FABRICATION AND HIGH HEAT FLUX TEST OF DIVERTOR COOLING ELEMENTS

June 1995

Satoshi SUZUKI, Masanori ARAKI, Kazuyuki NAKAMURA, Kazuyoshi SATOH
Kenji YOKOYAMA, Masayuki DAIRAKU and Masato AKIBA

日 本 原 子 力 研 究 所

Japan Atomic Energy Research Institute

Fabrication and High Heat Flux Test of Divertor Cooling Elements

Satoshi SUZUKI, Masanori ARAKI, Kazuyuki NAKAMURA, Kazuyoshi SATOH
Kenji YOKOYAMA, Masayuki DAIRAKU and Masato AKIBA

Department of Fusion Engineering Research
Naka Fusion Research Establishment
Japan Atomic Energy Research Institute
Naka-machi, Naka-gun, Ibaraki-ken

The plasma facing components in ITER are subjected to a high heat flux from fusion plasma. The heat flux is not only higher than that of existing tokamaks but also has a longer pulse duration (burn time). To minimize a peaking of the heat flux, the thermal deformation towards the plasma should be restrained. One-meter-long monoblock divertor modules with a sliding support structure were fabricated and tested at JAERI. Two kinds of support mechanisms were provided to minimize the thermal deformation of the modules in the upward and downward directions ; one is a pin type sliding structure and the other is a rail type support structure. Both modules were tested on the electron beam HHF test facility, JEBIS (JAERI Electron Beam Irradiation System), in JAERI. The steady-state heat flux of 15 MW/m^2 was applied to the surface of the modules to simulate the design condition of ITER CDA. As a result of the HHF test, the peformance of the sliding support structures was successfully demonstrated.

Three dimensional elastic stress analyses were conducted using a finite element method. The result shows that the relatively high thermal stress is observed at the cooling tube ; and that the maximum thermal stress at the cooling tube exceeds its yield strength. It is necessary to perform the lifetime evaluation of the copper cooling tube against cyclic thermal stresses.

i

ダイバータ冷却構造体の製作及び高熱負荷実験

日本原子力研究所那珂研究所核融合工学部

鈴木　　哲・荒木　政則・中村　和幸・佐藤　和義

横山　堅二・大楽　正幸・秋場　真人

　ITERのプラズマ対向機器は，現有のトカマク型核融合実験装置と比べ，より高い熱負荷に，より長時間にわたってさらされる。また，プラズマ対向機器に対する局所的な熱負荷のピーキングを避けるために，構造体のメインプラズマ側への熱変形は可能な限り抑制する必要がある。そこで熱変形を抑制するための摺動支持機構を有するモノブロック型ダイバータ冷却構造模擬試験体を製作し，原研の高熱負荷試験装置JEBISにおいて高熱負荷実験を実施した。今回製作した2体の試験体はそれぞれピン型及びレール型の摺動支持機構を有しており，試験体の上下方向への熱変形を抑制する。実験では，ITER概念設計段階における設計熱負荷条件を模擬して，定常熱流束15MW／㎡において繰り返し加熱を実施した。その結果，試験体の上下方向の熱変形量は0.5mm以内に抑制されることを確認し，摺動支持機構の有効性を実証した。

　また，本実験を模擬した3次元弾性応力解析を有限要素コードを用いて実施した結果，試験体のアーマタイル間の冷却管部に高い熱応力が発生することがわかり，無酸素銅製の冷却管の繰り返し熱応力に対する損傷評価が必要なことが明らかとなった。

那珂研究所：〒311-01　茨城県那珂郡那珂町向山801-1

Contents

目　　　　次

1. Introduction

Various types of divertor structures have been designed and presented in the ITER conceptual design activity(ITER-CDA). A water cooled divertor plate with CFC armors has been one of the most promising divertor structures. To reduce heavy particle contamination to a main plasma, materials with low atomic number are preferable as a plasma facing material of ITER. Therefore, use of carbon based materials such as CFC's for a divertor armor is one solution. JAERI has been developing divertor plate modules for the ITER divertor. We have successfully developed and tested 1m long divertor modules with a sliding support structure.

The ITER divertor plate is subjected to a high heat load and a high particle load from the main plasma. In the ITER-CDA, one of the critical issues for a divertor plate was how to reduce deformation of divertor plates toward the main plasma. The unevenness of the adjacent divertor plate will lead to severe erosion of the armor tiles by the peaked heat flux. Therefore, to avoid such unevenness, the deformation of the divertor plates towards the main plasma should be restrained as low as possible. A sliding support concept was presented to solve this problem. The deformation of the divertor plate towards the main plasma can be restrained by a rigid structure with the sliding support. Two types of the sliding support structure, a pin type structure and a rail type structure, were tested to demonstrate their validity for the ITER divertor plate.

2. Designs of sliding support structures

Pin type support structure

Figure 1 shows a schematic of the pin type support structure. It uses cylindrical pins to fix the divertor plate. Therefore, the divertor plate is always supported by the contact line between the fixing pin and an upper/lower structure even if the thermal deformation occurs in the divertor plate. The advantage and disadvantage of this structure are as follows;

- It has high reliability because it is hard to stick between the fixing pin and the upper/lower structure.

1. Introduction

Various types of divertor structures have been designed and presented in the ITER conceptual design activity(ITER-CDA). A water cooled divertor plate with CFC armors has been one of the most promising divertor structures. To reduce heavy particle contamination to a main plasma, materials with low atomic number are preferable as a plasma facing material of ITER. Therefore, use of carbon based materials such as CFC's for a divertor armor is one solution. JAERI has been developing divertor plate modules for the ITER divertor. We have successfully developed and tested 1m long divertor modules with a sliding support structure.

The ITER divertor plate is subjected to a high heat load and a high particle load from the main plasma. In the ITER-CDA, one of the critical issues for a divertor plate was how to reduce deformation of divertor plates toward the main plasma. The unevenness of the adjacent divertor plate will lead to severe erosion of the armor tiles by the peaked heat flux. Therefore, to avoid such unevenness, the deformation of the divertor plates towards the main plasma should be restrained as low as possible. A sliding support concept was presented to solve this problem. The deformation of the divertor plate towards the main plasma can be restrained by a rigid structure with the sliding support. Two types of the sliding support structure, a pin type structure and a rail type structure, were tested to demonstrate their validity for the ITER divertor plate.

2. Designs of sliding support structures

Pin type support structure

Figure 1 shows a schematic of the pin type support structure. It uses cylindrical pins to fix the divertor plate. Therefore, the divertor plate is always supported by the contact line between the fixing pin and an upper/lower structure even if the thermal deformation occurs in the divertor plate. The advantage and disadvantage of this structure are as follows;

- It has high reliability because it is hard to stick between the fixing pin and the upper/lower structure.

- The fixing pin gets high temperature due to nuclear heating because the thermal contact between the fixing pin and the support structure is poor. Therefore the pin material should be made of refractory metals or ceramics. (In this study, the pin was made of a stainless steel because the experiment did not simulate a volumetric nuclear heating.).

Rail type support structure

Figure 2 shows a schematic of the rail type support structure. It consists of the rail and the saddle shaped guide. Comparing to the pin type support structure, the bending deformation of the rail type structure is much less than that of the pin type structure. Because the divertor plate with the rail type structure is supported by the contact surface between the rail and the guide. The advantage and disadvantage of this structure are as follows;

- It has a very simple structure and it is easy to assemble.

- It has lower reliability because the rail and the guide are easy to stick each other comparing to the pin type support structure.

3. Divertor modules tested

Divertor module with a pin type support structure

Figure 3 shows a photo of the divertor module with a pin type support structure. Monoblock type structure was selected. The width, height and the length of the armor tiles are 25 mm, 30 mm and 25 mm, respectively. A felt type CFC material, CX-2002U (TOYO TANSO Co., LTD) is used as an armor material, which has high thermal conductivity in the felt plane. The total length of the module is about 1 m. The outer diameter of the cooling tube is 18 mm; the inner diameter is 15 mm. The cooling tube has a twisted tape insert to enhance its heat removal capability; its tape twist ratio is 3. It is known as 'swirl tube'. Based on Gambill's results[1], the heat transfer coefficient of this cooling tube is expected to be about twice as much as that of a normal straight tube under non-boiling condition. The cooling tube is made of OF-Cu. The armor tiles were brazed on the cooling tube with Ti-Cu-Ag braze material. There are four discrete support sections. The distance between each support sections is 30 cm. The support guides, the support arms and the fixing pins are made of austenitic stainless steel (SS304). The stainless steel box is mechanically attached to the back plate to improve its bending stiffness against thermal deformation.

Divertor module with a rail type support structure

Figure 4 shows a photo of the divertor module with a rail type support structure. A cross section of the module is also monoblock type structure. The dimensions of the armor tiles and the cooling tube are same as those of the pin type model. This module has also four support sections. The slide mechanism between the rail and the guide absorbs the thermal deformation of the divertor module. The slide resistance of the rail type support structure is believed to be greater than that of the pin type because of larger contact area at the support section. Therefore, a molybdenum-based solid lubricant was coated on the contact area to keep its slidability stable; the curvature of the inner surface of the guide also keeps its performance stable.

4. High heat flux test facility
- JEBIS (JAERI Electron Beam Irradiation System) -

High heat flux tests of the divertor modules were carried out on JEBIS in JAERI. JEBIS is the most sophisticated e-beam facility in the world for high heat flux testing. It has two plasma electron guns; they were originally developed for NBI (Neutral Beam Injector) for JT-60. They can deliver a high current e-beam up to 4 A with a maximum acceleration voltage of 100 kV. It can also irradiate a large area of around 1800 cm^2 using a multi-aperture grid and sweeping coils. Major performance and the schematic of JEBIS are summarized in Table 1 and Fig. 5, respectively. [2] [3]

Table 1 Major performance of JEBIS

Accel. voltage	20 - 100 kV
Accel. current	up to 4 A
Pulse duration	0.1 ms - CW
Working gas	Hydrogen
Sweeping freq.	0.01 - 1 kHz (unidirectional)
Max. heat flux	over 2 GW/m^2 at a heated area of 0.8 cm^2
Heated area	around 1800 cm^2 at a heat flux of 0.2 MW/m^2
Coolant	water at room temp.
Coolant flow rate	40 m^3/h
Inlet coolant pressure	up to 4 MPa

At present, JEBIS has two kinds of electron guns. One is used for plasma disruption simulation testing and the other is used for steady-state high heat flux testing. The former has an single-aperture grid to get a single focused electron beam; while the latter has multi-aperture grids to get a sheet-like electron beam. The data acquisition system of JEBIS is as follows;

- Infrared camera system (AGEMA 900)
- ITV camera system
- High speed video system (Kodak SP-2000)
- CAMAC system (diff. 32 ch available; on HP-9000)
- PC data sampling system (diff. 8 ch available; LabVIEW3 on Macintosh)

5. Experiment

Electron beam irradiation experiments were performed at JEBIS. The objectives of the experiments are as follows;

- To validate the slidability of both support structures.
- To investigate the soundness of the brazed parts.

Test conditions

Test conditions are summarized in Table 2.

Table 2 Test conditions and ITER CDA design values for divertor plates

	Experiment	ITER CDA design
Heat flux	15 MW/m^2	15 - 30 MW/m^2
Pulse duration	30 s	- 1000 s
Coolant pressure	4 MPa(Inlet)	3.5 MPa
Coolant temp.	25 °C	60 °C
Flow velocity	10 m/s	10 m/s

To obtain the temperature histories of the divertor module, type-K thermocouples were brazed on the top of the cooling tube; a needle and a ruler were attached at the end of the support section to observe its displacement caused by the thermal deformation under thermal loads. (See Fig. 1.) Surface temperature change was monitored and recorded by the infrared camera system.

- Infrared camera system (AGEMA 900)
- ITV camera system
- High speed video system (Kodak SP-2000)
- CAMAC system (diff. 32 ch available; on HP-9000)
- PC data sampling system (diff. 8 ch available; LabVIEW3 on Macintosh)

5. Experiment

Electron beam irradiation experiments were performed at JEBIS. The objectives of the experiments are as follows;

- To validate the slidability of both support structures.
- To investigate the soundness of the brazed parts.

Test conditions

Test conditions are summarized in Table 2.

Table 2 Test conditions and ITER CDA design values for divertor plates

	Experiment	ITER CDA design
Heat flux	15 MW/m^2	15 - 30 MW/m^2
Pulse duration	30 s	- 1000 s
Coolant pressure	4 MPa(Inlet)	3.5 MPa
Coolant temp.	25 °C	60 °C
Flow velocity	10 m/s	10 m/s

To obtain the temperature histories of the divertor module, type-K thermocouples were brazed on the top of the cooling tube; a needle and a ruler were attached at the end of the support section to observe its displacement caused by the thermal deformation under thermal loads. (See Fig. 1.) Surface temperature change was monitored and recorded by the infrared camera system.

The schematic of the experiment is shown in Fig. 6. In the experiments, two heated areas were selected to monitor its deformation modes. One is just on the surface where the support section was attached; the other was on the surface between the support sections.

Figure 7 shows the heat flux profile of the electron beam. Peak heat flux was over 15 MW/m^2. It simulated the ITER CDA design value. However, this profile of the beam did not simulate the heat flux distribution of ITER. The FWHM of the beam was about 150 mm. Pulse duration was 30s and the dwell duration was 30 s. This thermal cycle was selected so that the divertor module could sufficiently reach their thermal steady-state.

Coolant flow velocity and the coolant inlet pressure simulated ITER CDA design.

Results of the experiments

Temperature changes at the top of the cooling tube is shown in Fig. 8. The divertor module with a pin type support structure reached its thermal steady-state at around 8 - 10 s after the beam on. In this case, the unstable temperature change caused by the coolant boiling did not appear through the experiments. As a result of the experiments, both types of the divertor module could keep their thermal performance.

Figure 9 shows photos of the divertor module with a rail type support structure at the heating phase and the cooling phase. The divertor module was heated just on the surface where the support section was attached. The thermal expansion along the coolant flow direction of the module was monitored by the ITV camera system. In both types of the modules, the elongation was less than 0.5 mm; the upward deformation of the module could successfully be restrained to within 0.5 mm. However, the large bending deformation was observed in the divertor module with the rail type support structure in such a case that the armor blocks between the support structure was heated. Because the rail type support structure has curved surface in its guides; it is relatively easy to rotate against the bending deformation. The shape of the guides must be modified.

6. Numerical analyses

To predict the thermal deformation of the divertor modules, finite element analyses were performed. Three dimensional half models were selected to precisely investigate the thermal deformation of the modules. In the analyses, steady-state thermal analyses were carried out to obtain temperature distributions of the divertor module. Based on the temperature distribution obtained, elastic thermal stress analyses were performed. To simplify the stress-strain behavior of the divertor module, the clearance of the adjacent armor tile was ignored. To consider the effect of the element size, the elastic stress analyses were performed with three different mesh distributions. Nine integration points element and 4 integration points element (reduced integration points element) were used in the stress analyses.

FE code : ABAQUS ver 4-9-1 (FACOM VP version)

6.1 Thermal analyses

Analytical model

Cross sectional view of the FE model along the coolant flow direction is shown in Fig. 10; cross sectional view perpendicular to the coolant flow direction is also shown in Fig. 11. The model contains 40 armor blocks totally.

There are three kinds of FE meshes used in the analyses from the view point of the number of partitions within an armor tile where the heat flux was applied.

Figure 12 shows the FE mesh except for the armor tile where the heat flux was applied. This part of the mesh is common for all the following analyses. On the other hand, the mesh of the heated area varies three types, CASE 1, CASE 2 and CASE 3.

Figure 13 shows "Coarse mesh".   (CASE 1)
Figure 14 shows "Medium mesh". (CASE 2)
Figure 15 shows "Fine mesh".   (CASE 3)

The number of nodes and elements are summarized in Table 3.

Table 3 The number of nodes and elements of FE meshes

	Nodes	Elements	Elm. type
CASE 1	13023	1680	DC3D20
CASE 2	13471	1764	DC3D20
CASE 3	18341	2712	DC3D20

Initial conditions and boundary conditions

In the thermal analyses, the initial temperature of the whole model was assumed to be 40 °C. And the coolant bulk temperature (sink temperature) was also assumed to be 40 °C. Uniform heat flux distribution was assumed.

Boundary conditions for the analyses are shown in Fig. 16-(A), (B) and (C). The heat transfer coefficient of the cooling tube was assumed to be a function of the wall temperature. It is based on the Dittus-Boelter's correlation for a non-boiling phase and it is based on shah's correlation under a boiling phase. Considering the swirl flow effect, Gambill's enhancement factor was used for the calculation. Figure 17 shows the heat transfer coefficient of the cooling tube as a function of the wall temperature.

Material properties

Tables 4 and 5 summarize material properties used in the analyses.

Table 4 Thermal conductivity of OF-Cu

Temp. (°C)	λ (W/m/K)
0.0	399.4
27.0	398.0
327.0	383.0
527.0	371.0
727.0	357.0
927.0	342.0

Table 5 Thermal conductivity of CX-2002U

Temp. (°C)	λx (W/m/K)	λy (W/m/K)	λz (W/m/K)
0.0	338.7	403.1	224.5
27.0	320.1	381.0	215.0
127.0	251.3	299.0	180.0
227.0	213.5	254.0	150.0
427.0	161.7	193.0	116.6
627.0	127.1	153.0	84.5
1000.0	100.0	120.0	74.0
1500.0	85.0	104.0	65.0

Results of the thermal analyses

Figure 18 shows the node sets where nodal temperatures to be output.

Figures 19-(A), (B), (C) and (D) show the temperature distribution obtained in CASE 1. Also, Figures 20-(A), (B), (C), (D), 21-(A), (B), (C) and (D) show the results of the CASE 2 and CASE 3, respectively. Maximum steady-state temperatures appeared at the top of the cooling tube are summarized in Table 6.

Table 6 Maximum steady-state temperature in each analyses

	at the cooling tube (upper) (°C)	at the cooling tube (lower) (°C)
CASE 1	315	52.8
CASE 2	308	53.1
CASE 3	309	53.1

As shown in Table 6, all the results are in good agreement with each other. Mesh size dependency did not appear in these thermal analyses.

6.2 Elastic thermal stress analyses

Analytical model

There are five FE models totally in the stress analyses. CASE 1, CASE 3 and CASE 5 used the same FE mesh used in the thermal analyses. On the other hand, CASE 2 and CASE 4 used reduced integration point elements. (See Table 7)

Table 7 The number of nodes and elements of FE meshes

	Nodes	Elements	Elm. type
CASE 1	13023	1680	C3D20
CASE 2	13023	1680	C3D20R (reduced intg. pts.)
CASE 3	13471	1764	C3D20
CASE 4	13471	1764	C3D20R (reduced intg. pts.)
CASE 5	18341	2712	C3D20

Initial conditions and boundary conditions

The reference temperature for the stress analyses were assumed to be 40 °C. Mechanical boundary conditions are shown in Fig. 22-(A) and (B).

Material properties

The material properties used in the stress analyses are summarized in Table 8 and Table 9.

Table 8 Mechanical properties of OF-Cu

Temp. (°C)	Young's modulus (GPa)	Poisson's ratio	Therm. exp. coeff. (x 10^{-6}/K)
0.0	82.4	0.33	15.3
20.0	82.4	0.33	15.4
100.0	78.5	0.33	15.9
200.0	73.5	0.33	16.6
400.0	68.6	0.33	18.3
500.0	65.7	0.33	19.1
600.0	61.8	0.33	20.0
800.0	58.8	0.33	21.6

Table 9 Mechanical properties of CX-2002U

	X component	Y component	Z component
Young's modulus (GPa)	8.10	10.69	3.4
Poisson's ratio	0.19	0.19	0.19
Therm. exp. coeff. (x 10^{-6}/K)	1.70	1.50	5.80

Analyses cases

CASE 1   "Coarse mesh"
Integration points = 3 x 3 x 3
Temperature distribution from the CASE 1 (Thermal analysis) was referred.

CASE 2   "Coarse mesh"
            Integration points = 2 x 2 x 2 (reduced)
            Temperature distribution from the CASE 1 (Thermal
            analysis) was referred.

CASE 3   "Medium mesh"
            Integration points = 3 x 3 x 3
            Temperature distribution from the CASE 2 (Thermal
            analysis) was referred.

CASE 4   "Medium mesh"
            Integration points = 2 x 2 x 2 (reduced)
            Temperature distribution from the CASE 2 (Thermal
            analysis) was referred.

CASE 5   "Fine mesh"
            Integration points = 3 x 3 x 3
            Temperature distribution from the CASE 3 (Thermal
            analysis) was referred.

Results

   Figure 23 shows node sets where the nodal displacement to be output. Figure 24 also shows element sets where the stress components to be output.

   Figures 25 - 28, 29 - 32, 33 - 36, 37 - 40, and 41 - 44 show the deformations of CASE 1, CASE 2 CASE 3, CASE 4 and CASE 5 along X, Y and Z directions, respectively; Figures 45 - 64 also show the deformations around the selected points in each case. The deformations along Z direction which correspond to the elongation along the flow direction were about 0.6 - 0.8 mm in all cases. According to these results, the FE mesh size did not strongly affect the deformation of the model.

   On the other hand, stress distribution of the model varied in each case. Figures 65 - 84 show the von Mises and the Tresca equivalents stress distributions of CASE 1, CASE 2, CASE 3, CASE 4 and CASE 5. In general, if the reduced integration points elements are used, the stress distribution looks smooth. However, the stress distributions around the armor tile where the heat flux was applied were oscillated especially at

the tile edge in all cases. The maximum von Mises and Tresca equivalent stresses were around 100 MPa in all cases. These values exceed the yield strength of OF-Cu; the cooling tube will be in elastoplastic phase. The lifetime evaluation of the cooling tube against cyclic thermal stresses will be necessary under the consideration of the elastoplastic behavior of OF-Cu.

7. Conclusion

1. The performance of the pin type sliding support structure was validated under cyclic heat flux of over 15 MW/m^2. The displacement along the coolant flow direction was less than 0.5 mm; the upward deformation at the supported point was successfully restrained about 0.5 mm.

2. For the rail type support structure, relatively large bending deformation was found in the experiment. The shape of its guide and the rail should be modified.

3. As results of the FE analyses, the displacement along the coolant flow direction of the divertor modules, U_z, were predicted to be within 0.1 mm in each analytical case.

4. The thermal stress at the cooling tube between each armor tiles was predicted relatively high. The stress value at that point was found to exceed the yield strength of the OFHC copper. The lifetime evaluation of the cooling tube against the cyclic thermal stress should be done.

the tile edge in all cases. The maximum von Mises and Tresca equivalent stresses were around 100 MPa in all cases. These values exceed the yield strength of OF-Cu; the cooling tube will be in elastoplastic phase. The lifetime evaluation of the cooling tube against cyclic thermal stresses will be necessary under the consideration of the elastoplastic behavior of OF-Cu.

7. Conclusion

1. The performance of the pin type sliding support structure was validated under cyclic heat flux of over 15 MW/m^2. The displacement along the coolant flow direction was less than 0.5 mm; the upward deformation at the supported point was successfully restrained about 0.5 mm.

2. For the rail type support structure, relatively large bending deformation was found in the experiment. The shape of its guide and the rail should be modified.

3. As results of the FE analyses, the displacement along the coolant flow direction of the divertor modules, U_z, were predicted to be within 0.1 mm in each analytical case.

4. The thermal stress at the cooling tube between each armor tiles was predicted relatively high. The stress value at that point was found to exceed the yield strength of the OFHC copper. The lifetime evaluation of the cooling tube against the cyclic thermal stress should be done.

Acknowledgment

The present work has been completed through the discussions with other staffs in NBI Heating Laboratory, JAERI-Naka. The authors wish to express their special thanks to Mr. Hashimoto for his extensive efforts on numerical calculations. The authors would like to acknowledge S. Shimamoto, the Director of Department of Fusion Engineering Research at JAERI, S. Matsuda, Japanese Home Team Leader of ITER-EDA.

References

(1)   W. R. Gambill et al., ORNL-2911, Oak Ridge National Laboratory (1960).

(2)   S. Tanaka, et al., Rev. Sci. Instr. 62 (3) (1991).

(3)   M. Akiba, et al., Fusion Technology 21 (1992) 1835.

Acknowledgment

The present work has been completed through the discussions with other staffs in NBI Heating Laboratory, JAERI-Naka. The authors wish to express their special thanks to Mr. Hashimoto for his extensive efforts on numerical calculations. The authors would like to acknowledge S. Shimamoto, the Director of Department of Fusion Engineering Research at JAERI, S. Matsuda, Japanese Home Team Leader of ITER-EDA.

References

(1) W. R. Gambill et al., ORNL-2911, Oak Ridge National Laboratory (1960).
(2) S. Tanaka, et al., Rev. Sci. Instr. 62 (3) (1991).
(3) M. Akiba, et al., Fusion Technology 21 (1992) 1835.

900 mm

300 mm

Cooling tube
(O.D. 18 / I.D. 15)

Support guide

Fixing pin

Support arm

SS box

Armor tile

} Divertor plate (upper structure)

} Support structure (lower structure)
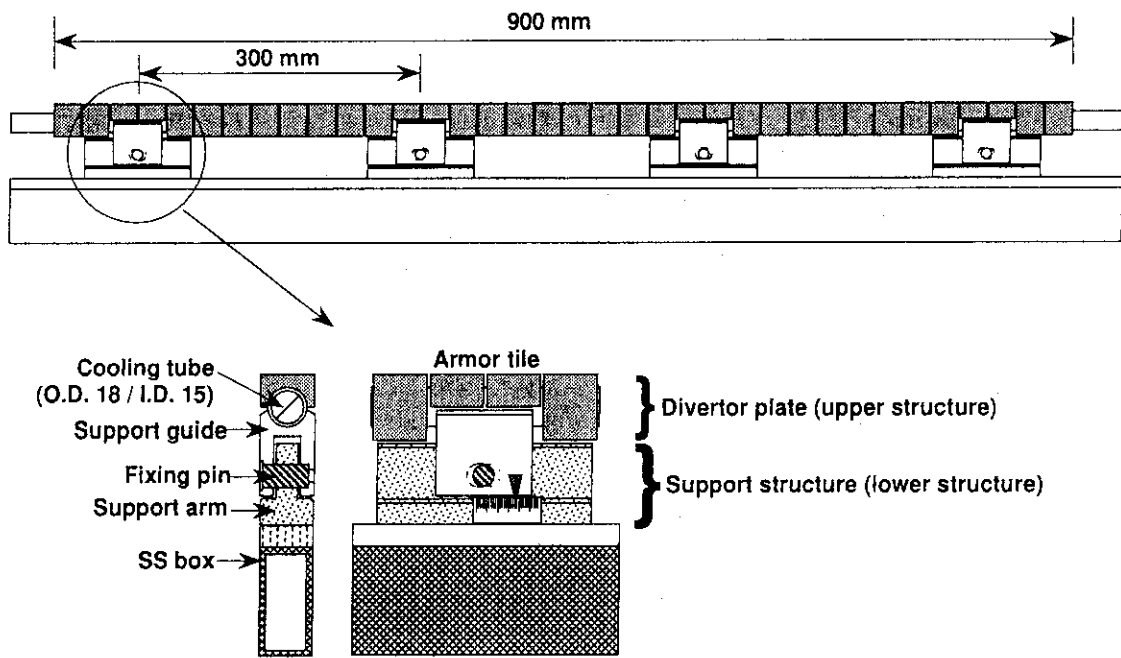
Fig. 1 Schematic view of a pin type support structure

900 mm

300 mm

Cooling tube
(O.D. 18 / I.D. 15)

Support guide

Rail

Armor tile

} Divertor plate (upper structure)

} Support structure (lower structure)
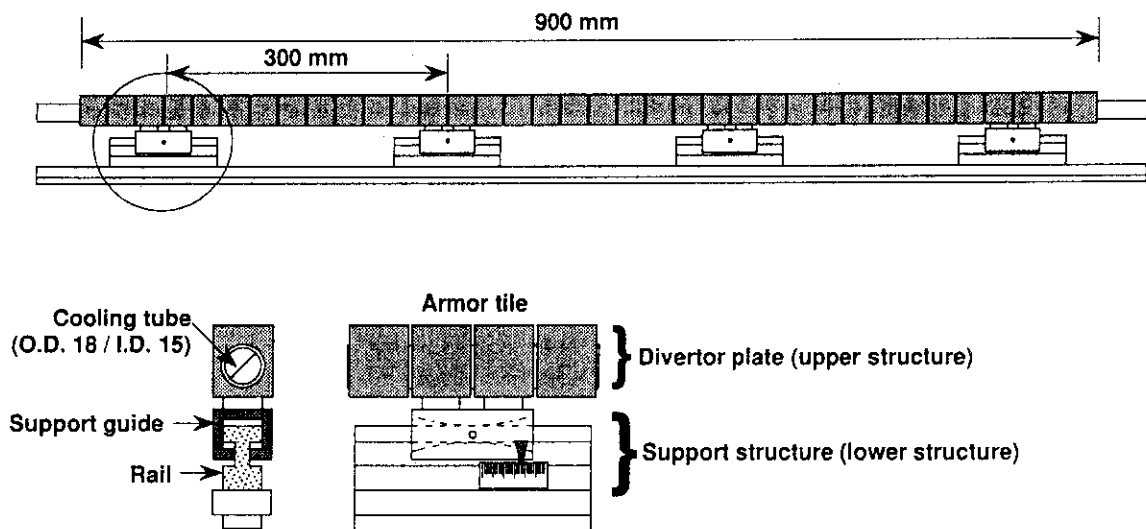
Fig. 2 Schematic view of a rail type support structure
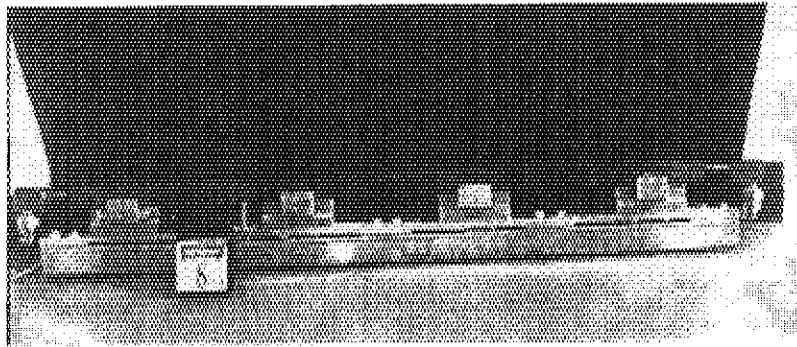
Fig. 3 Divertor module with a pin type support structure

Fig. 4 Divertor module with a rail type support structure

Plasma electron gun #1

Plasma electron gun #2

View port

Sweeping and deflection coil

Remotely handled sample holder

Electron beam

Beam limitter

Beam target

Divertor mock-up

Beam dump

JEBIS (JAERI Electron Beam Irradiation System)

1200 mm
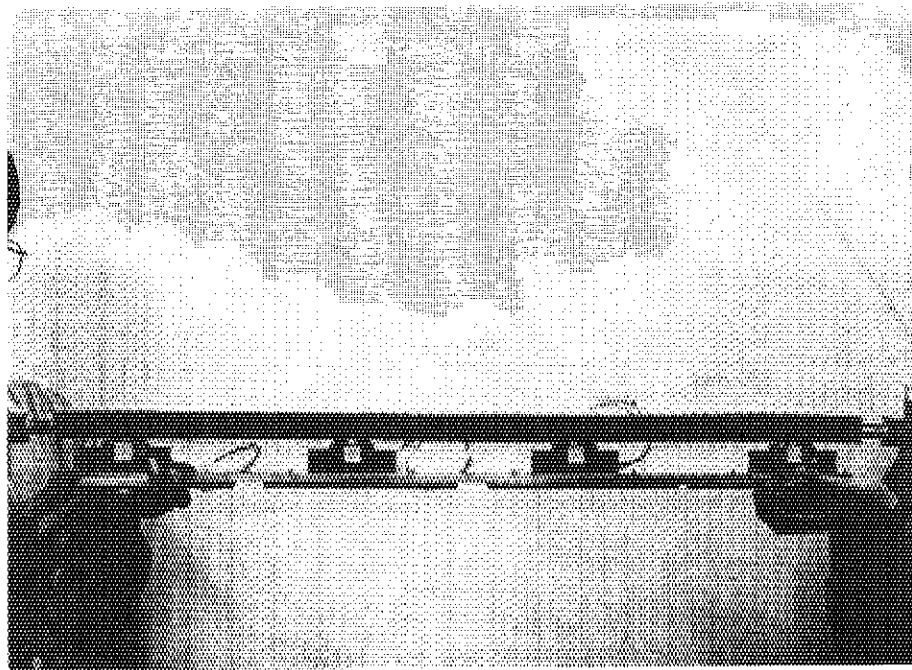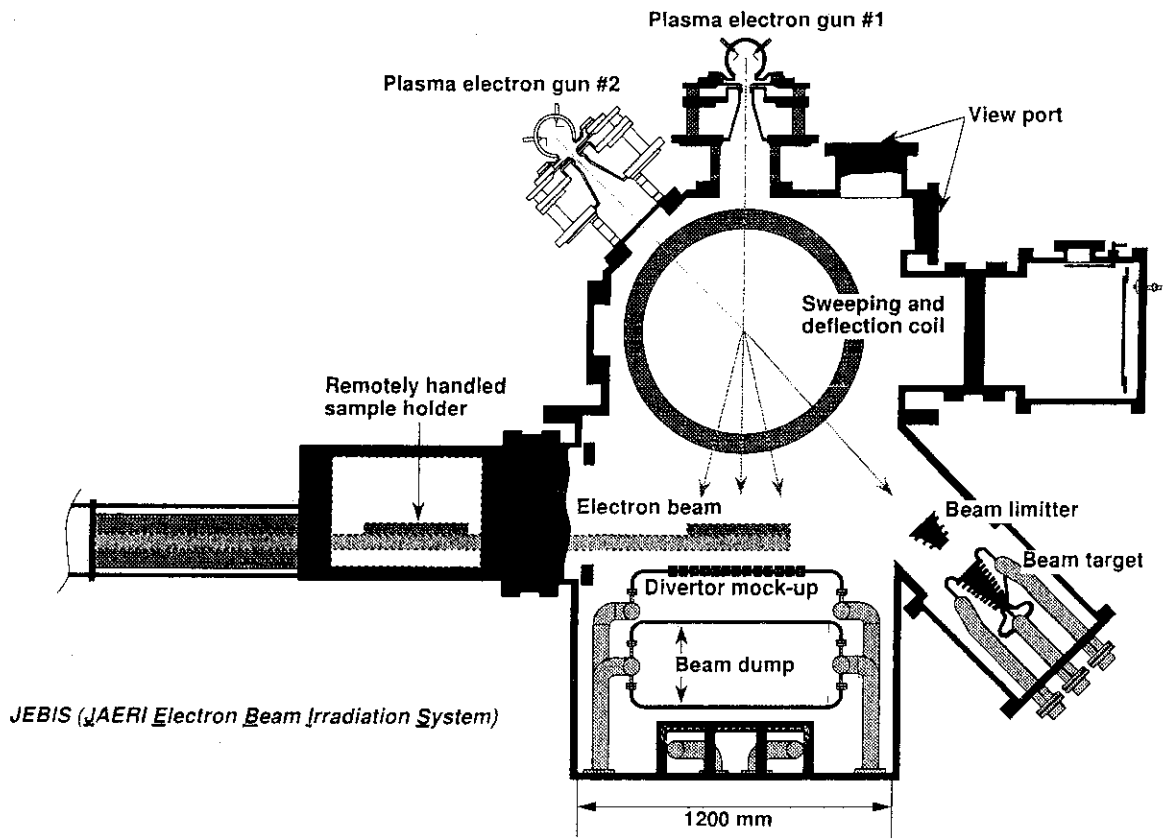
Fig. 5 Schematic view of JEBIS

Electron beam
(Swp freq. = 1kHz)
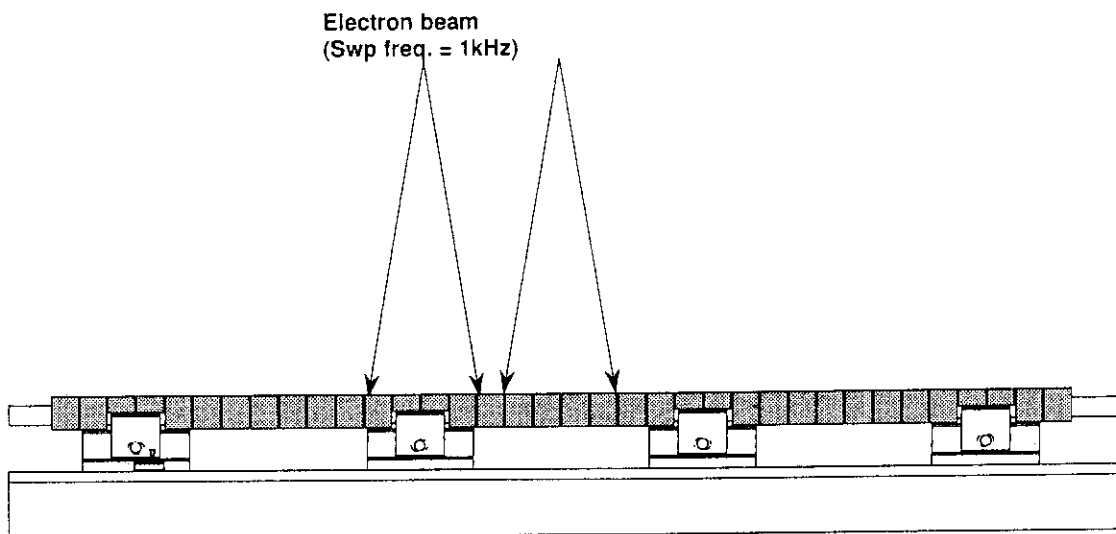
Fig. 6 Schematic view of electron beam irradiation tests
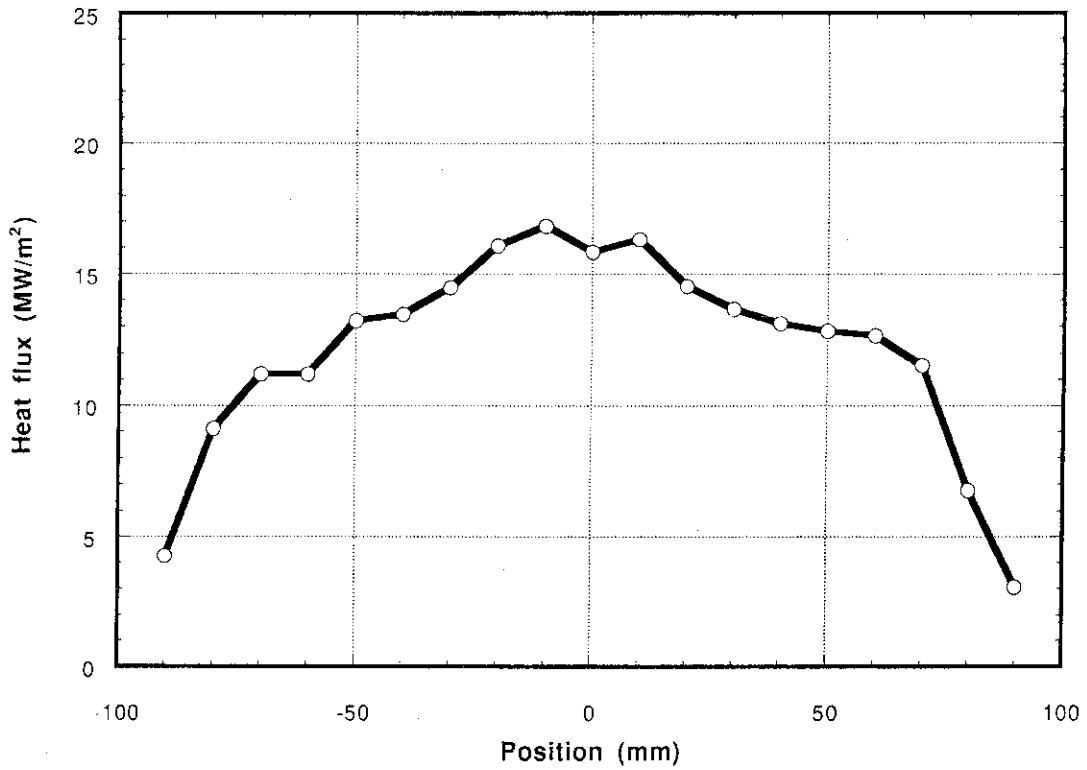
Fig. 7 Typical surface heat flux distribution at the divertor module
(along the coolant flow direction)
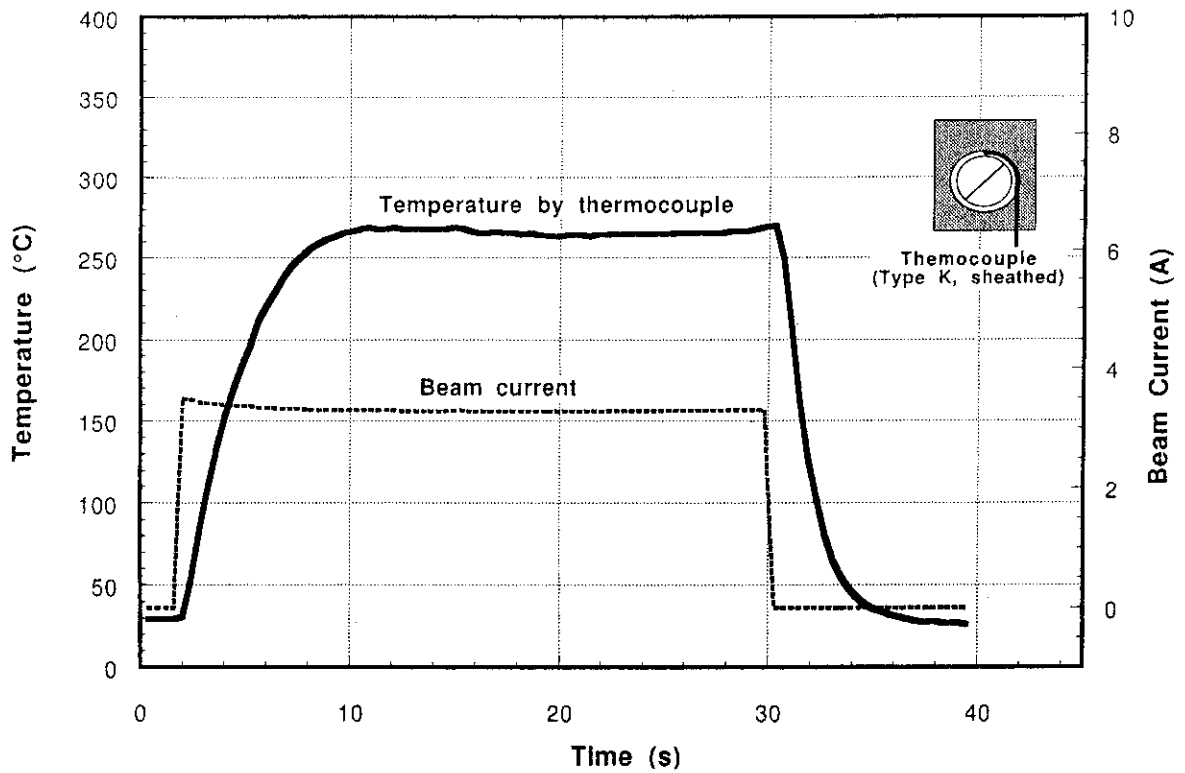
Fig. 8 Temperature change at the top of the cooling tude (Pin type model)
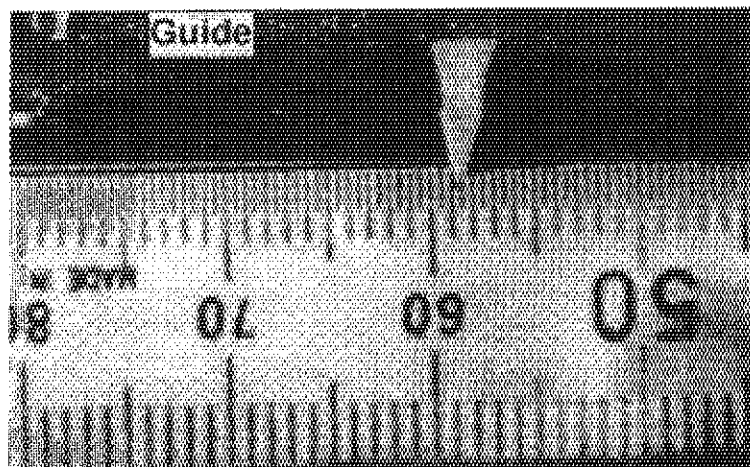
Before heating
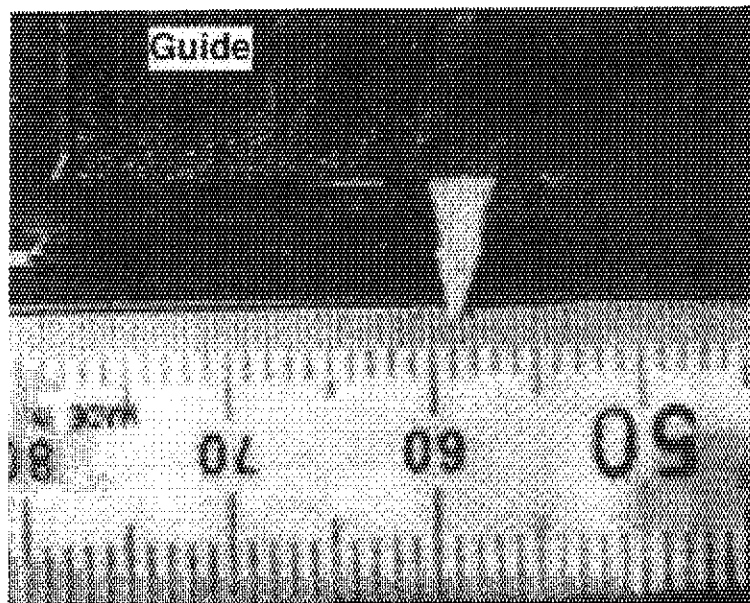
In the heating period

(scale : mm)

Fig. 9 Displacement of the rail type module
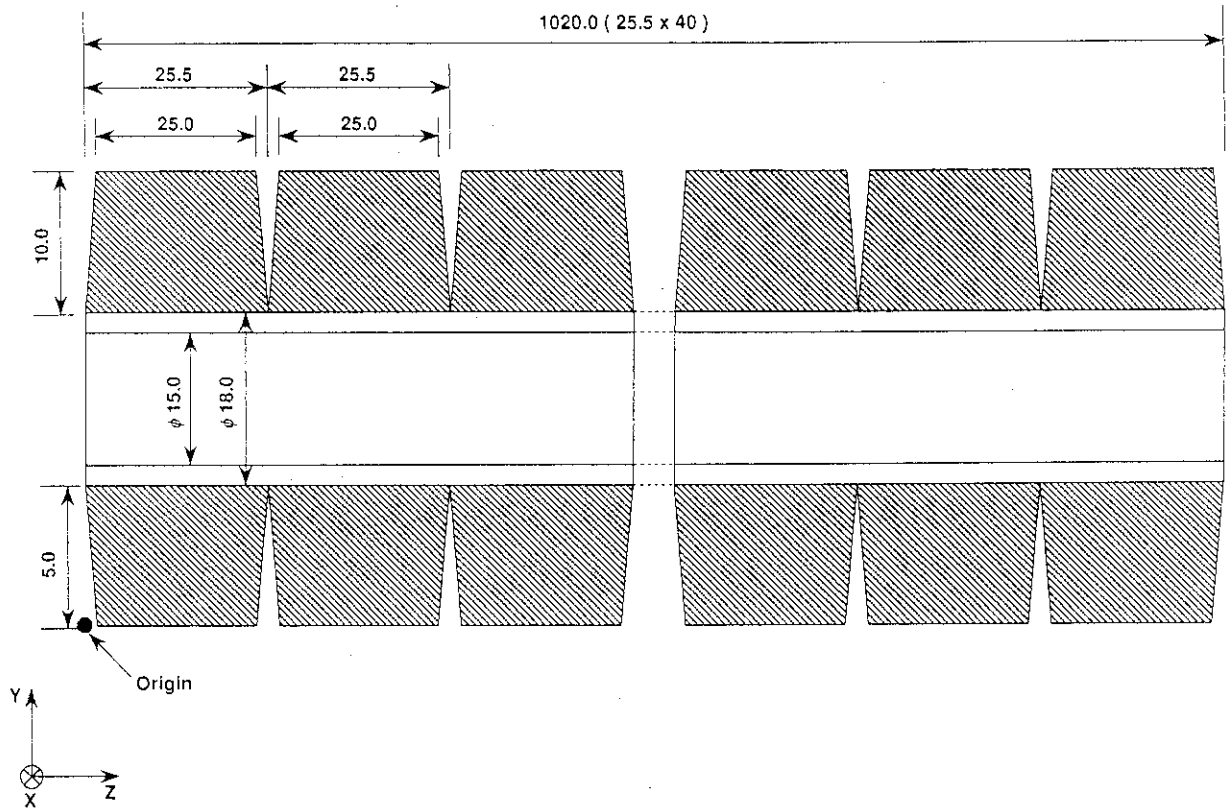
Fig. 10 FE model used (along coolant flow direction)
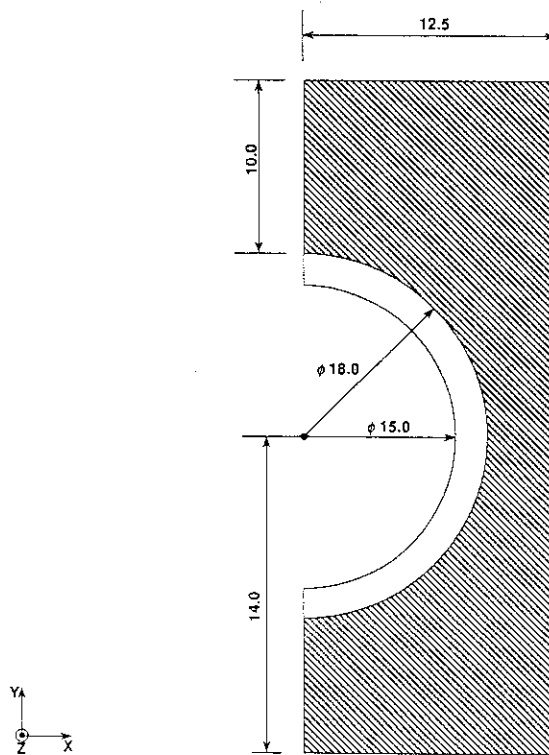
Fig. 11 FE model used (perpendicular to the coolant flow direction)
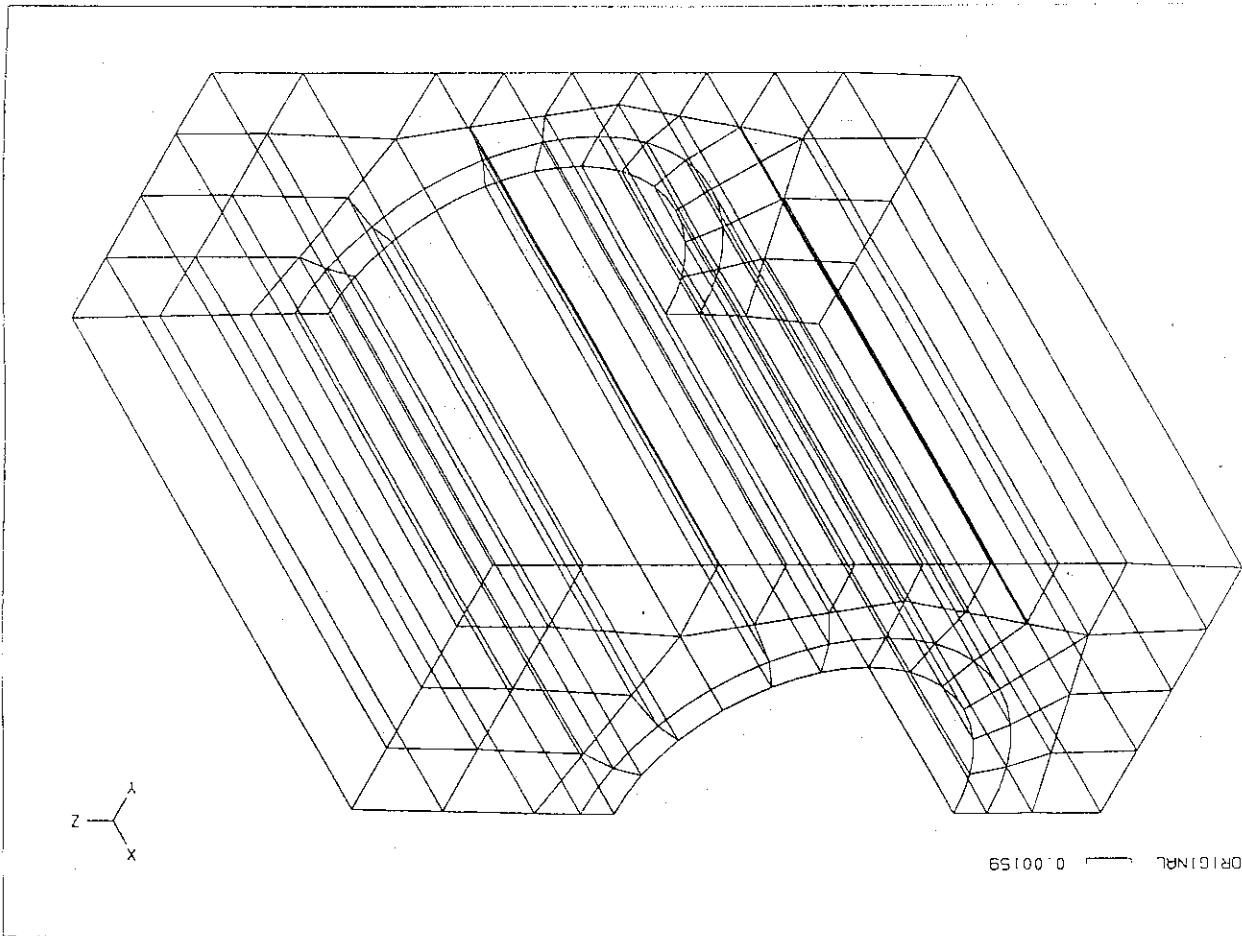
Fig. 13 FE mesh where the heat flux was applied (CASE 1)
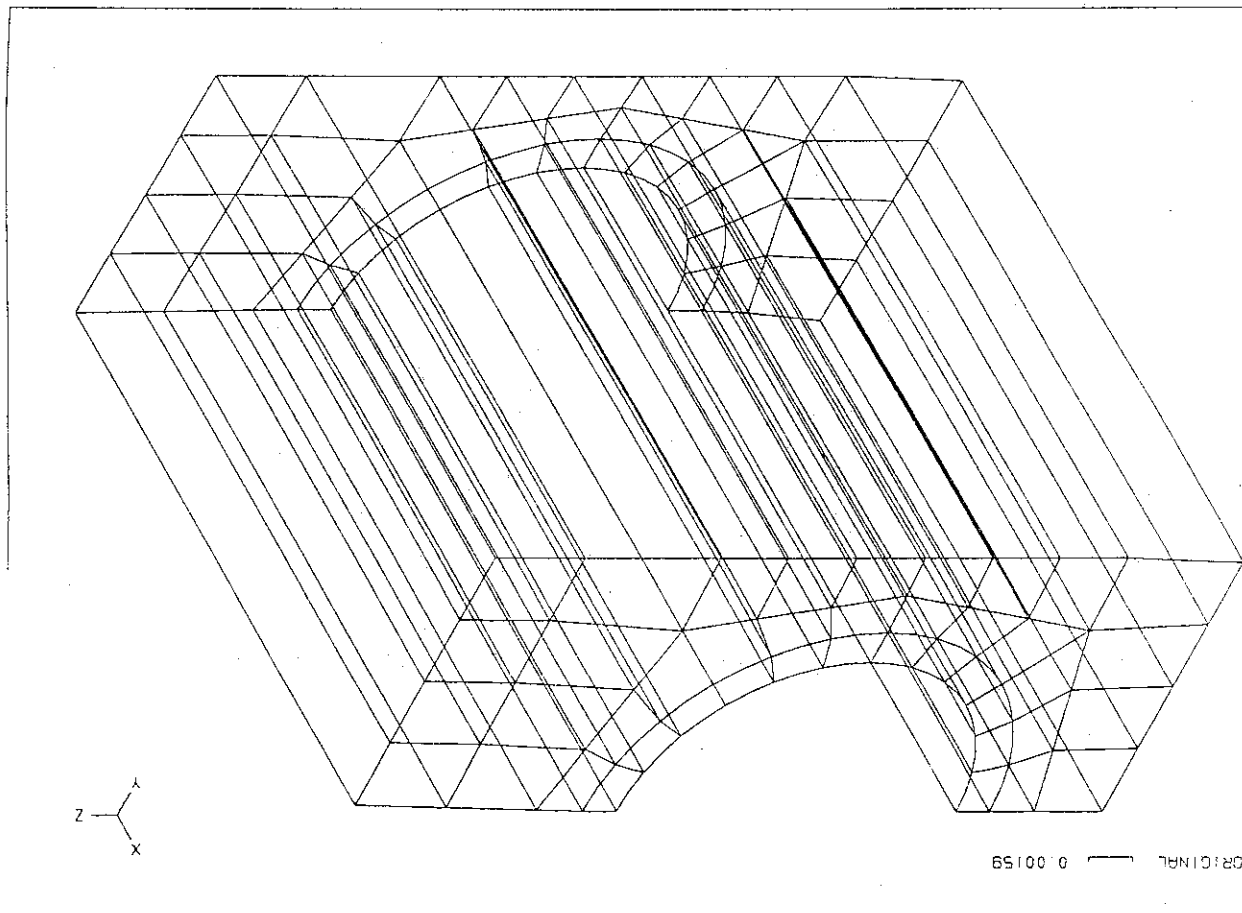
Fig. 12 FE mesh
(except for the armor tile where the heat flux was applied)
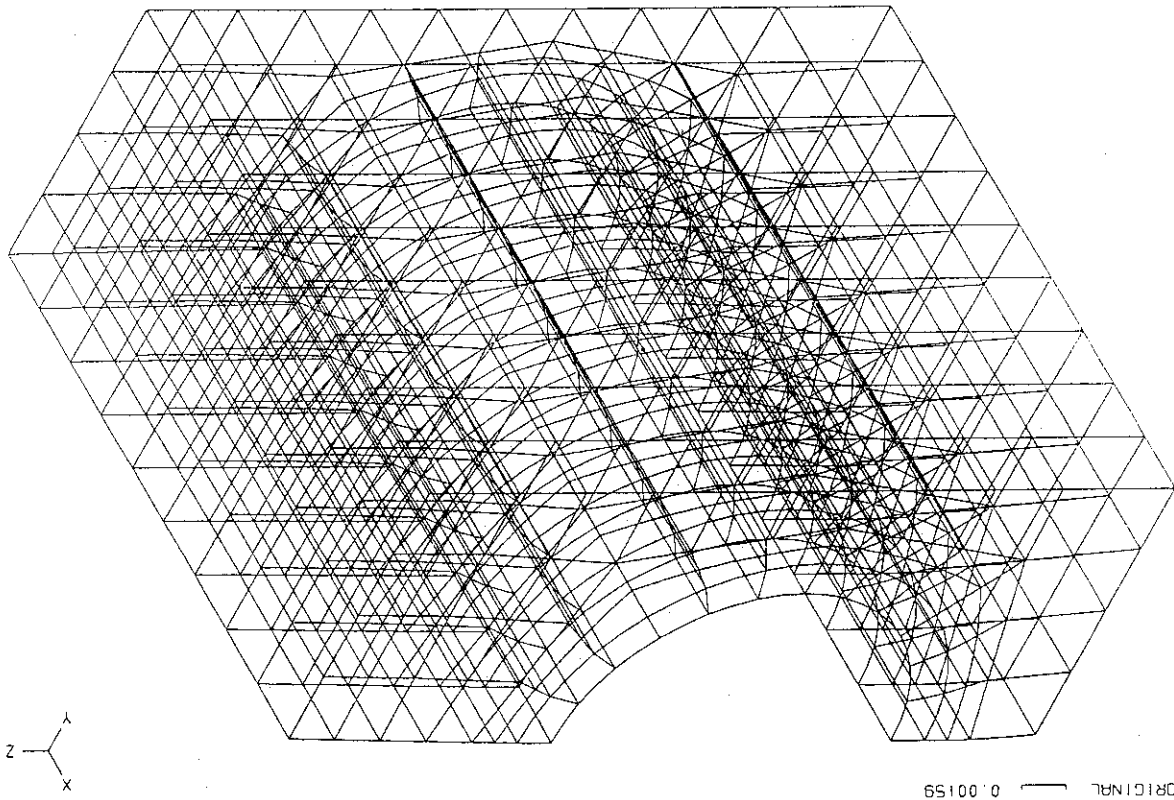
Fig.15 FE mesh where the heat flux was applied (CASE 3)
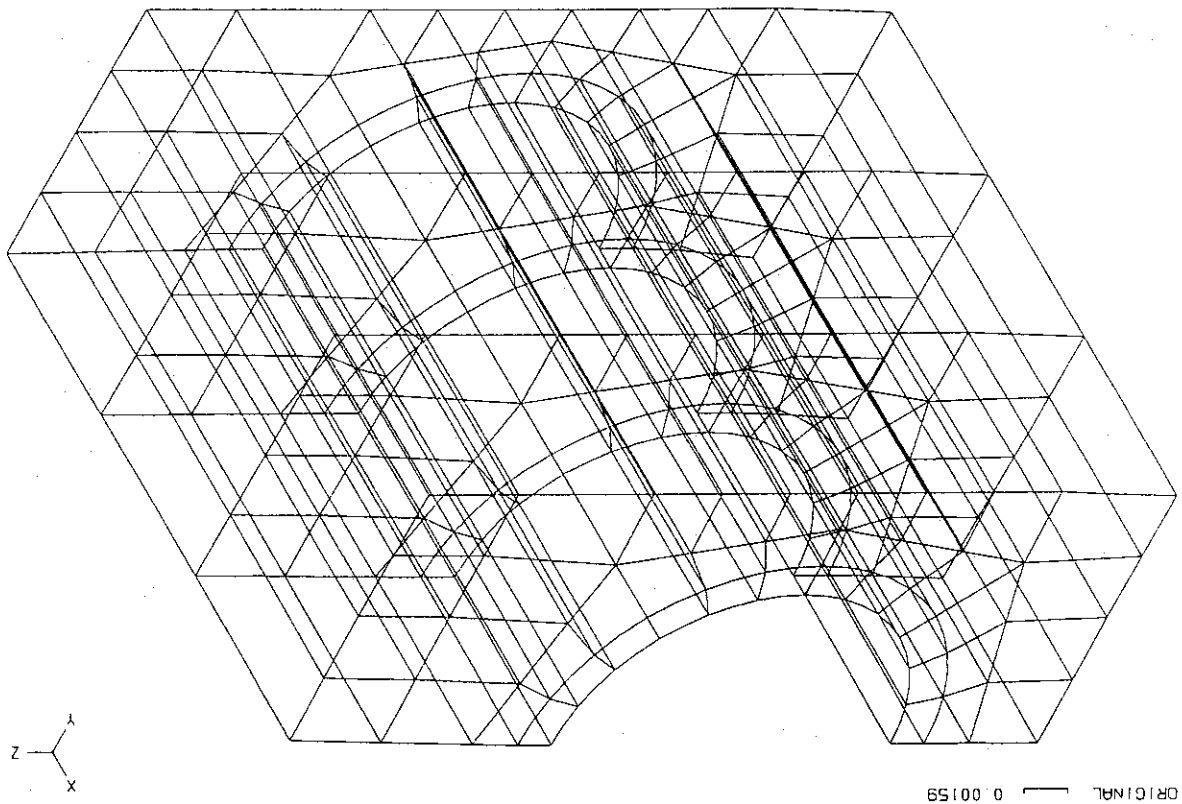
Fig.14 FE mesh where the heat flux was applied (CASE 2)
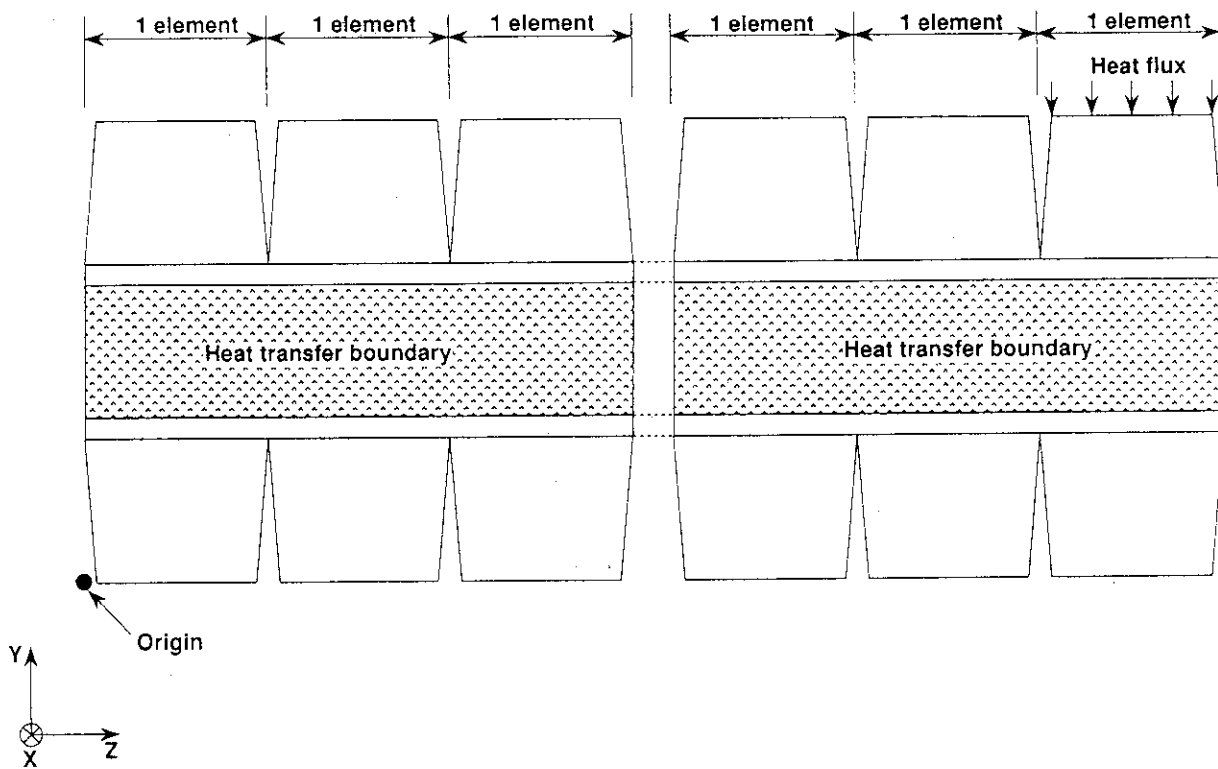
Fig. 16(A) Boundary conditions for thermal analyses (CASE 1)
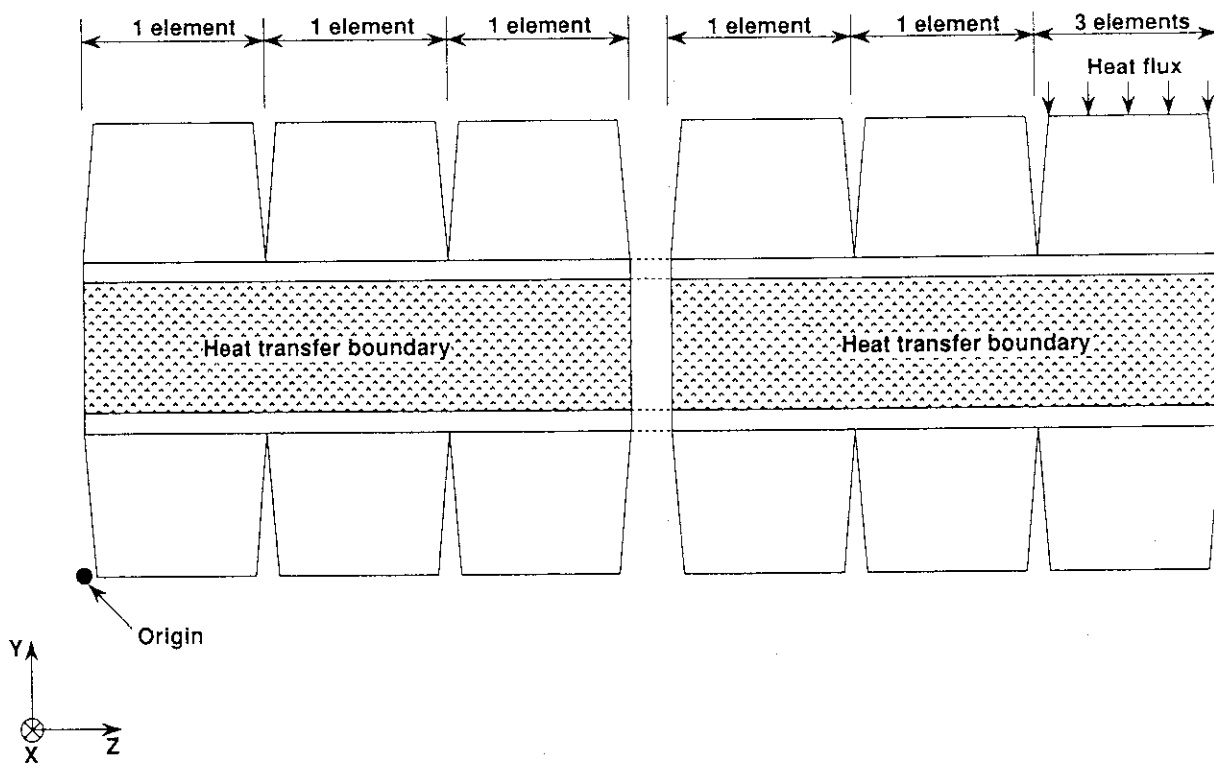
Fig. 16(B) Boundary conditions for thermal analyses (CASE 2)
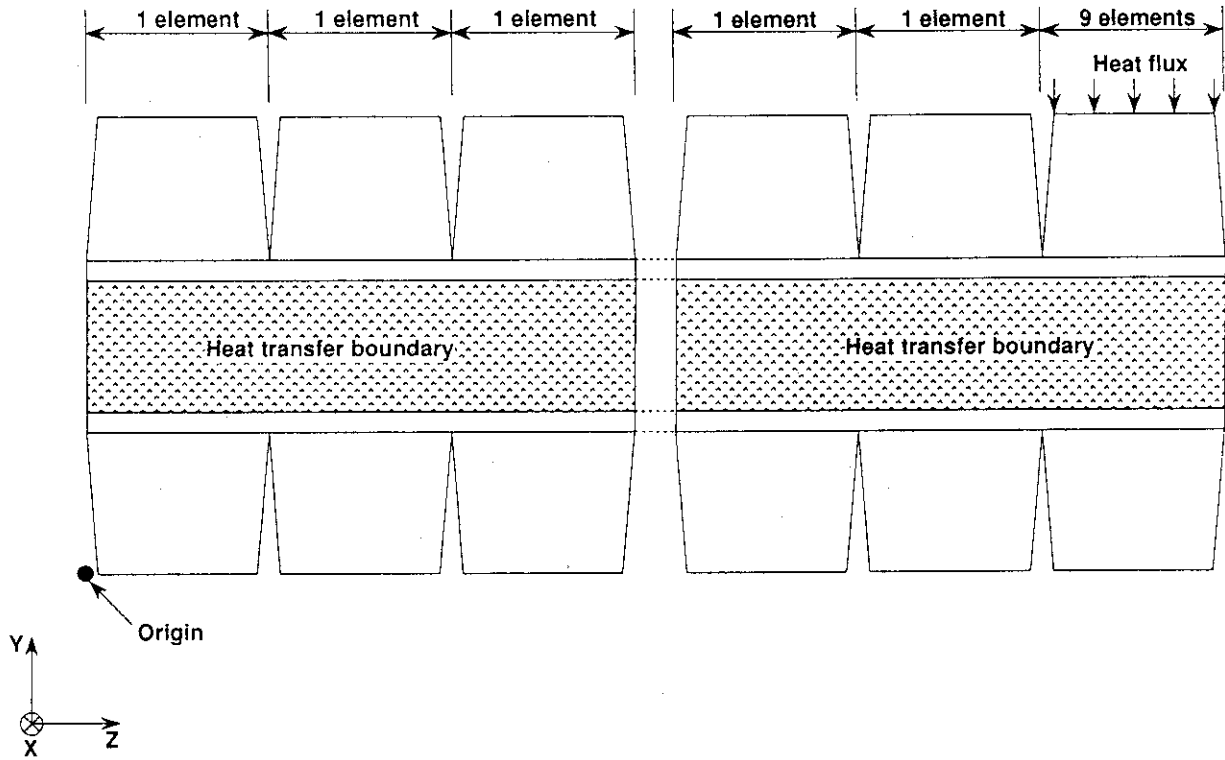
Fig. 16 (C) Boundary conditions for thermal analyses (CASE 3)
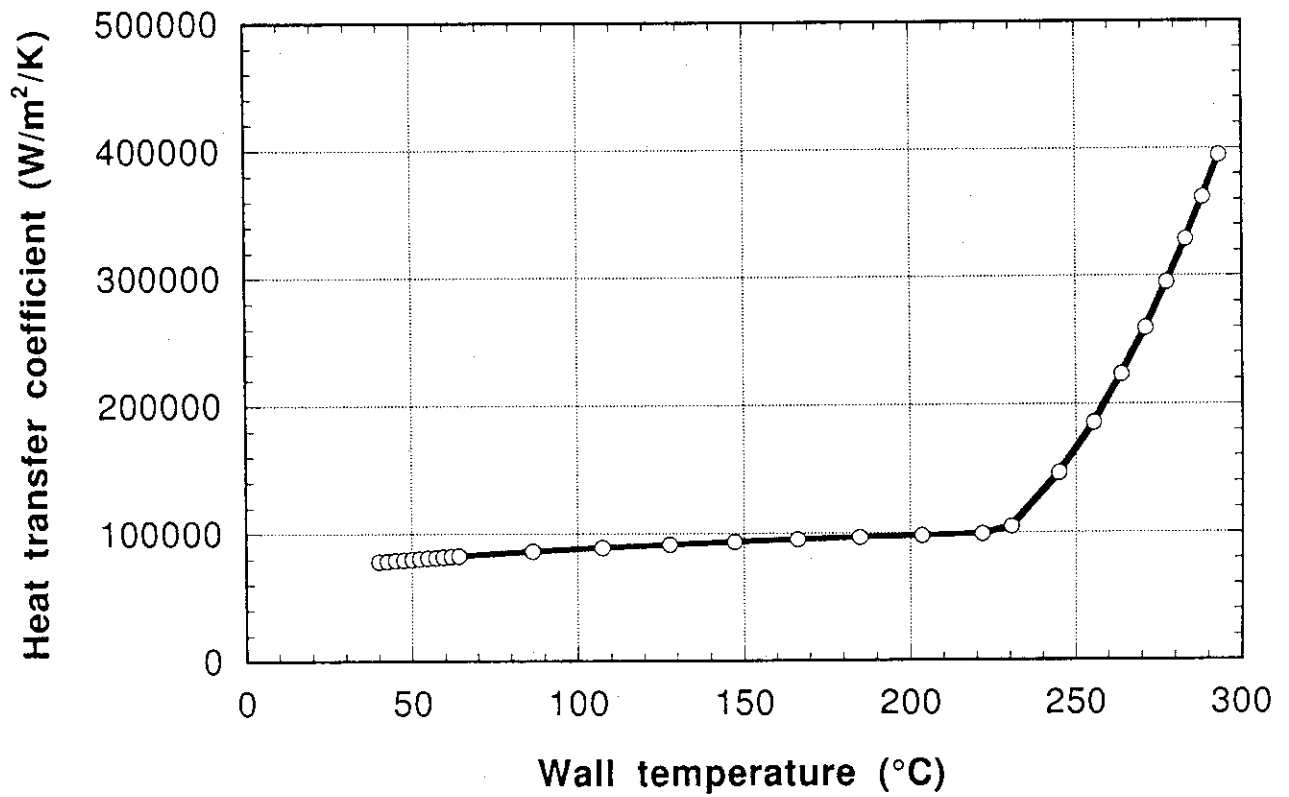
Fig. 17 Heat transfer coefficient of the cooling tube
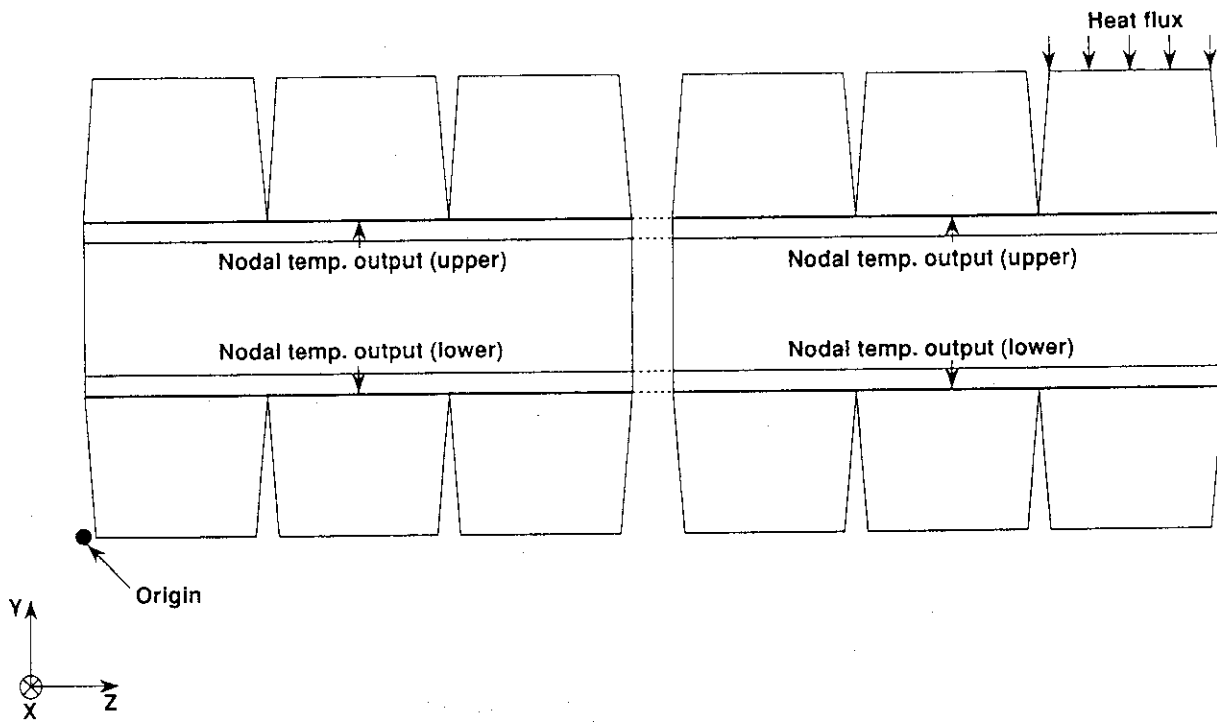
Fig. 18　Node sets to be output

1-21.data
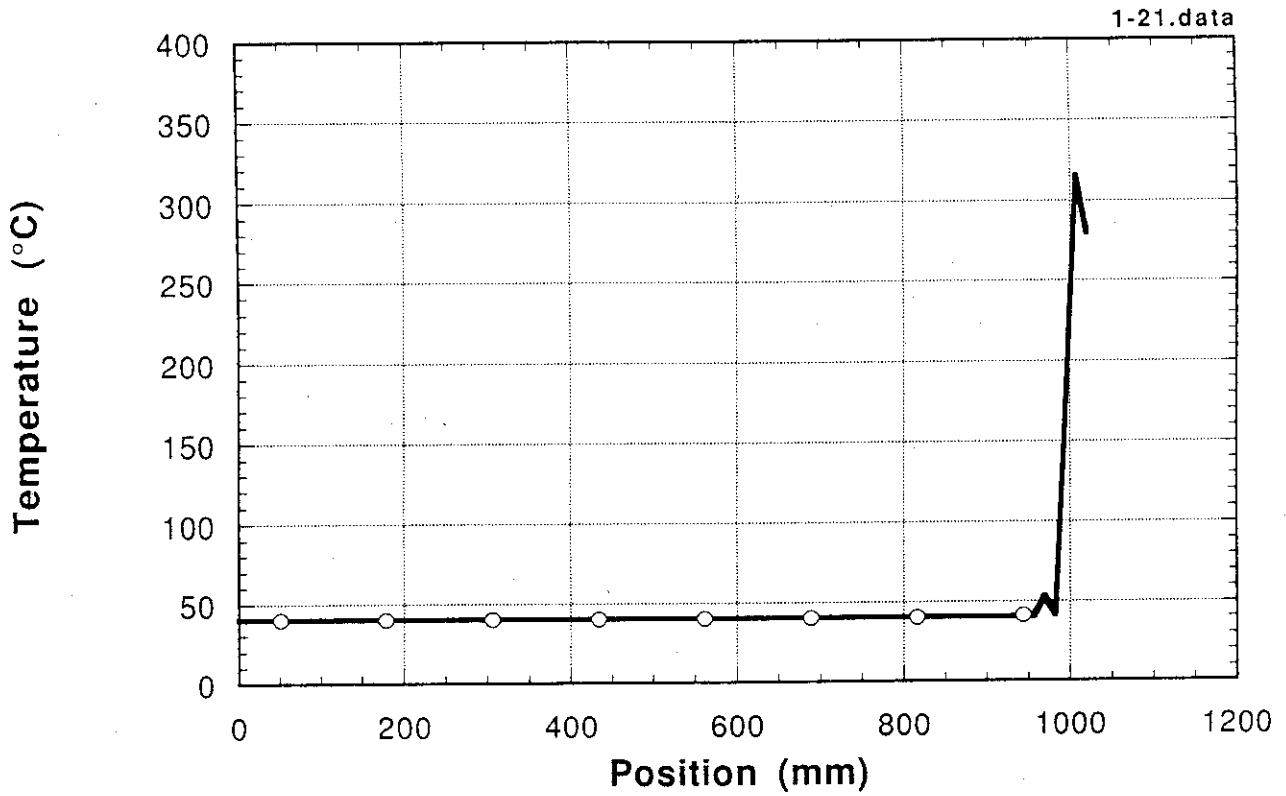
Fig. 19(A) Nodal temperature distribution obtained in CASE 1.
(upper part of the cooling tube)

1-21.data
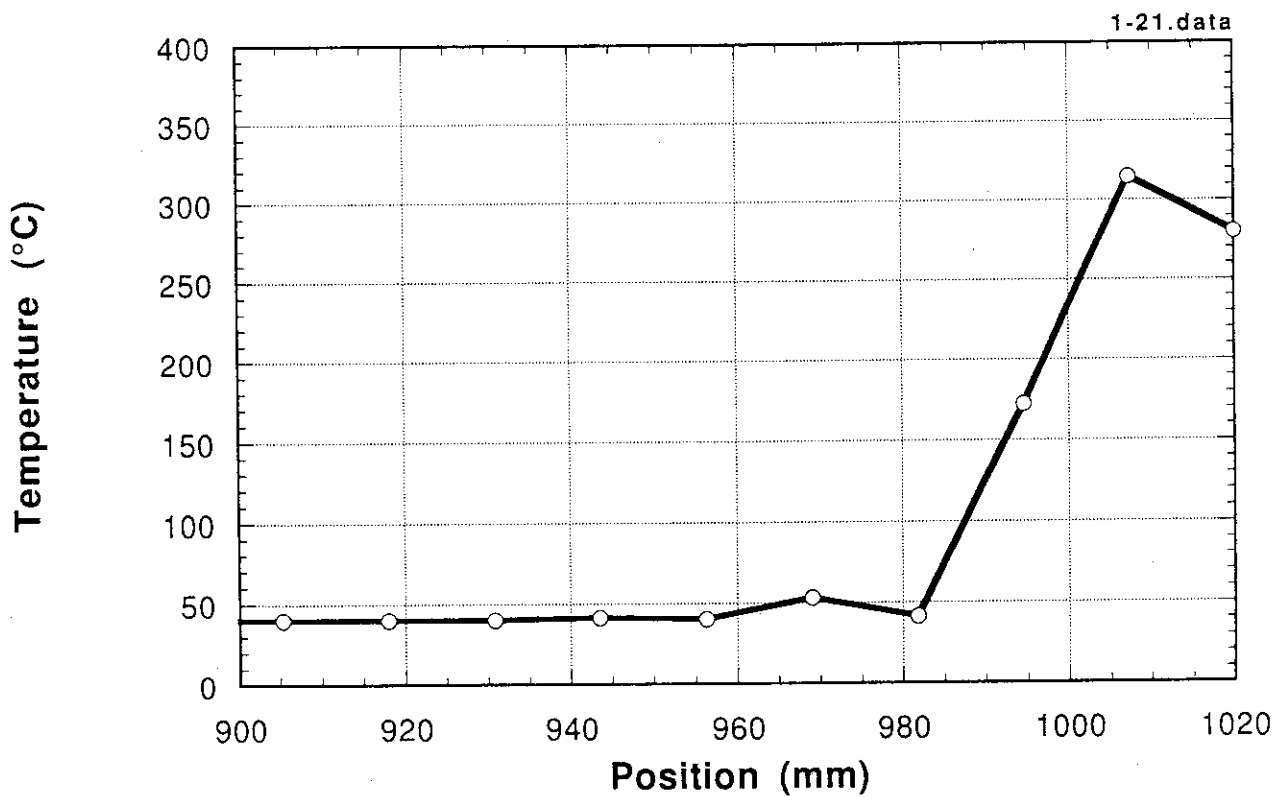
Fig. 19(B) Nodal temperature distribution obtained in CASE 2.
(upper part of the cooling tube)

1-23.data
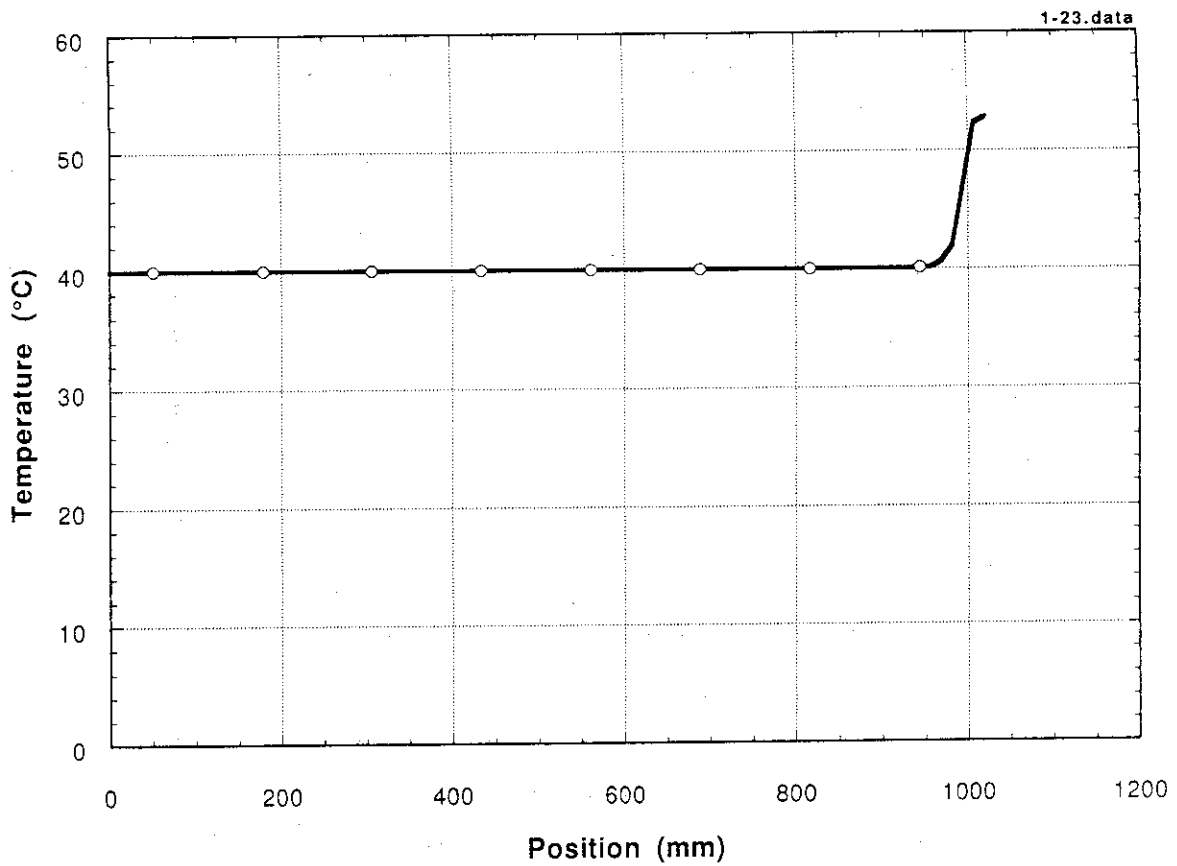
Fig. 19(C) Nodal temperature distribution obtained in CASE 1.

1-23.data
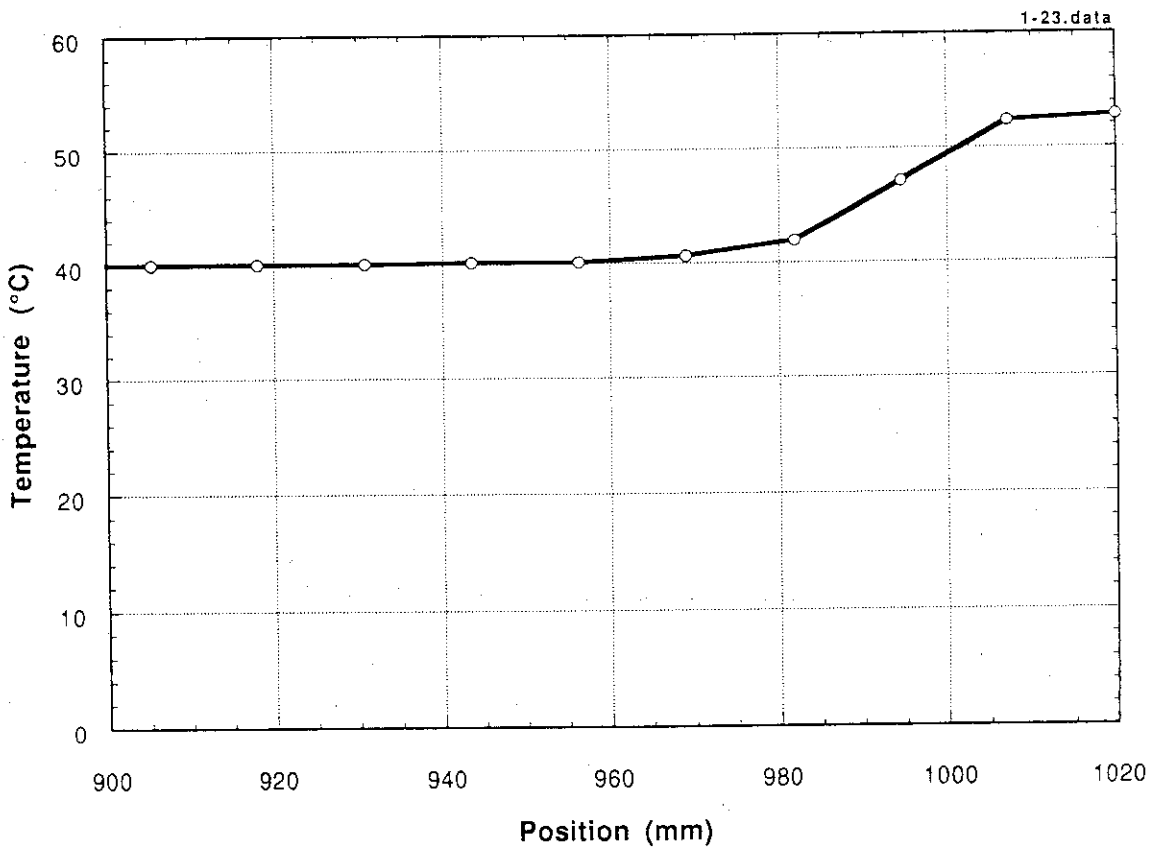
Fig. 19(D) Nodal temperature distribution obtained in CASE 1.
(lower part of the cooling tube)
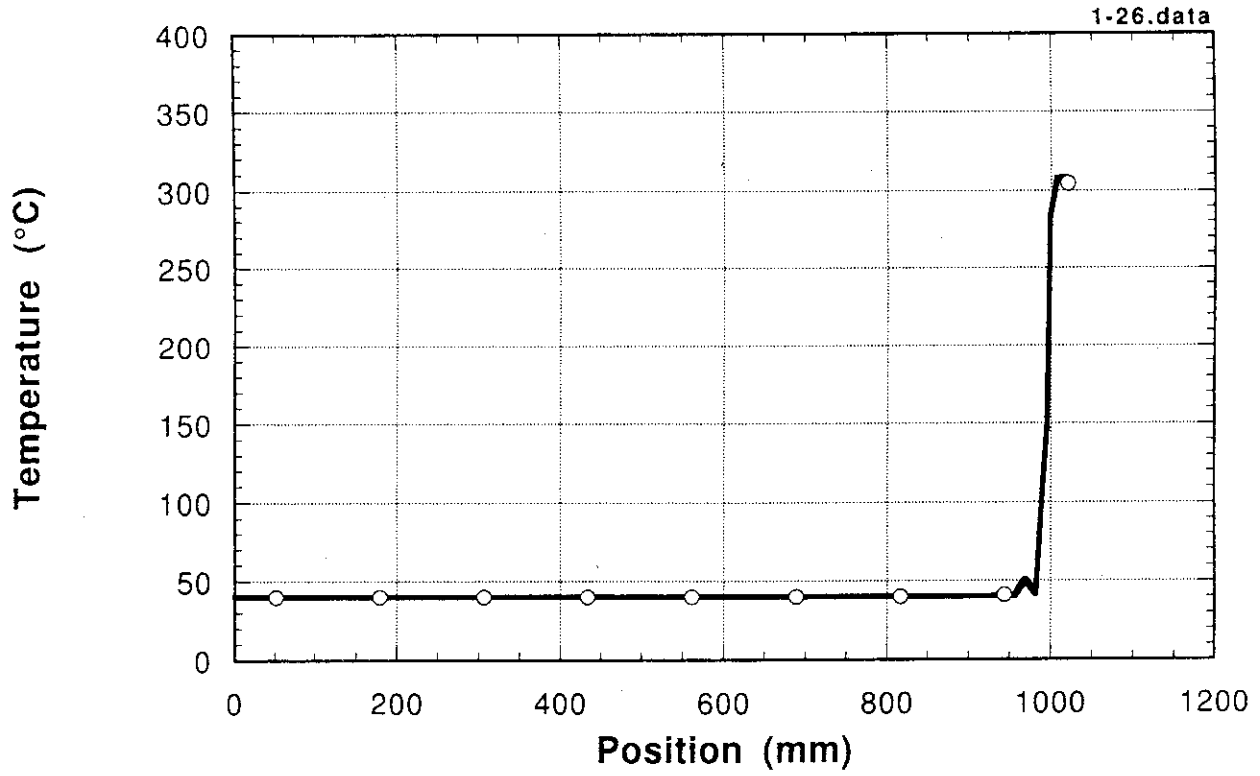
Fig. 20 (A) Nodal temperature distribution obtained in CASE 2.
(upper part of the cooling tube)
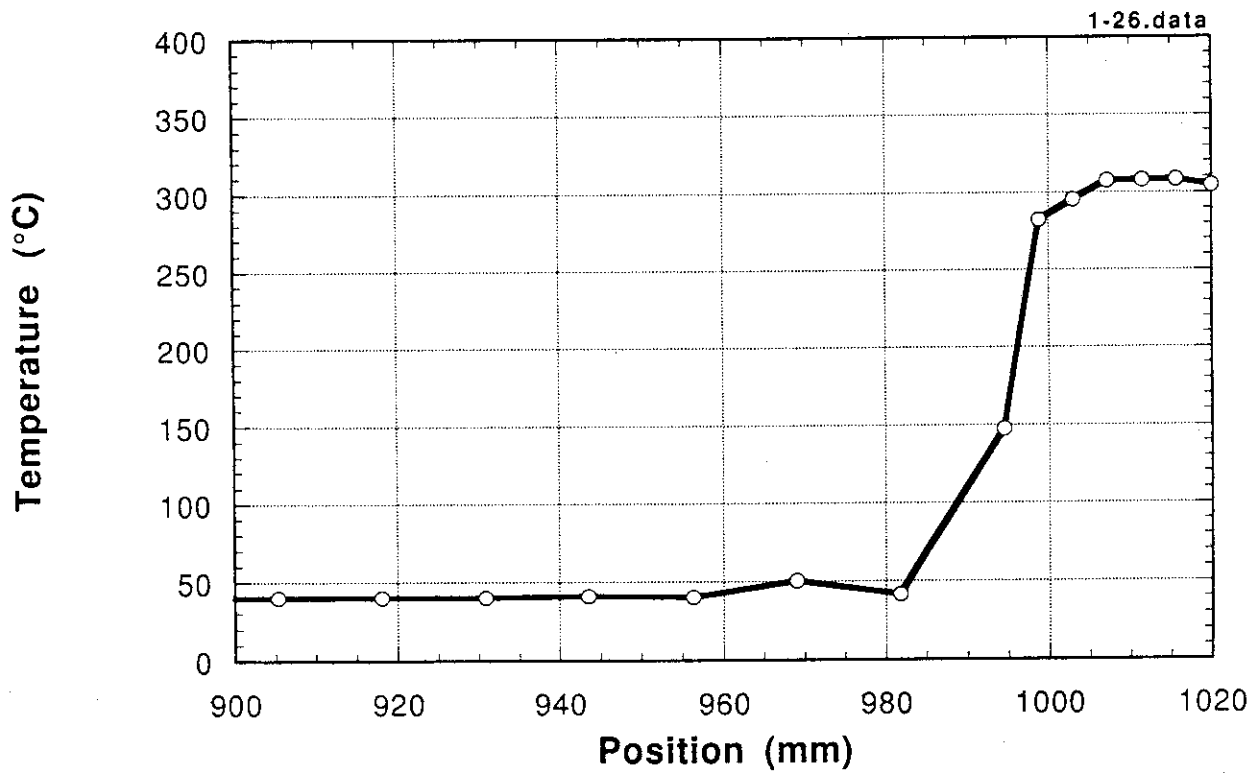
Fig. 20 (B) Nodal temperature distribution obtained in CASE 2.
(upper part of the cooling tube)

1-28.data
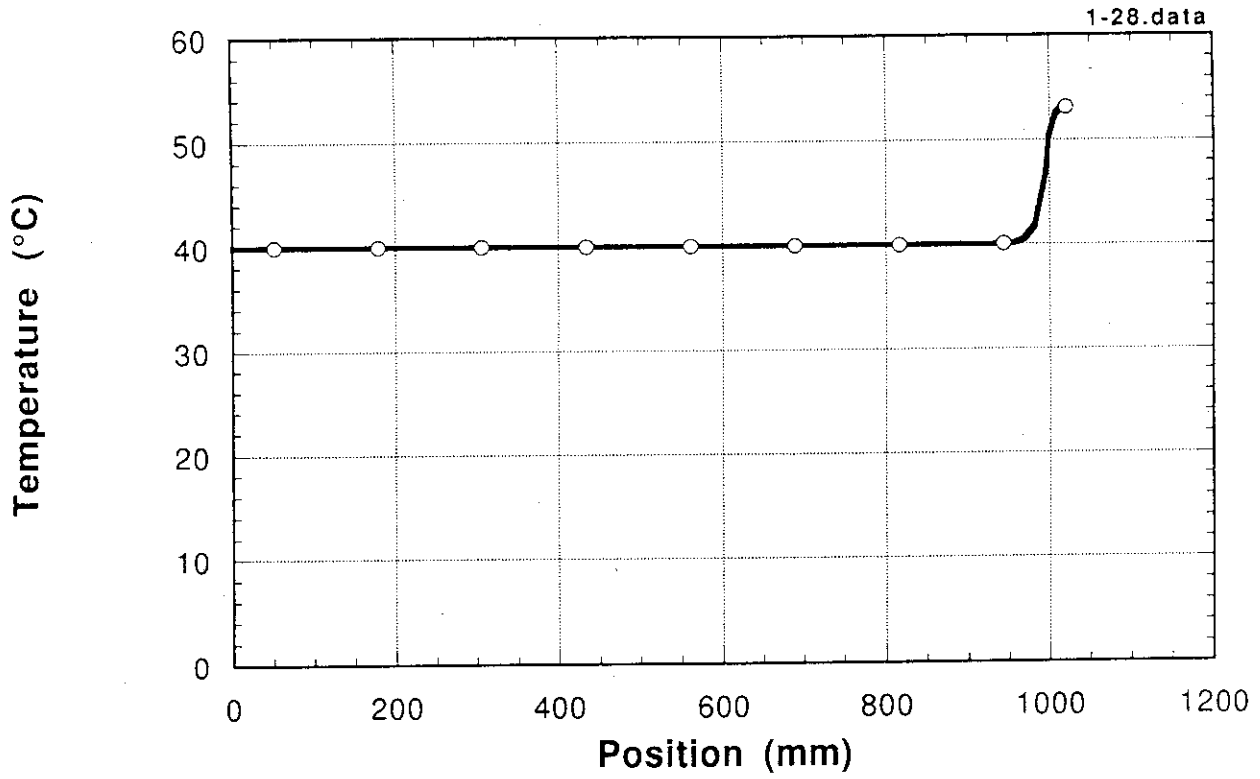
Fig. 20 (C) Nodal temperature distribution obtained in CASE 2.
(lower part of the cooling tube)

1-28.data
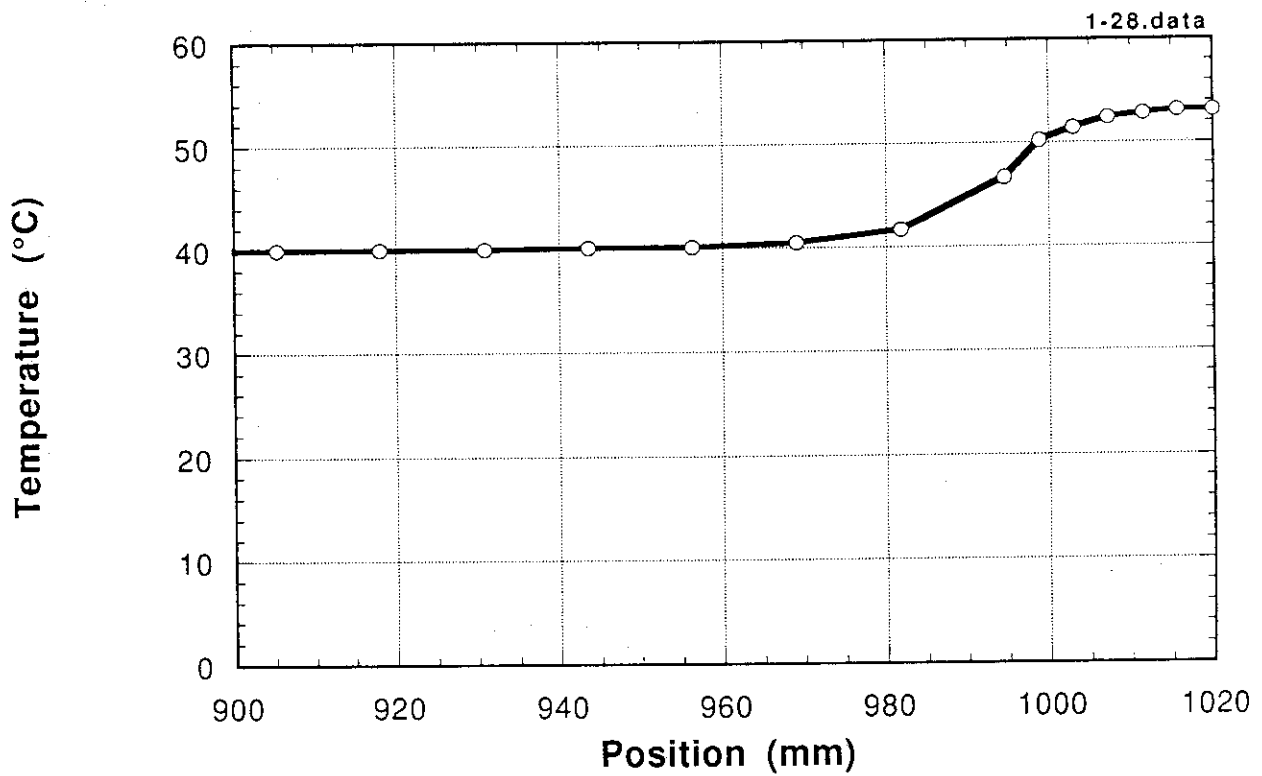
Fig. 20 (D) Nodal temperature distribution obtained in CASE 2.
(lower part of the cooling tube)

1-31.data
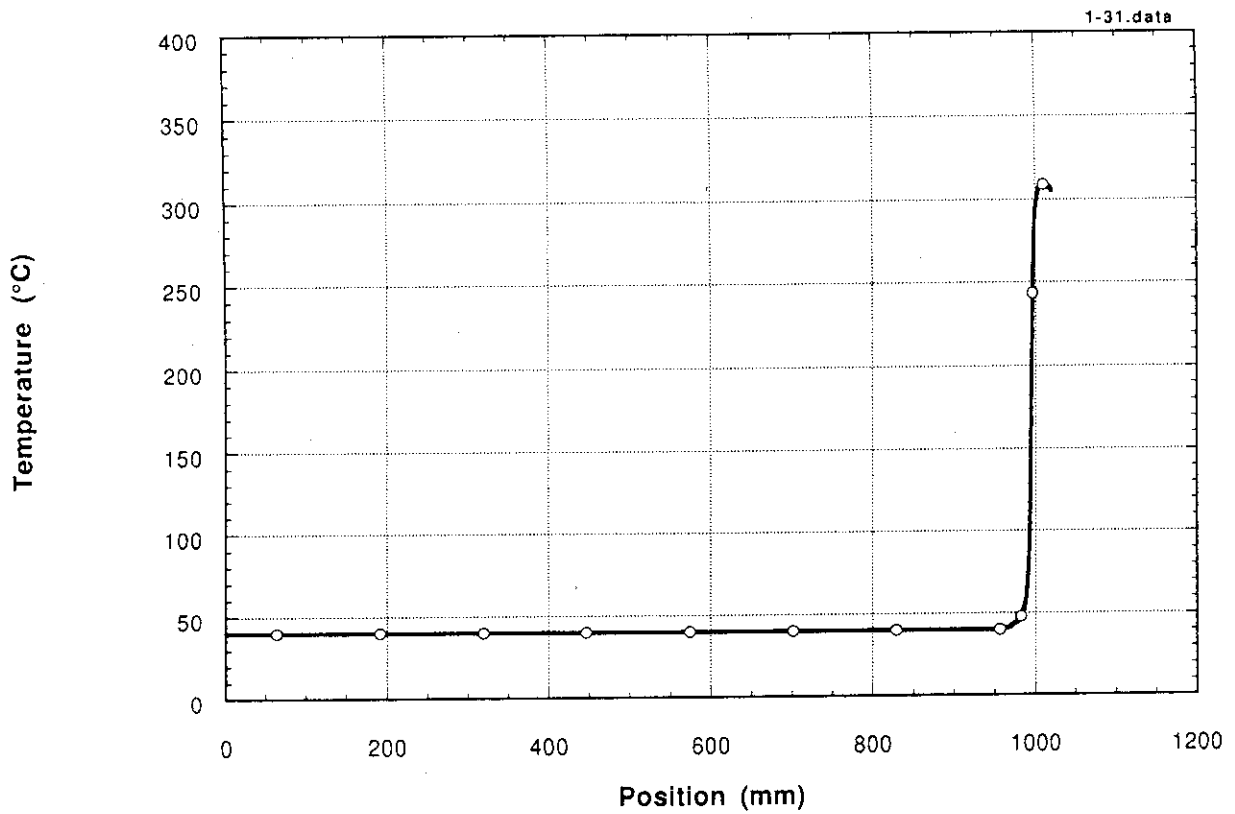
Fig. 21 (A) Nodal temperature distribution obtained in CASE 3.
(upper part of the cooling tube)

1-31.data
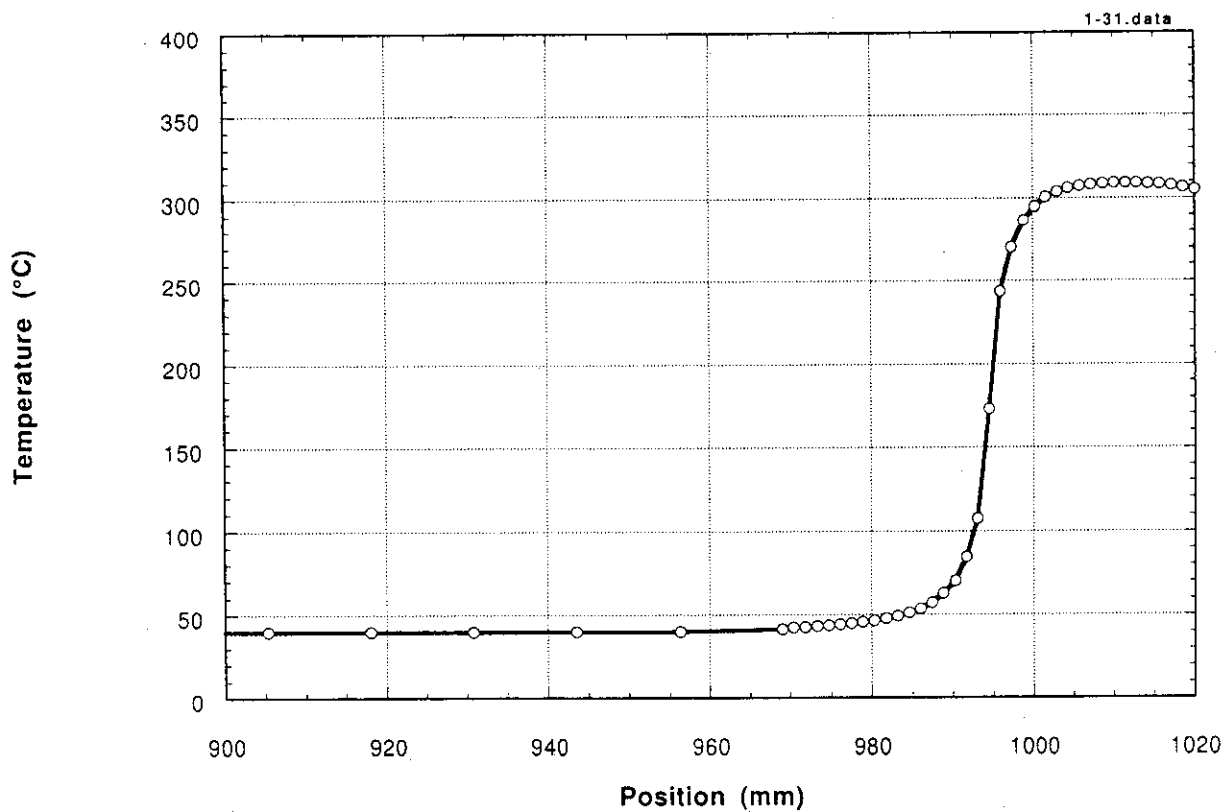
Fig. 21 (B) Nodal temperature distribution obtained in CASE 3.
(upper part of the cooling tube)
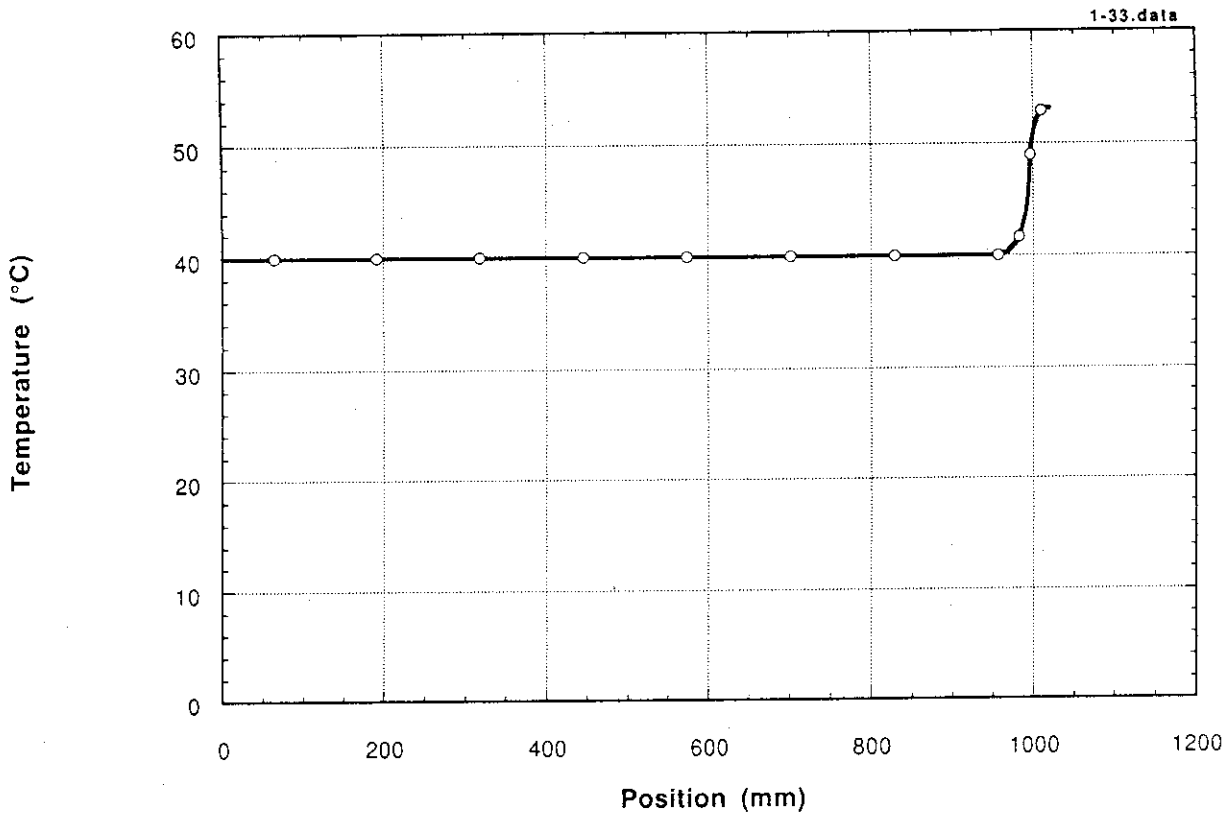
Fig. 21 (C) Nodal temperature distribution obtained in CASE 3.
(lower part of the cooling tube)
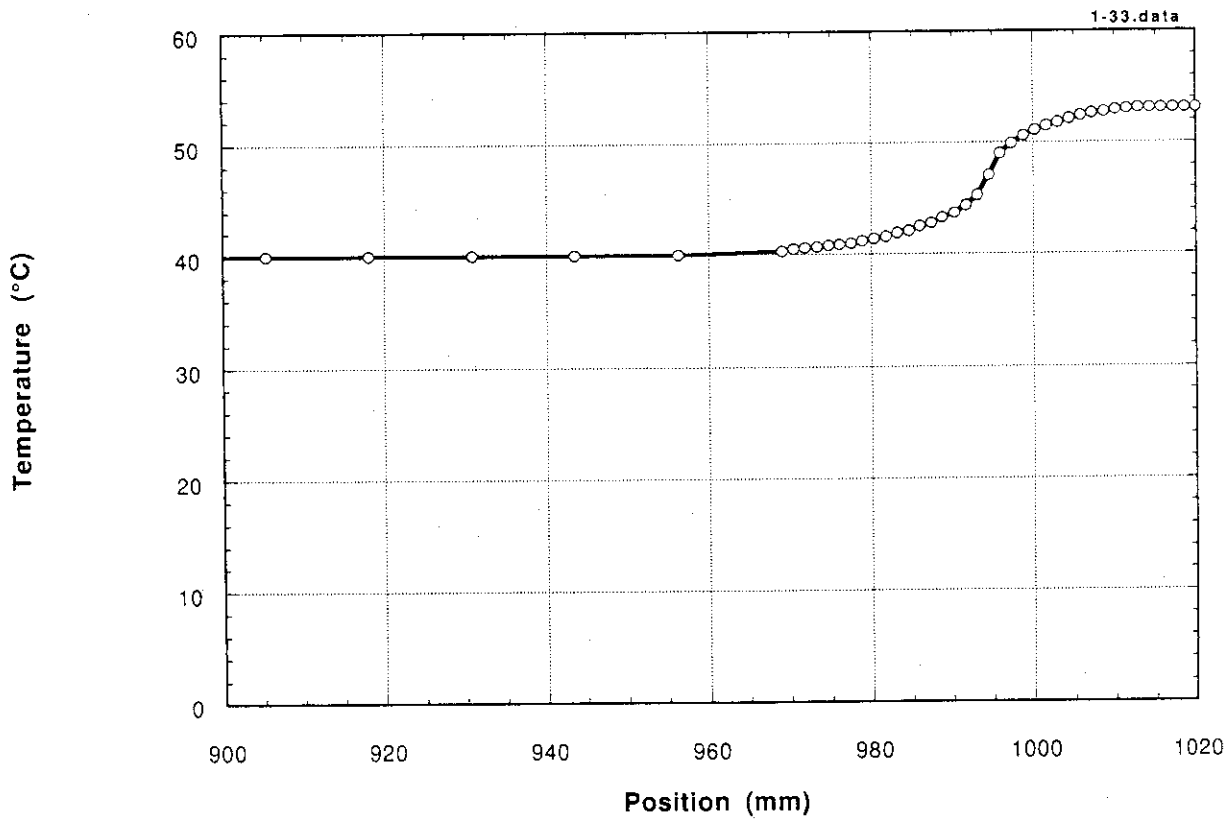
Fig. 21 (D) Nodal temperature distribution obtained in CASE 3.
(lower part of the cooling tube)
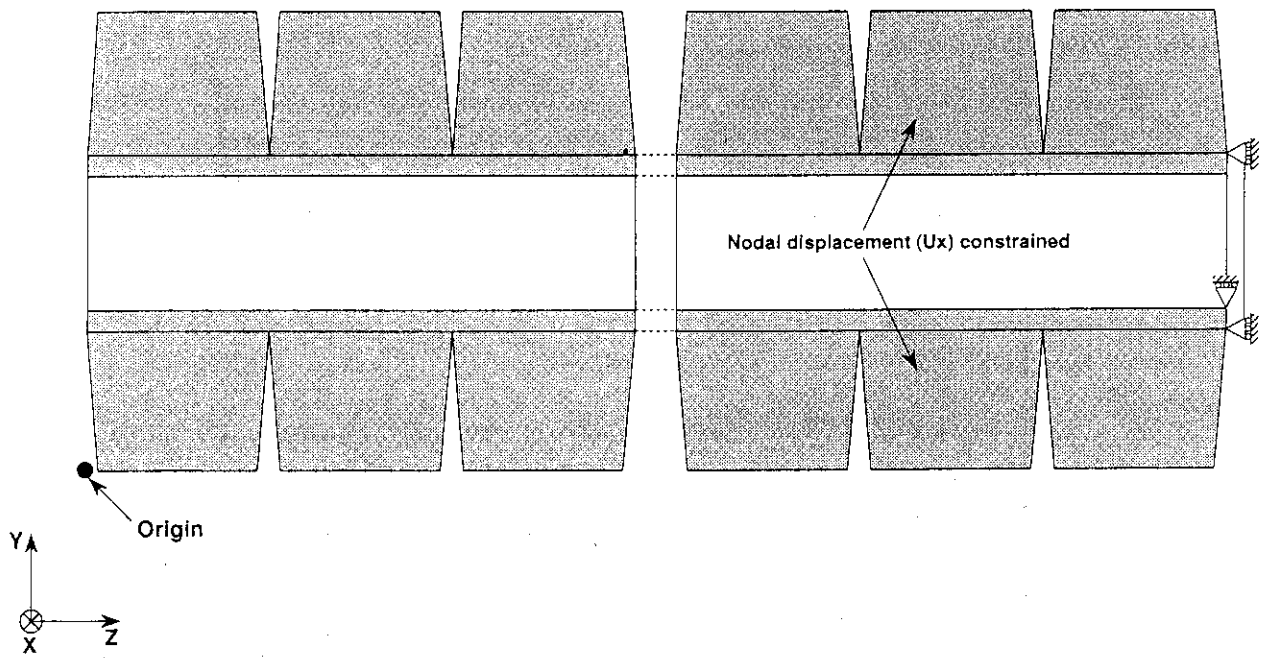
Fig. 22 (A) Mechanical boundary condition in YZ-plane
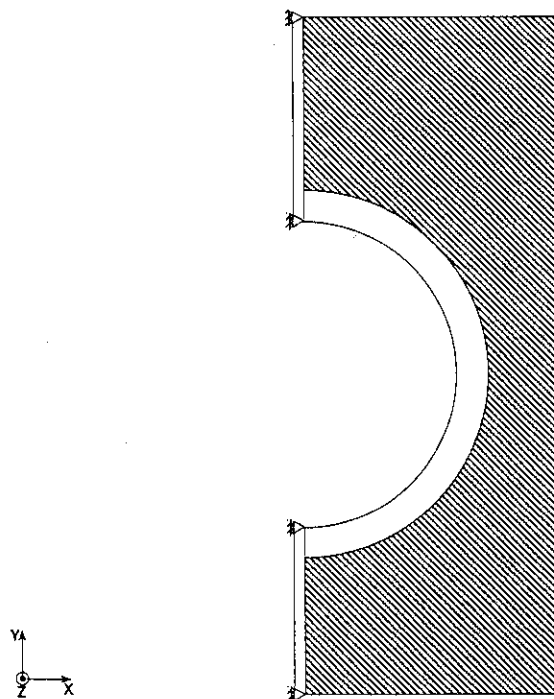
Fig. 22 (B) Mechanical boundary condition in XY-plane
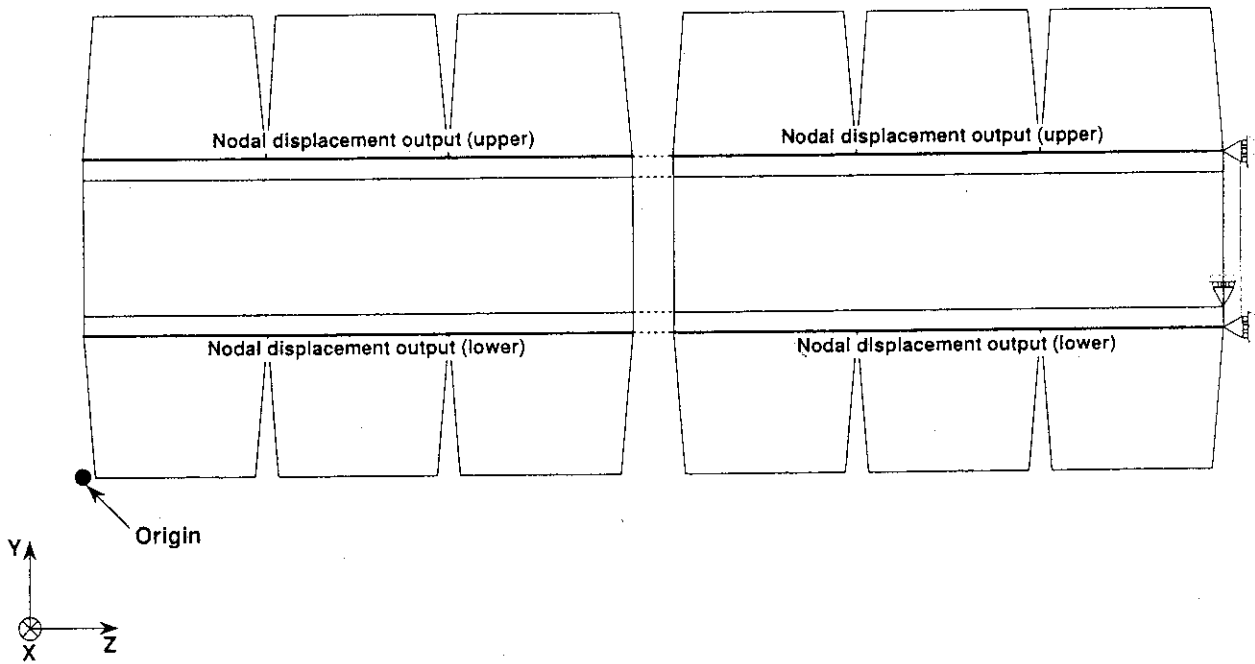
Fig. 23   Node sets to be output in stress analyses
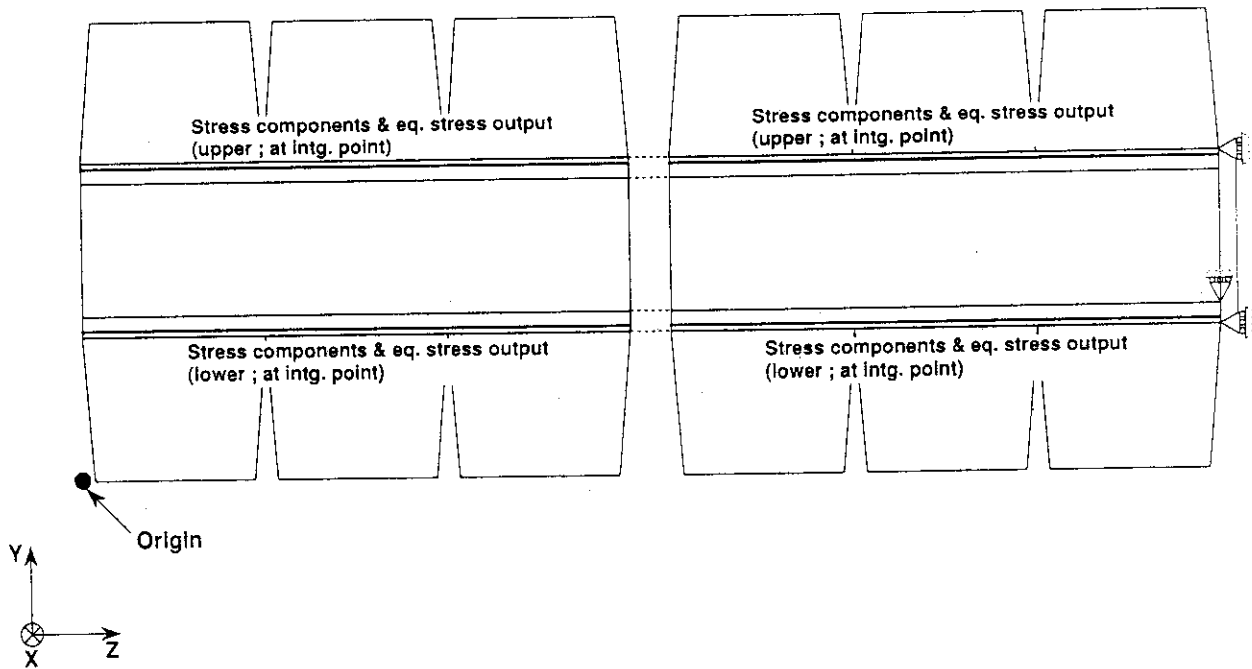
Fig. 24   Element sets to be output in stress analyses
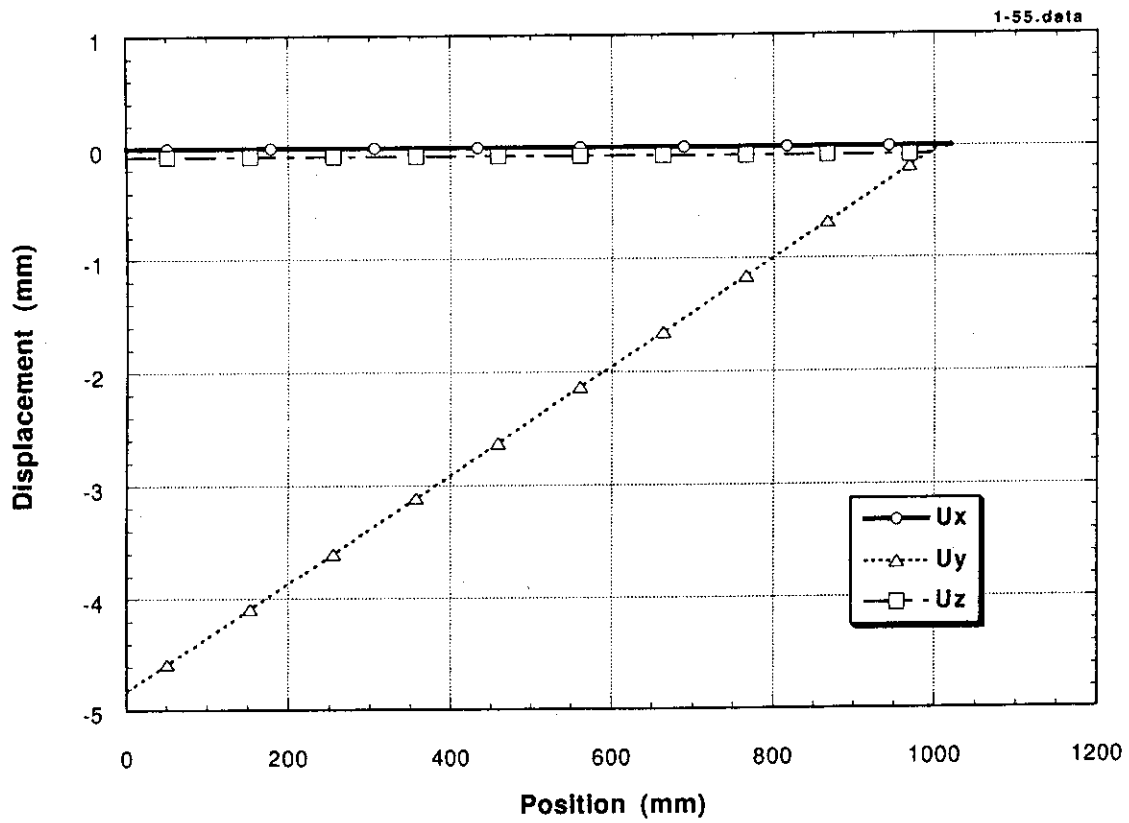
Fig. 25 Thermal deformation obtained in CASE 1
(upper part of the cooling tube)
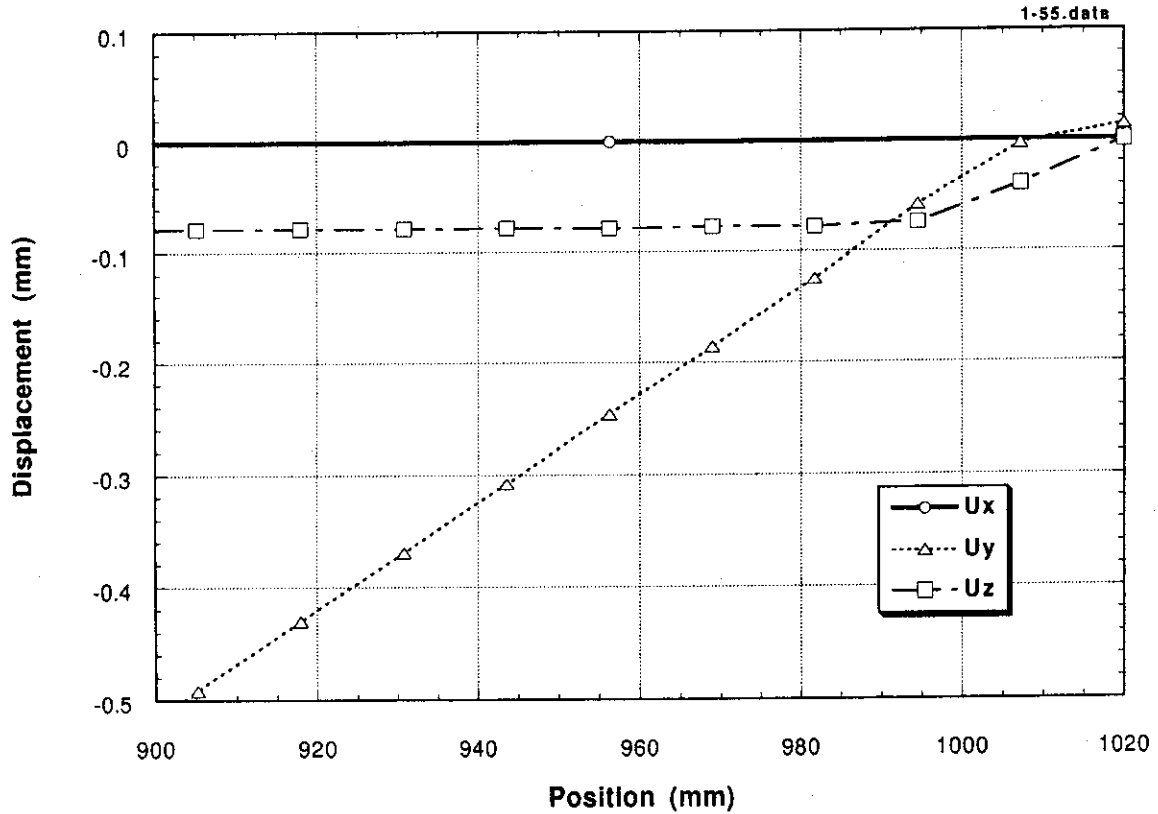
Fig. 26 Thermal deformation at selected points in CASE 1
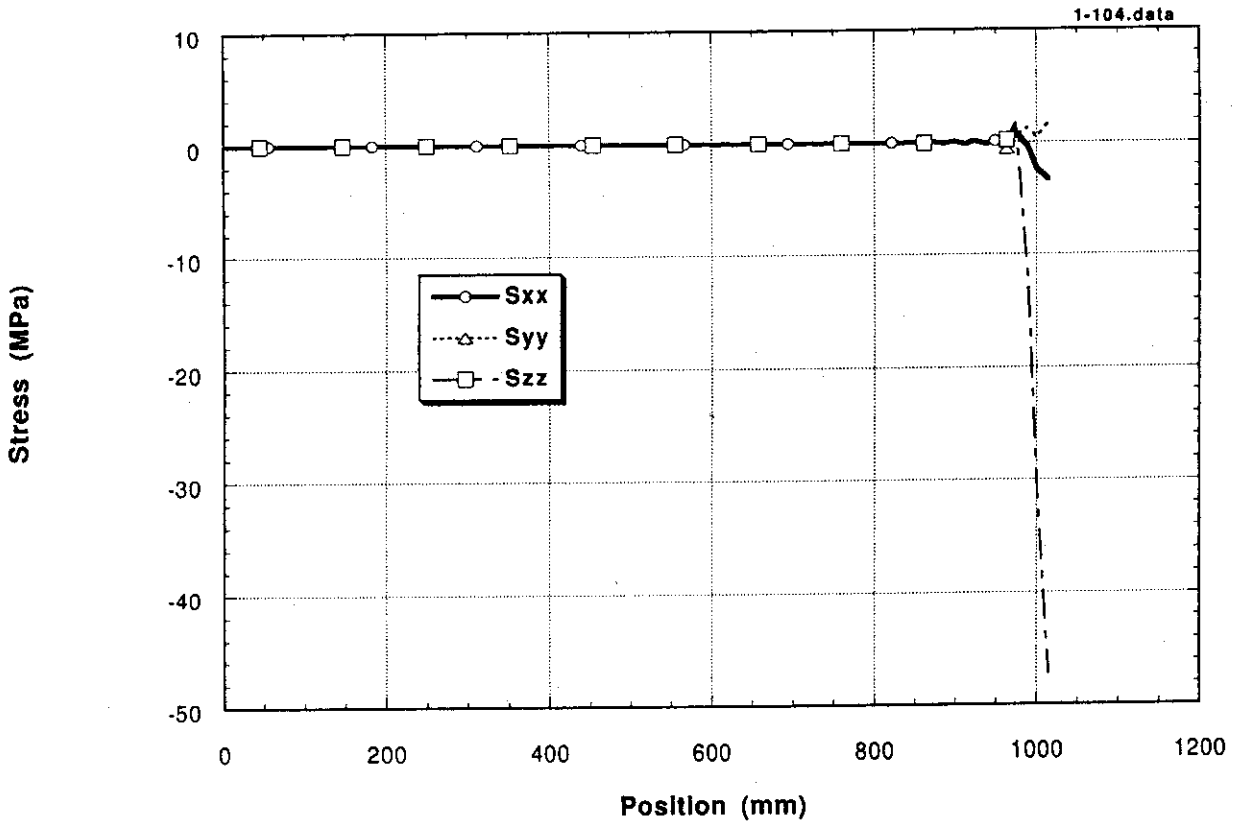(upper part of the cooling tube)
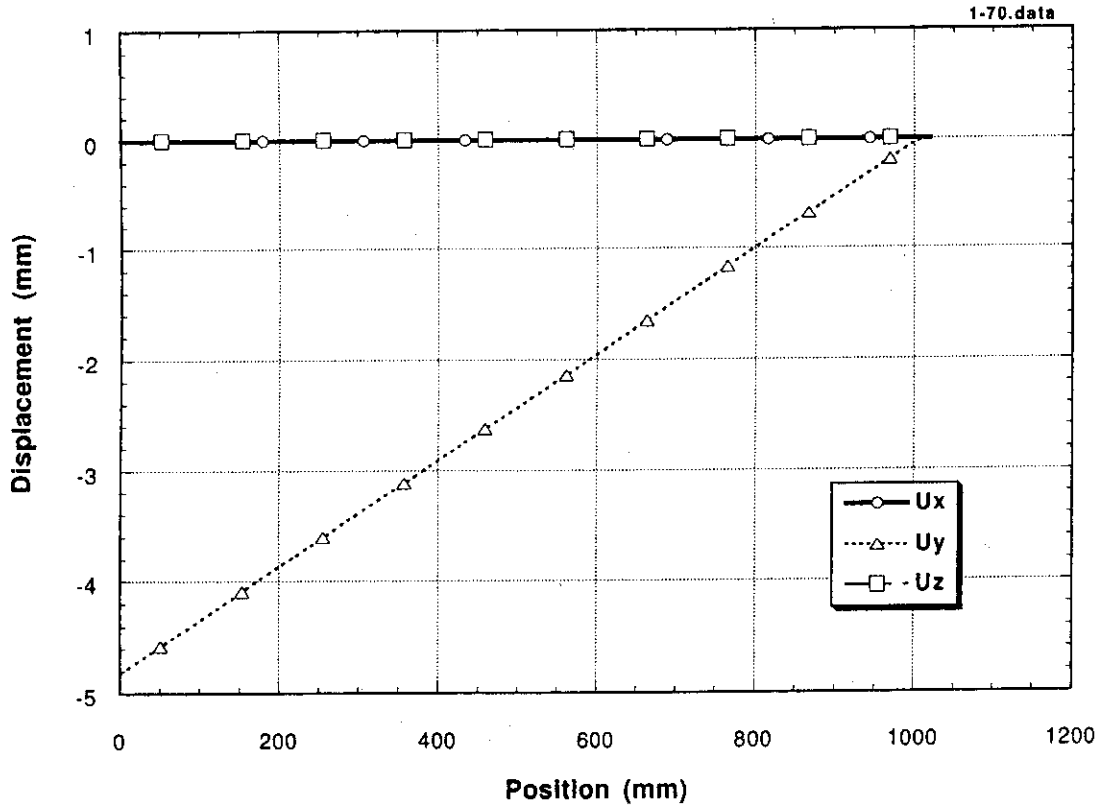
Fig. 27　Thermal deformation obtained in CASE 1
(lower part of the cooling tube)
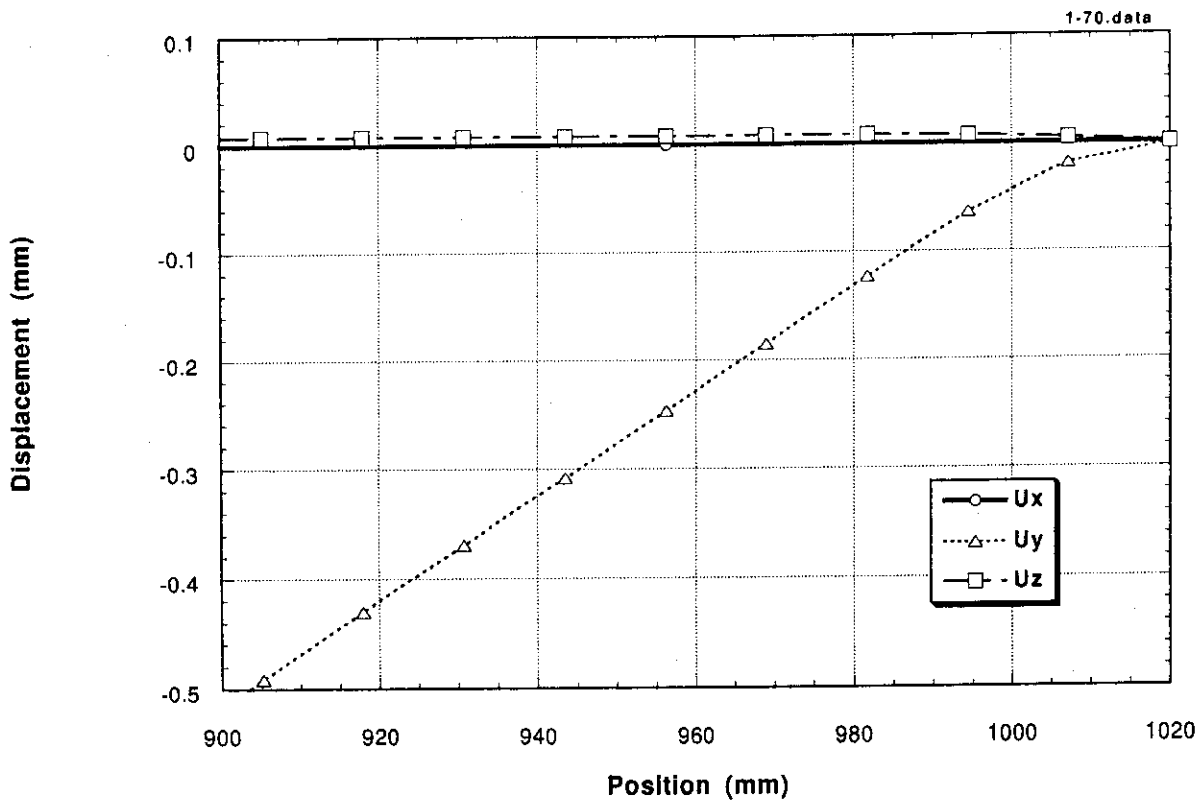
Fig. 28　Thermal deformation at selected points in CASE 1
(lower part of the cooling tube)
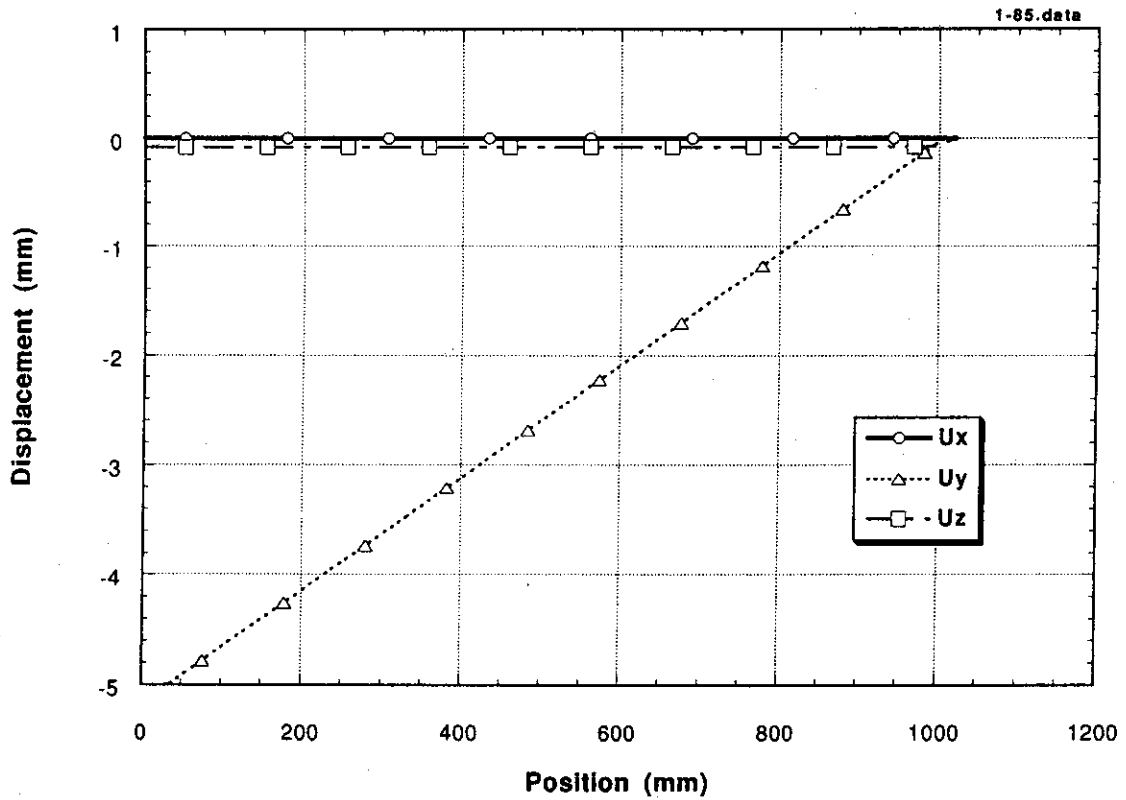
Fig. 29   Thermal deformation obtained in CASE 2
(upper part of the cooling tube)
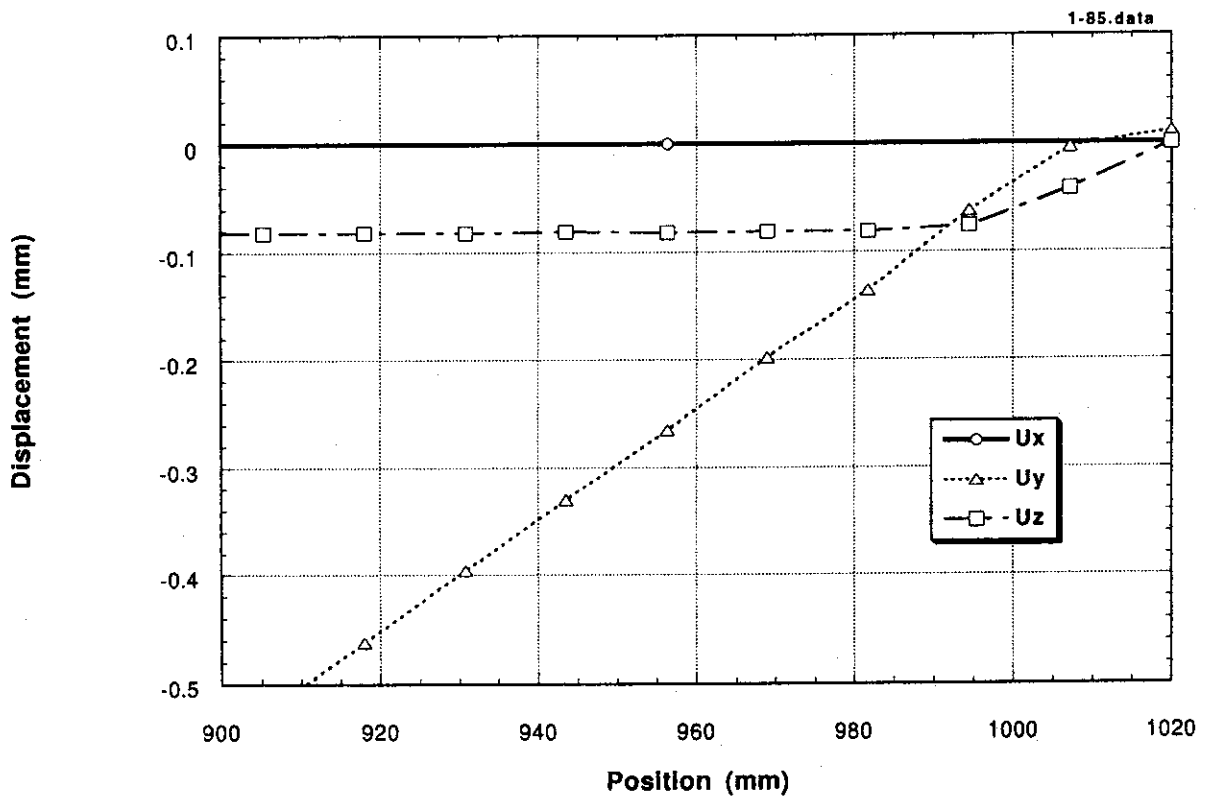
Fig. 30   Thermal deformation at selected points in CASE 2
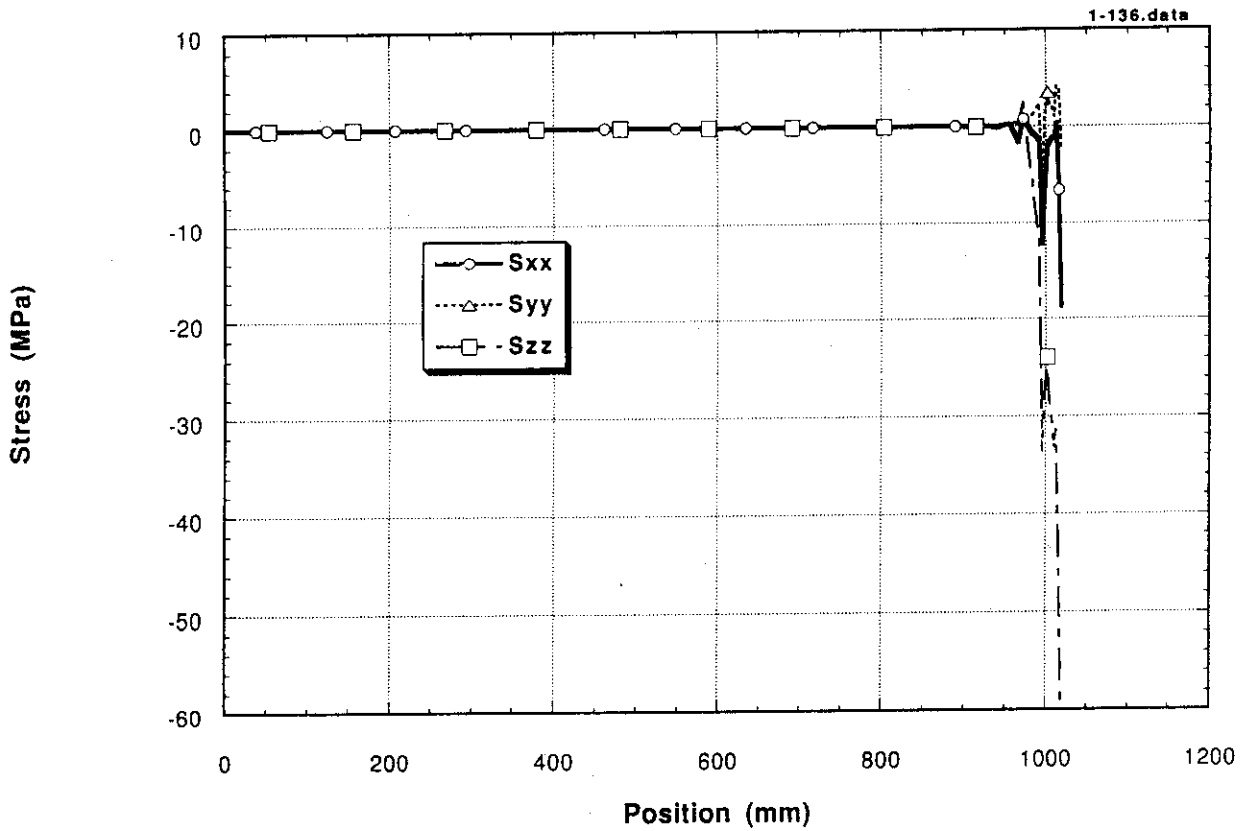(upper part of the cooling tube)
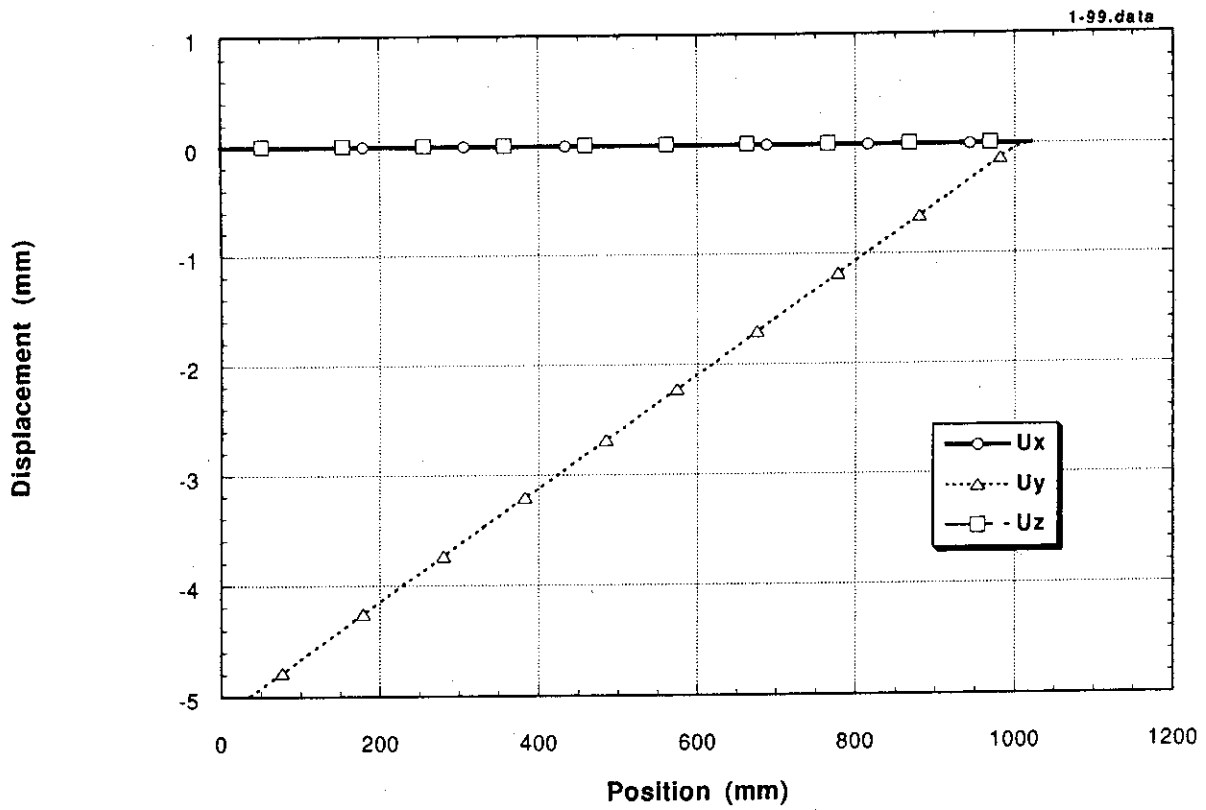
Fig. 31   Thermal deformation obtained in CASE 2
(lower part of the cooling tube)
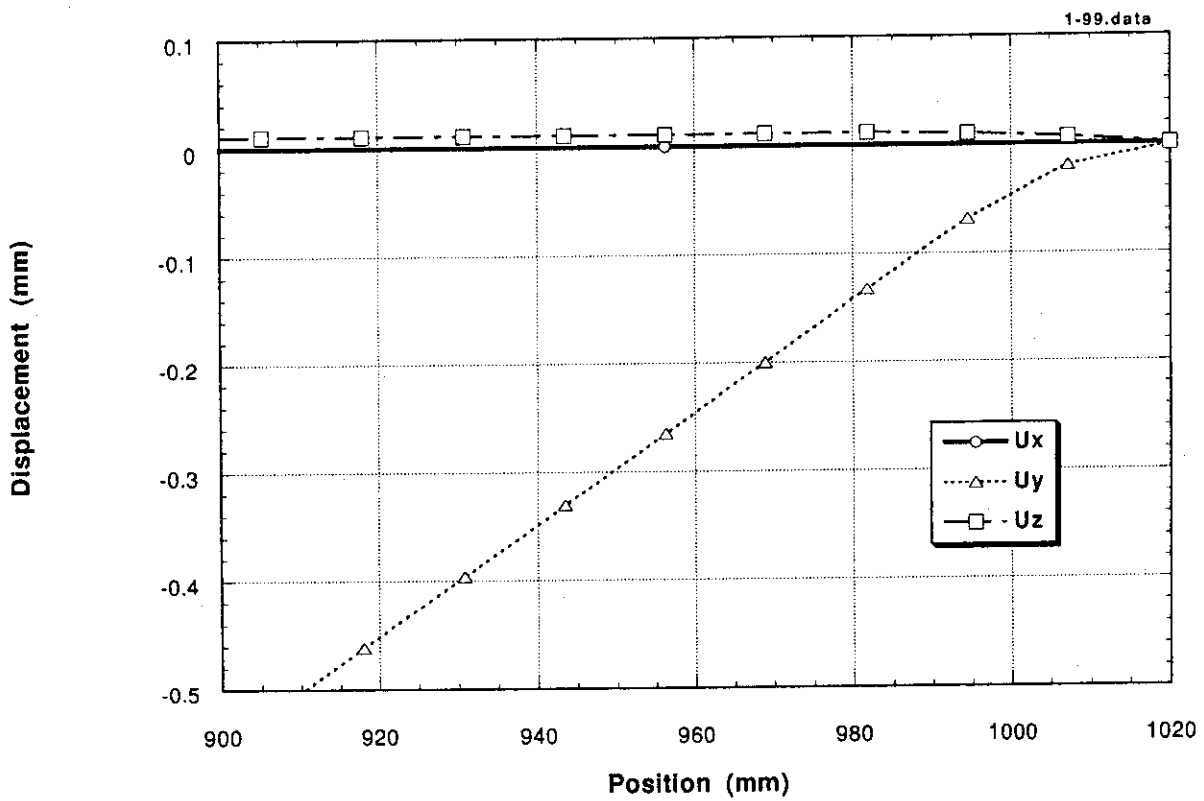
Fig. 32   Thermal deformation at selected points in CASE 2
(lower part of the cooling tube)
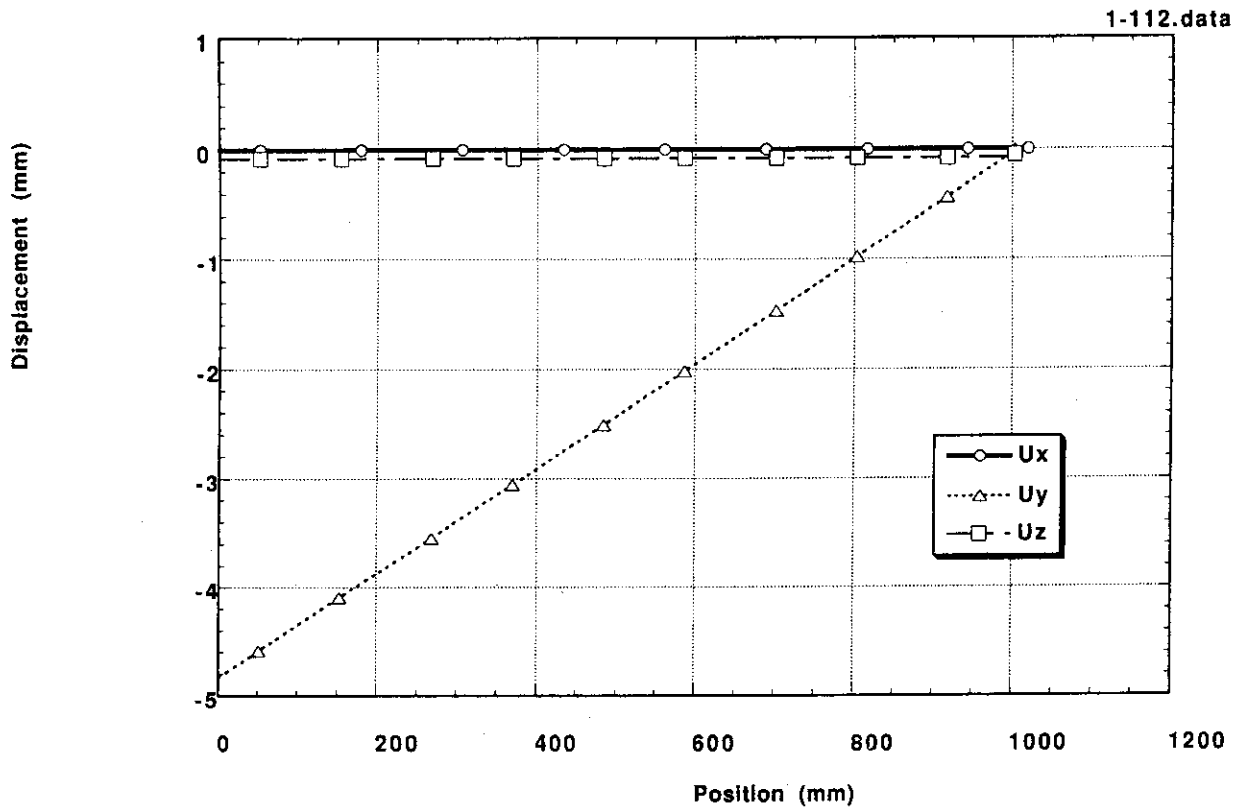
Fig. 33 Thermal deformation obtained in CASE 3
(upper part of the cooling tube)
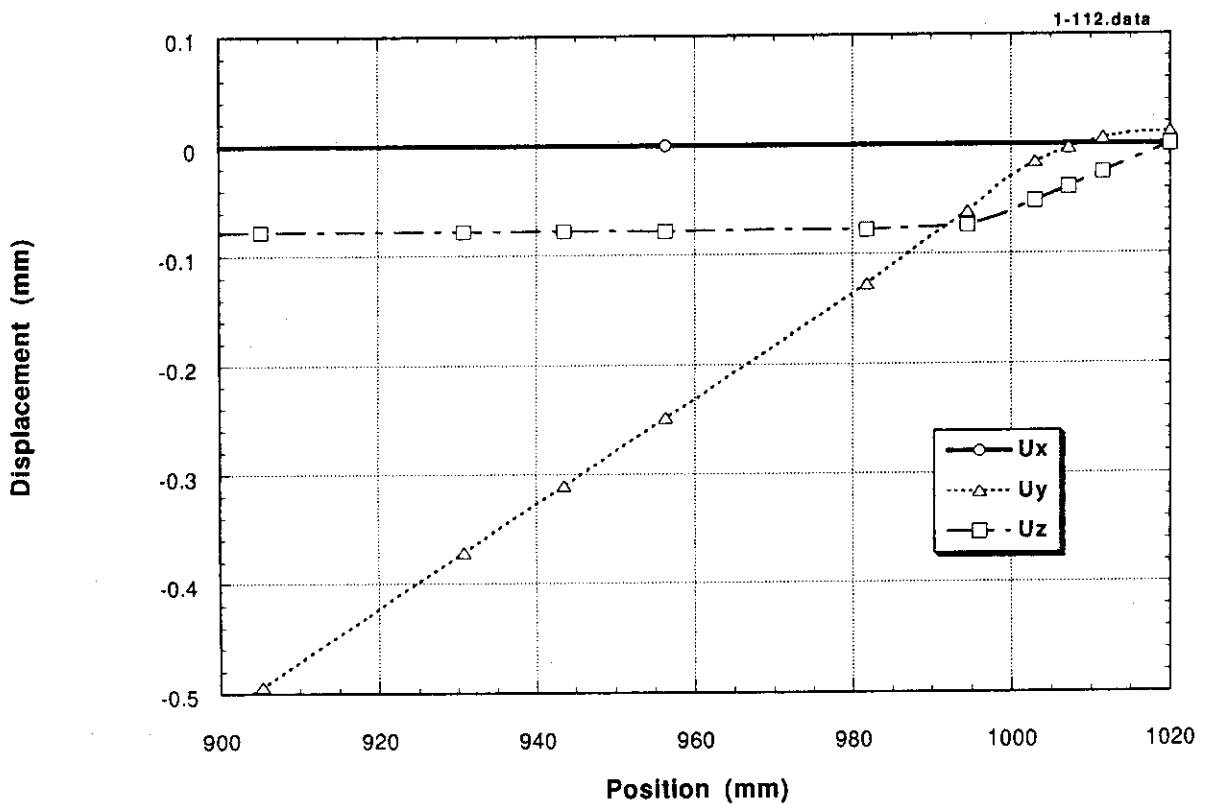
Fig. 34 Thermal deformation at selected points in CASE 3
(upper part of the cooling tube)
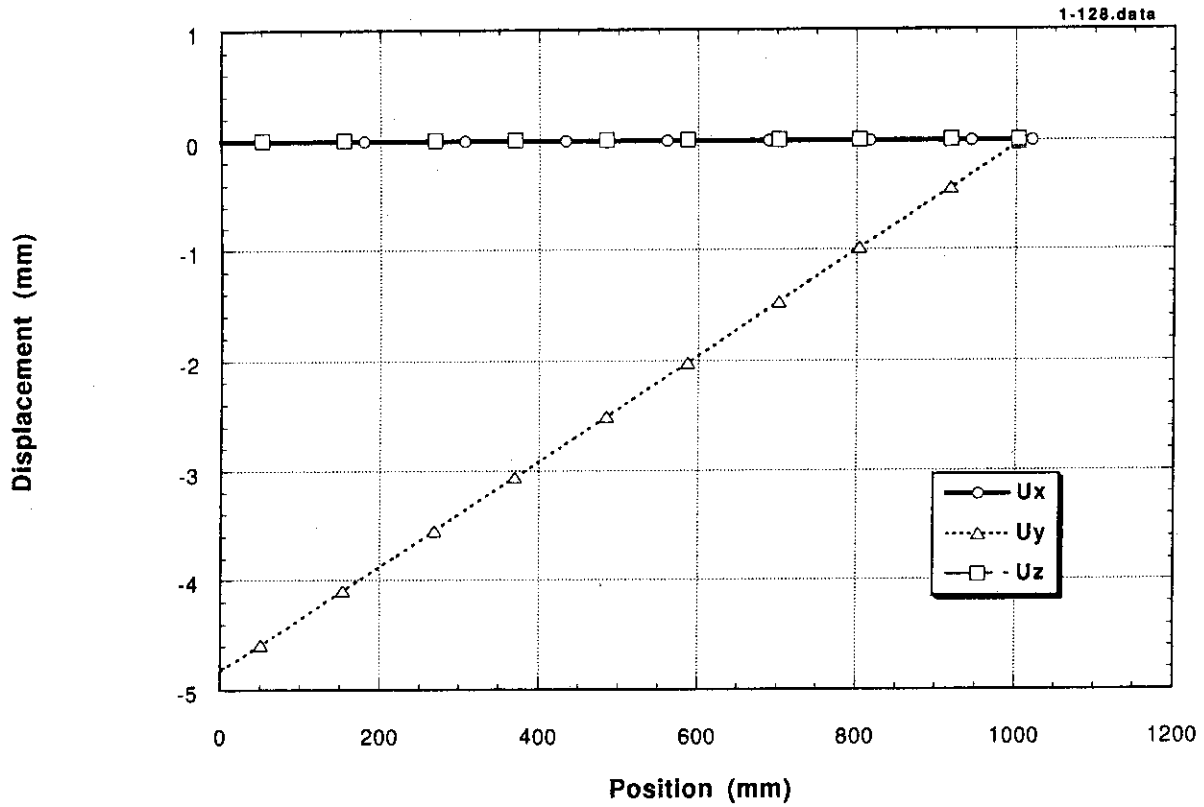
Fig. 35   Thermal deformation obtained in CASE 3
(lower part of the cooling tube)
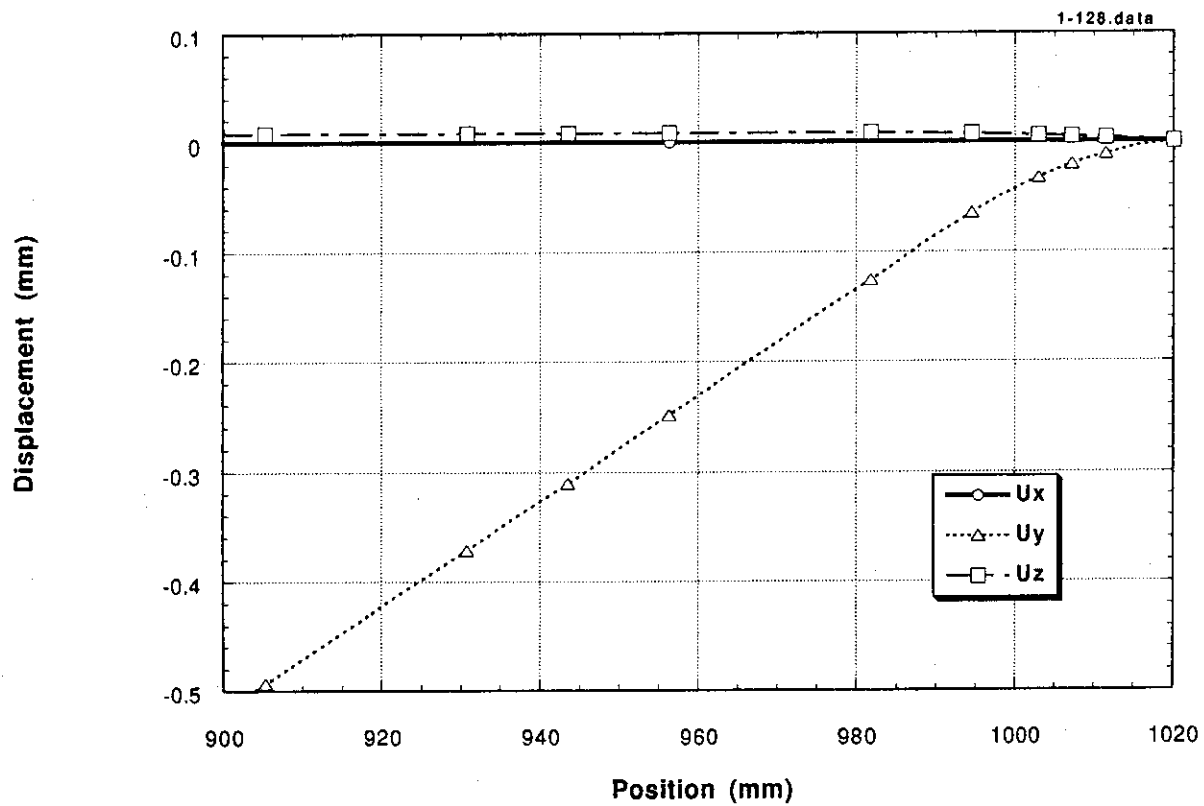
Fig. 36   Thermal deformation at selected points in CASE 3
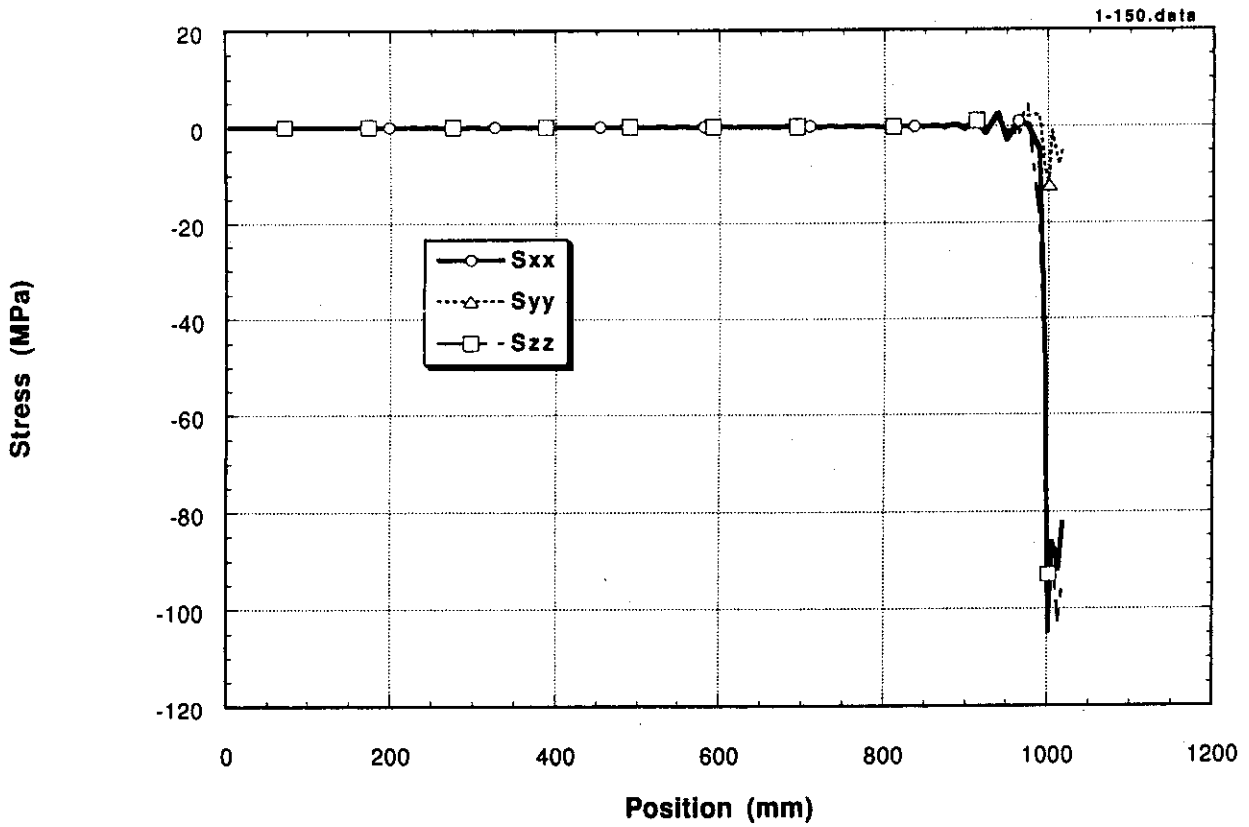(lower part of the cooling tube)
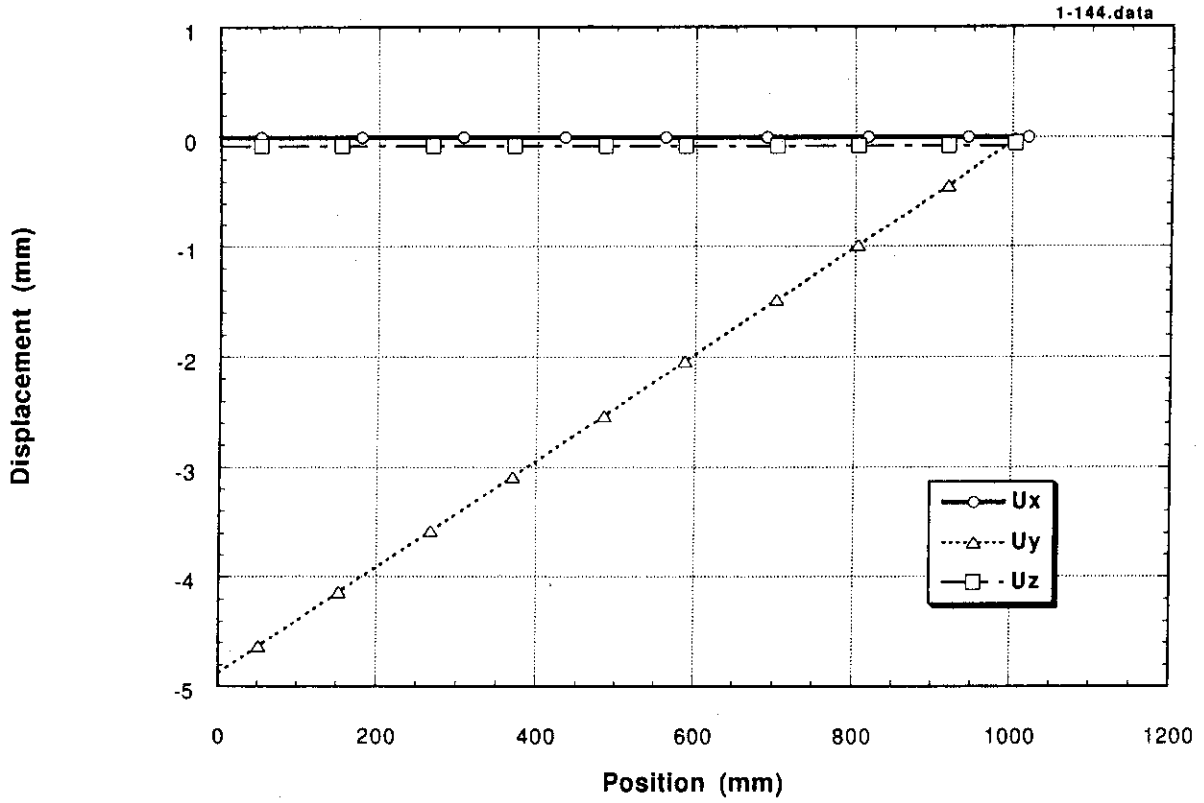
Fig. 37   Thermal deformation obtained in CASE 4
(upper part of the cooling tube)
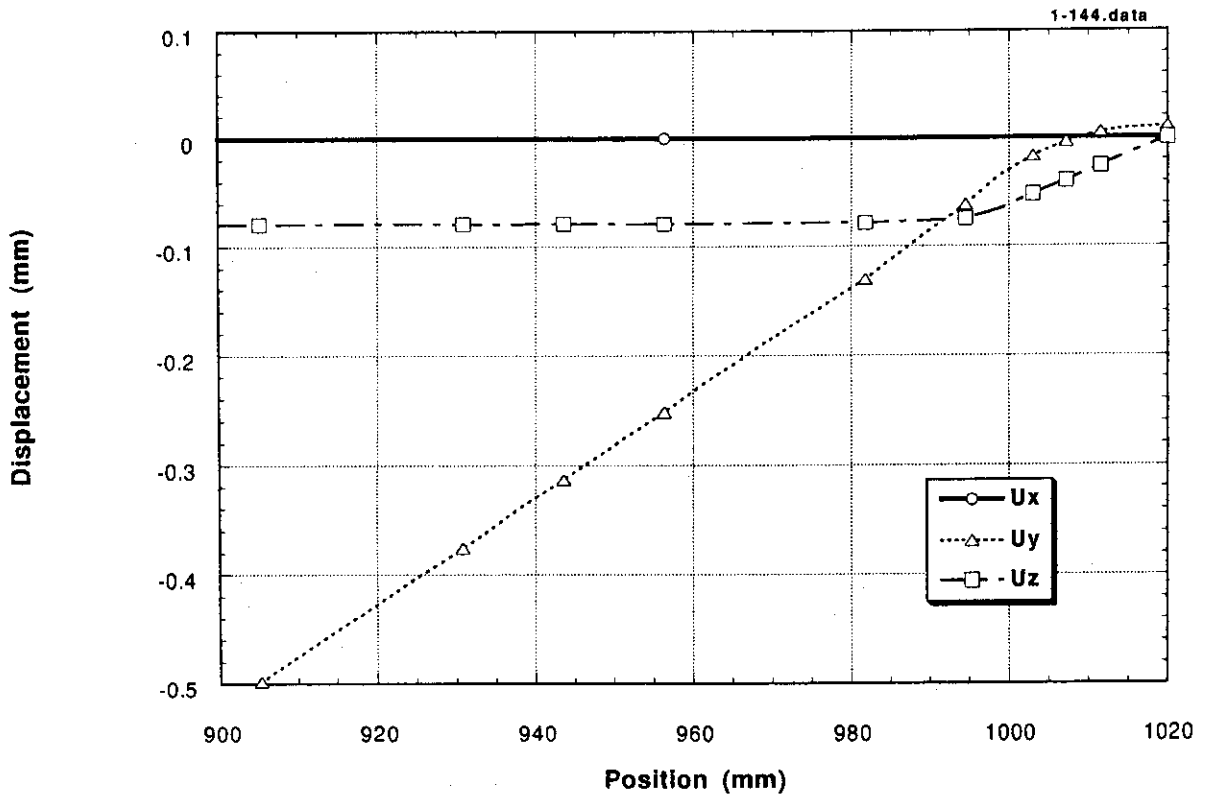
Fig. 38   Thermal deformation at selected points in CASE 4
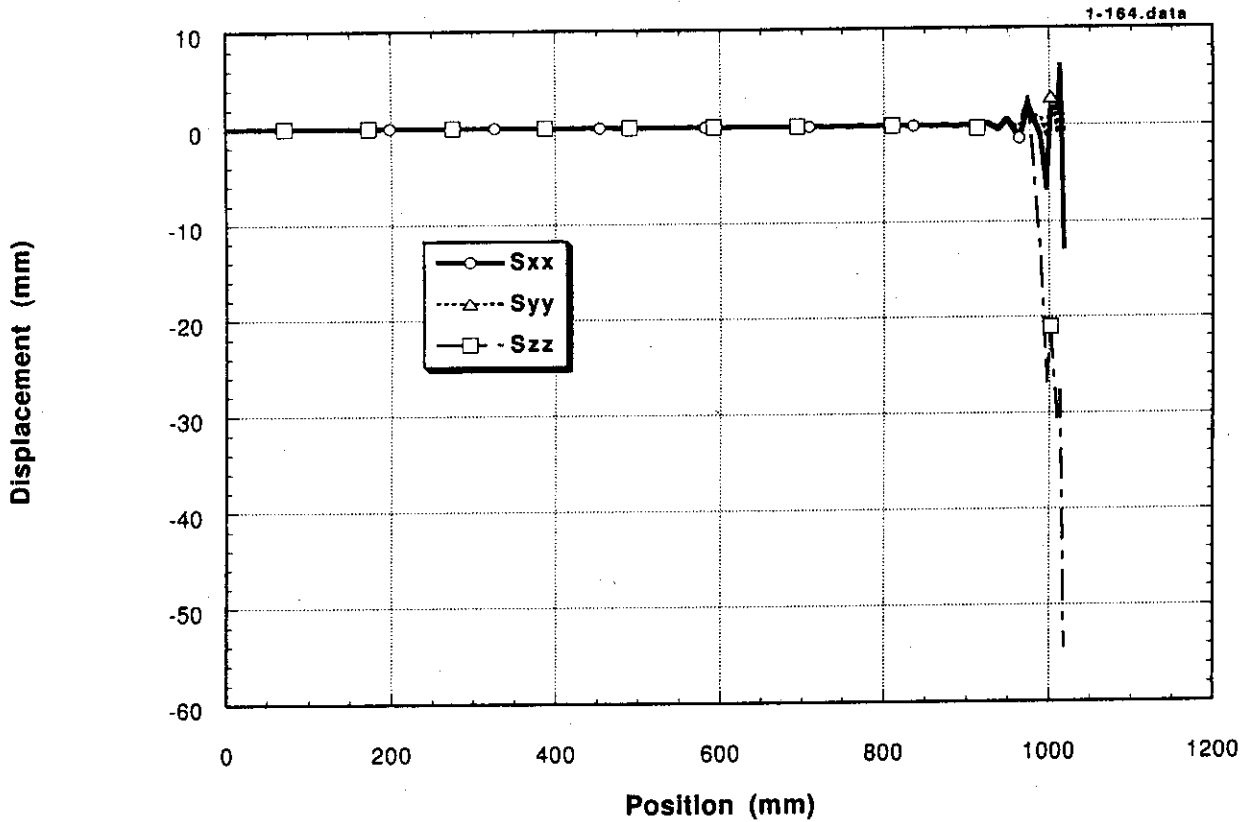(upper part of the cooling tube)

1-158.data
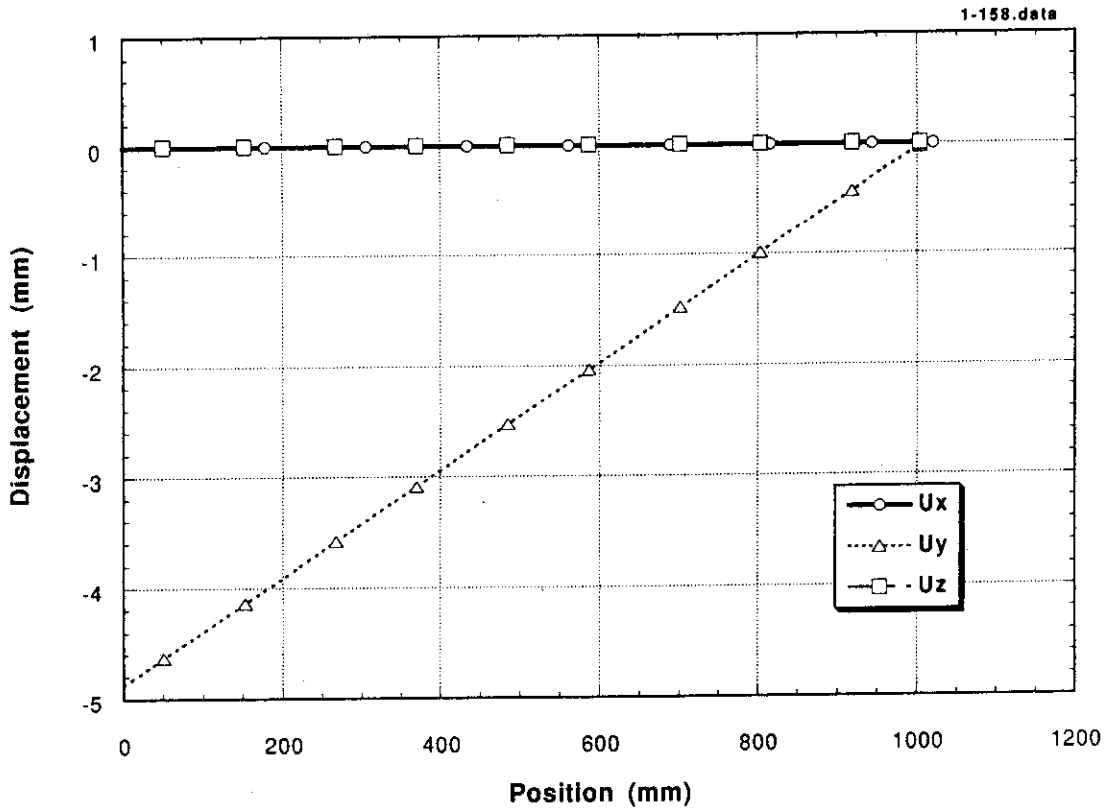
Fig. 39 Thermal deformation obtained in CASE 4
(lower part of the cooling tube)

1-158.data
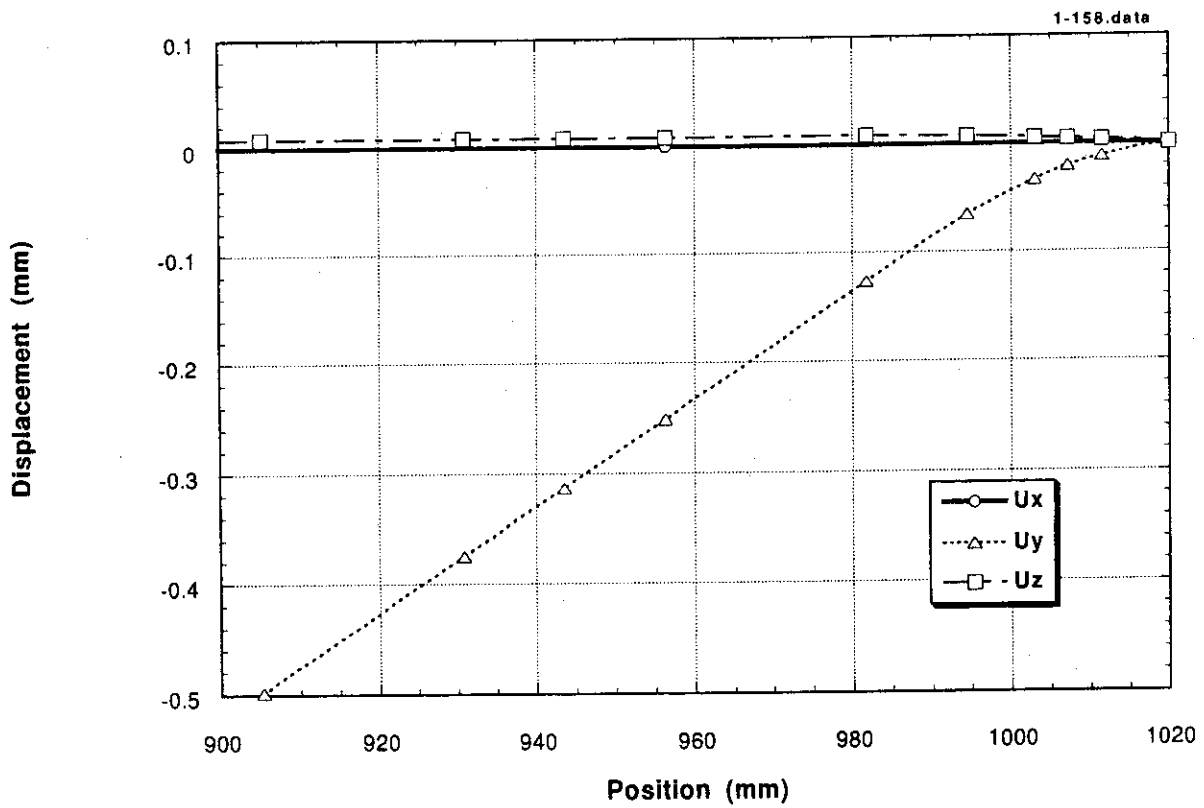
Fig. 40 Thermal deformation at selected points in CASE 4
(lower part of the cooling tube)

1-173.data
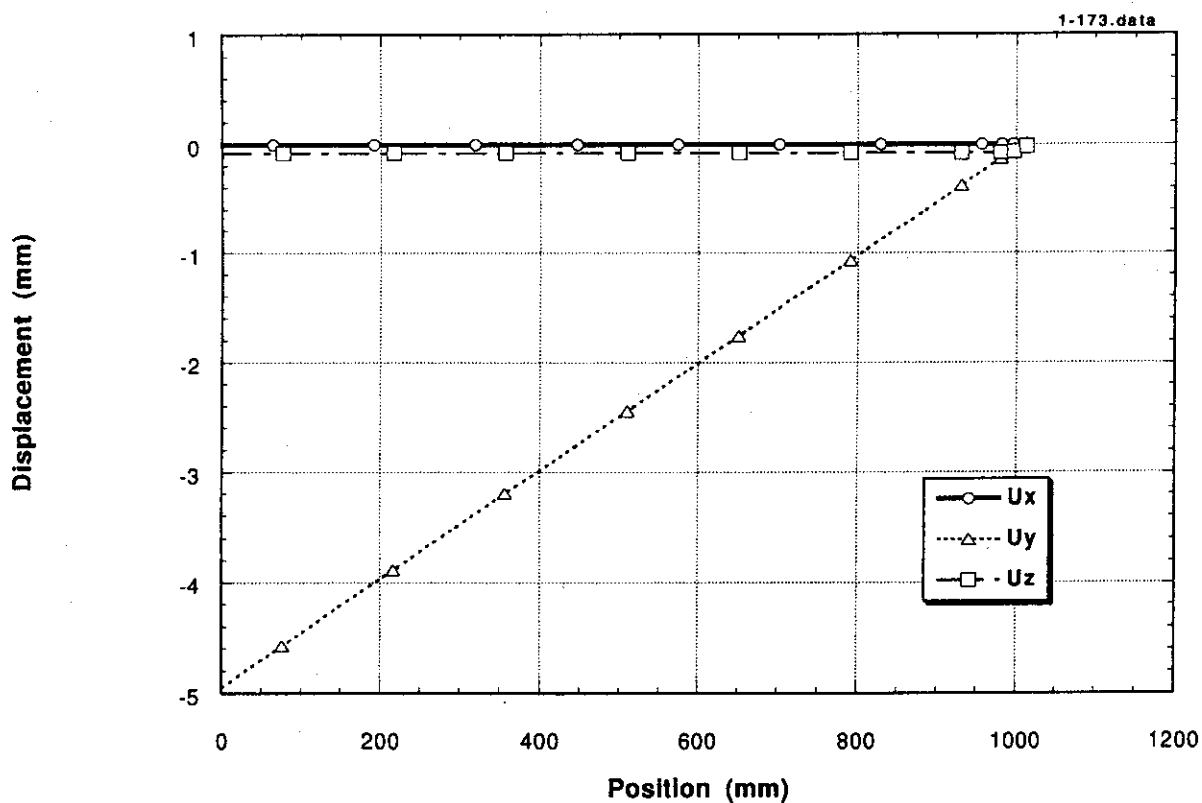
Fig. 41　Thermal deformation obtained in CASE 5
(upper part of the cooling tube)

1-173.data
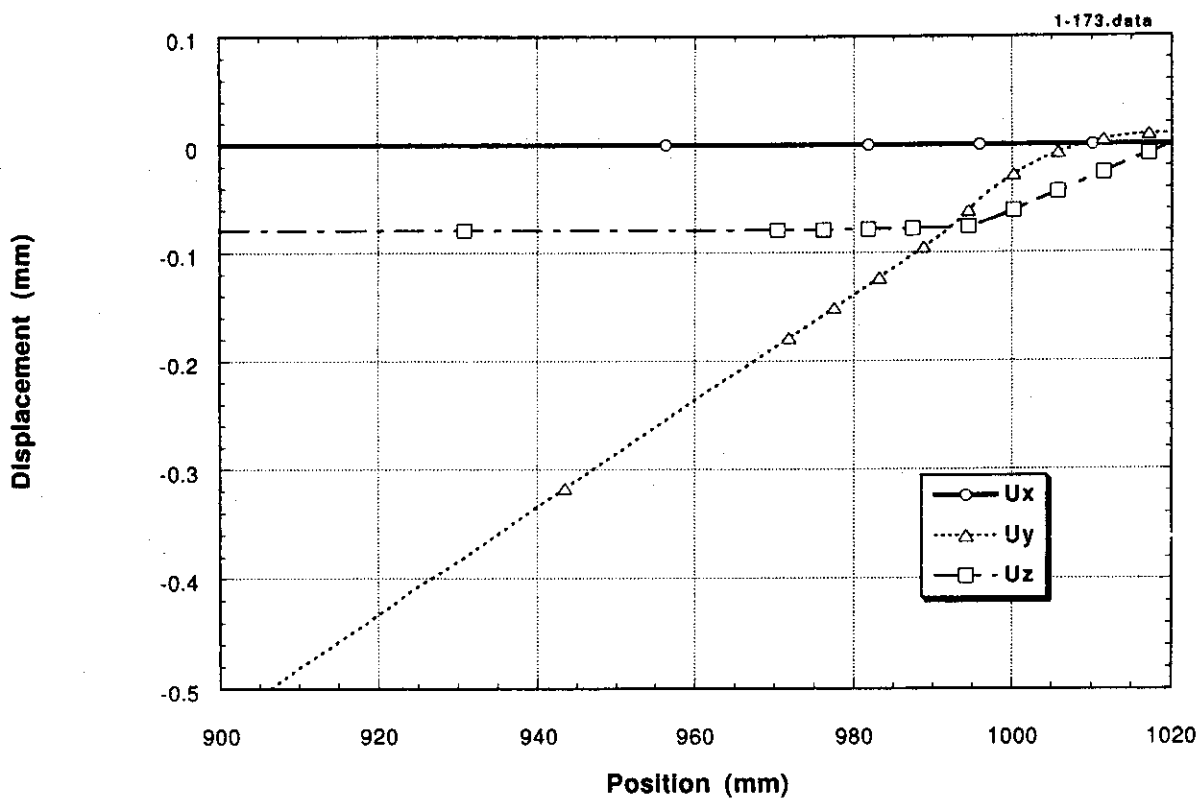
Fig. 42　Thermal deformation at selected points in CASE 5
(upper part of the cooling tube)
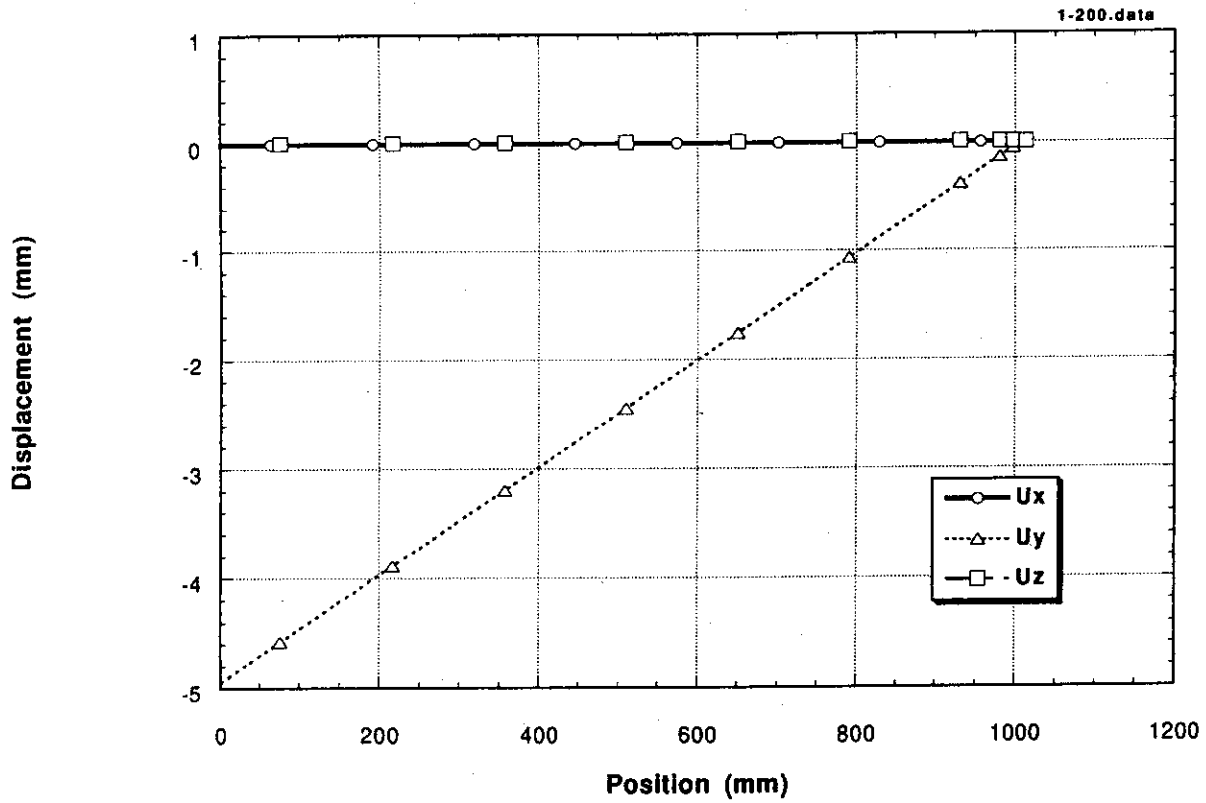
Fig. 43   Thermal deformation obtained in CASE 5
(lower part of the cooling tube)
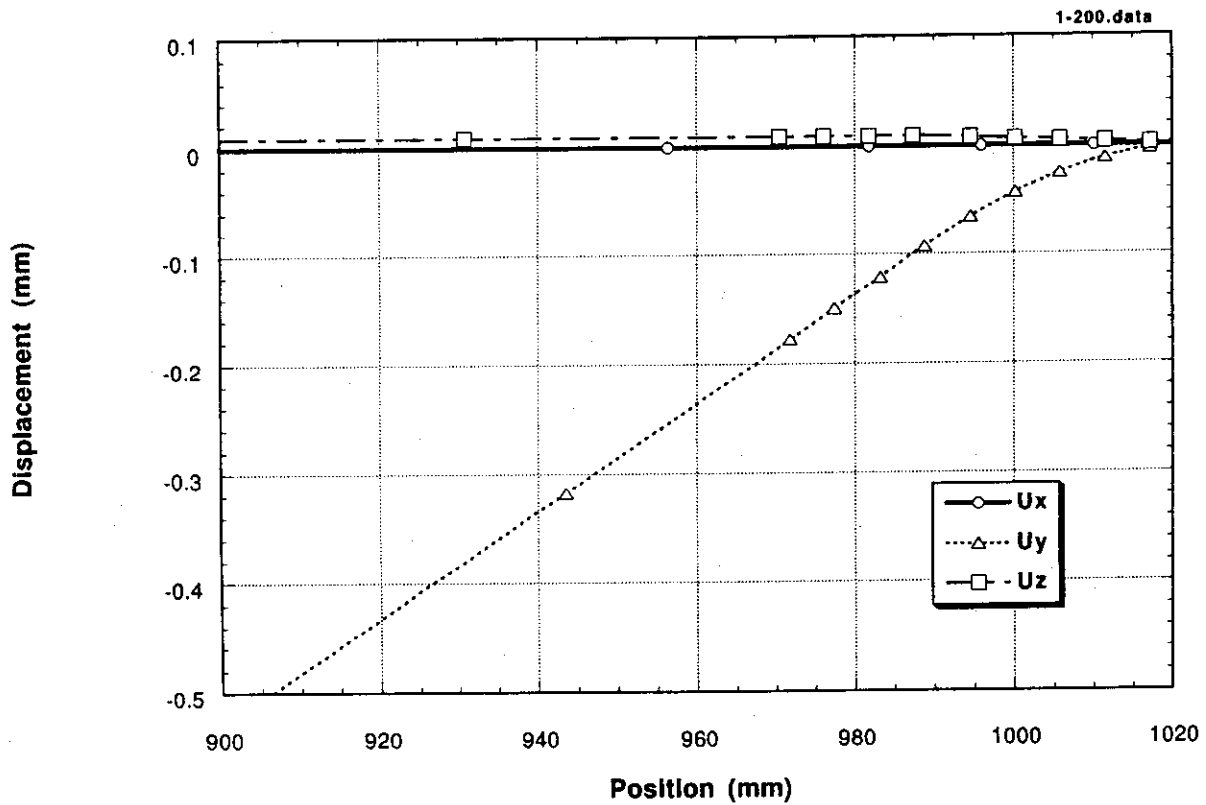
Fig. 44   Thermal deformation at selected points in CASE 5
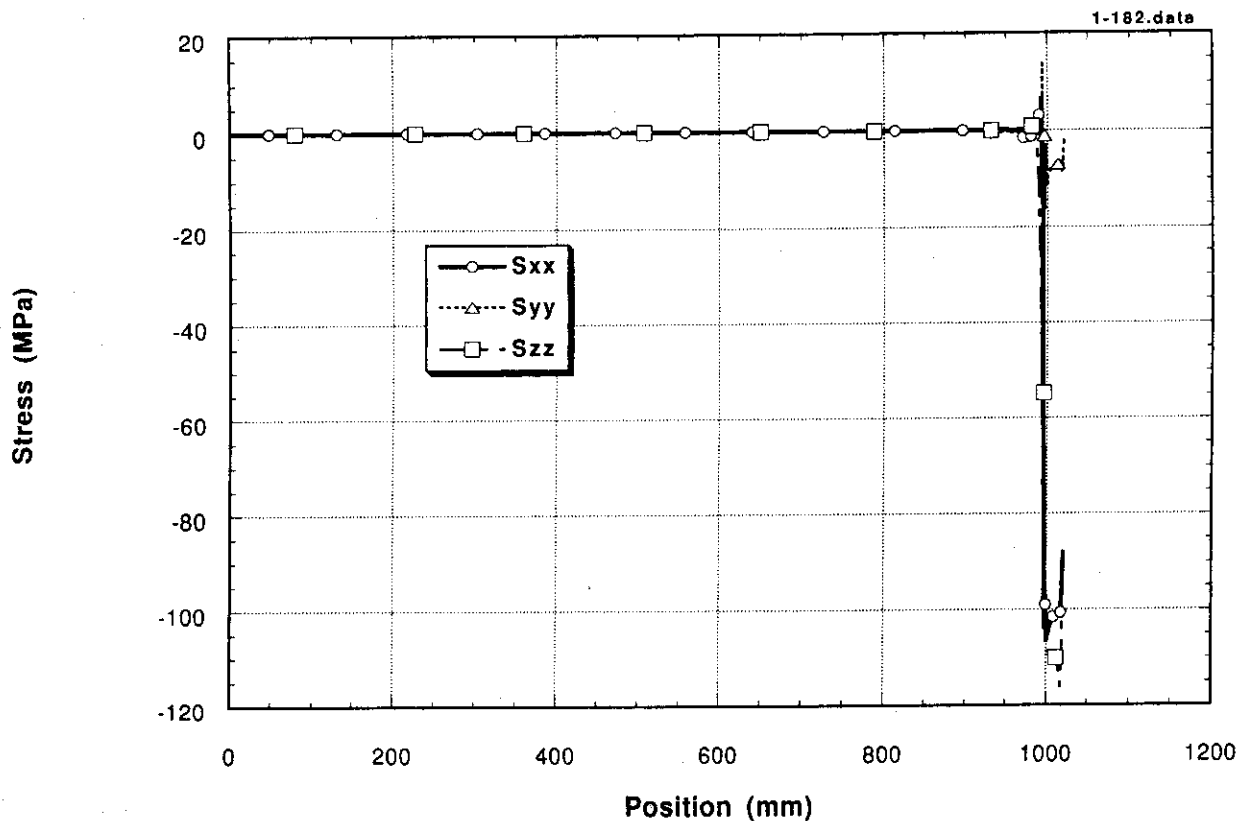(lower part of the cooling tube)

1-62.data
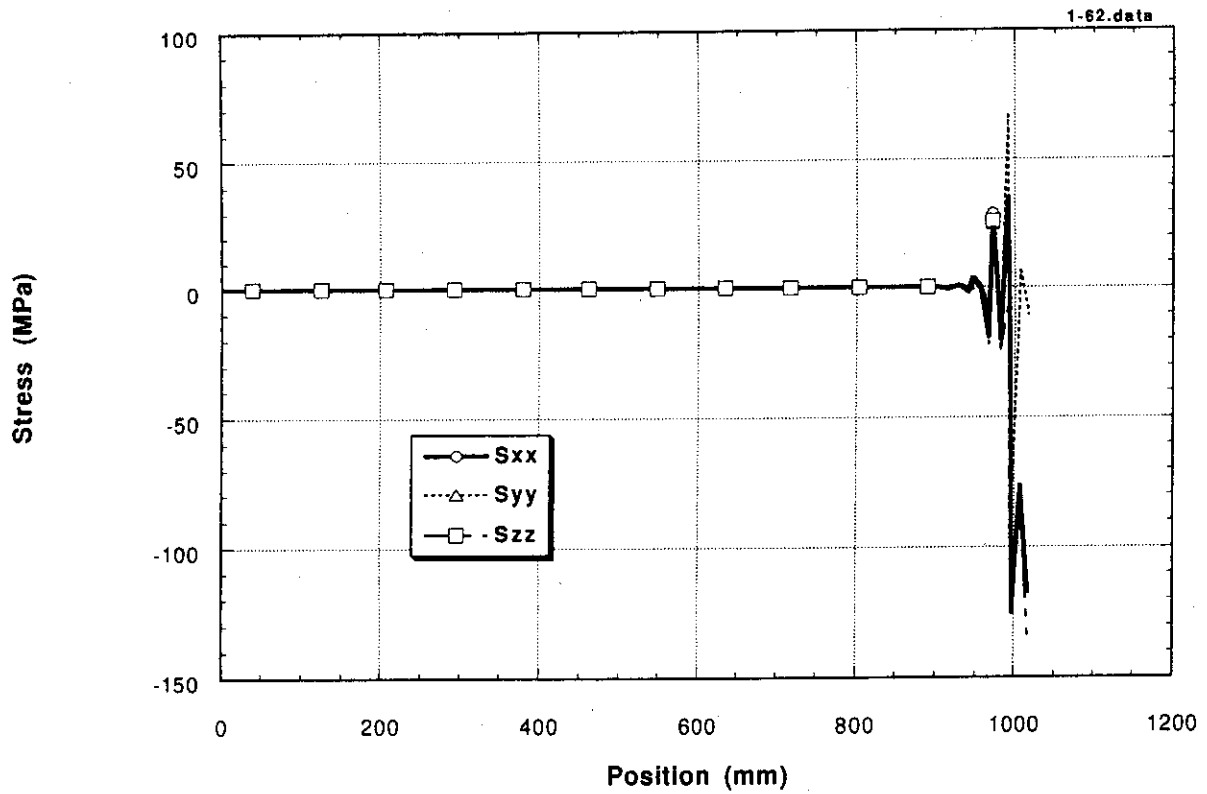
Fig. 45   Stress components obtained in CASE 1
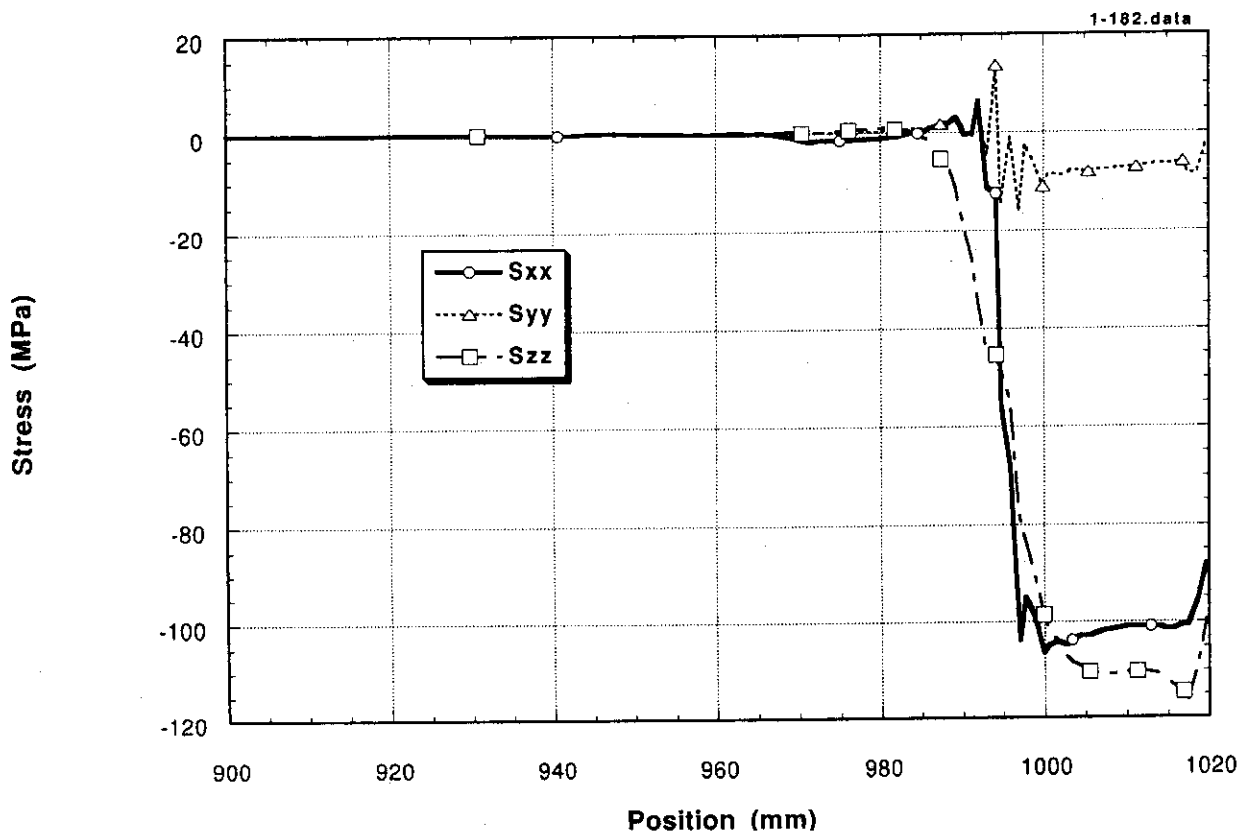(upper part of the cooling tube)

1-62.data
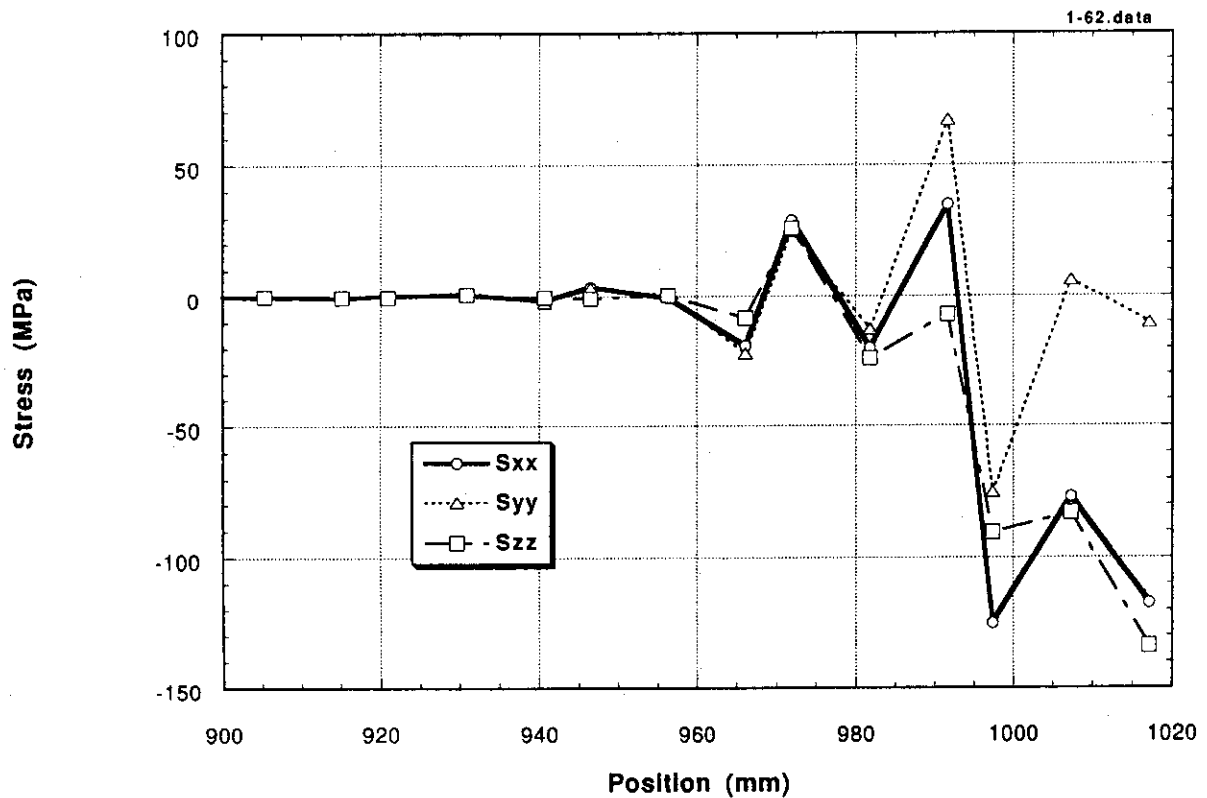
Fig. 46   Stress components at selected elements in CASE 1
(upper part of the cooling tube)

1-77.data
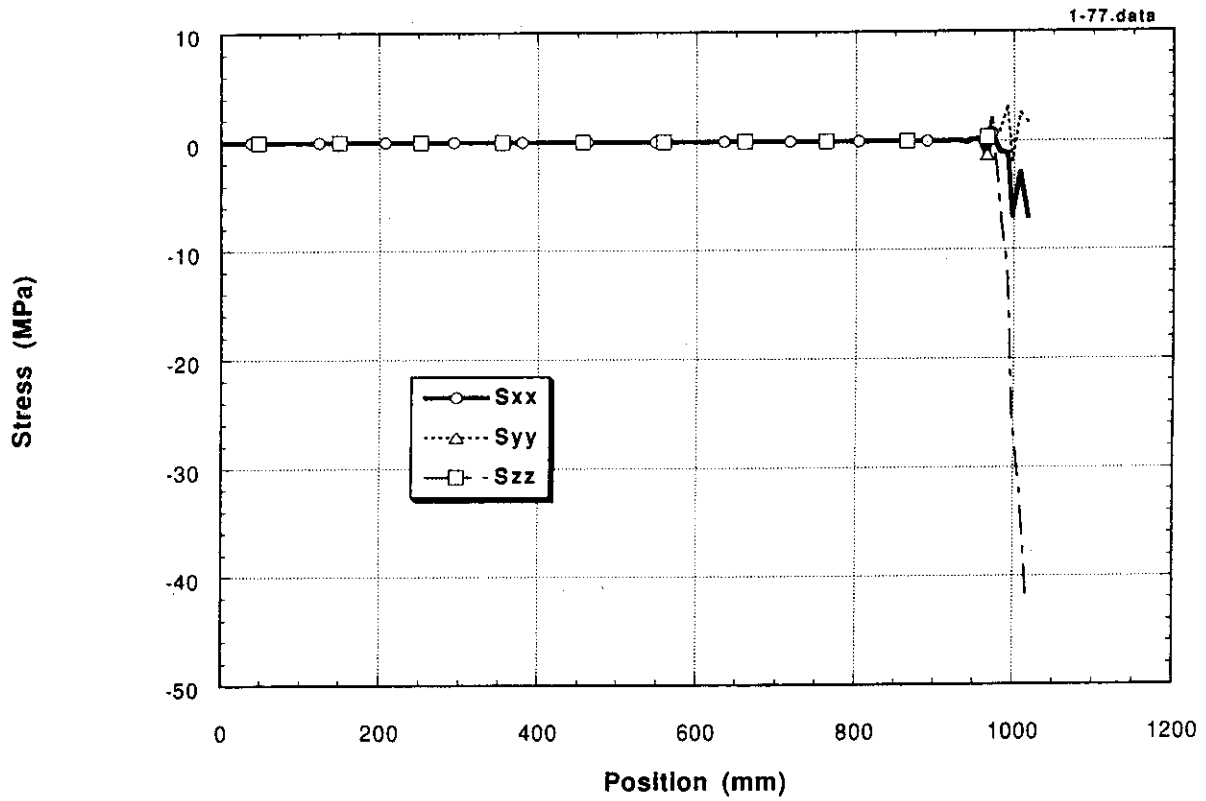
Fig. 47   Stress components obtained in CASE 1
(lower part of the cooling tube)

1-77.data
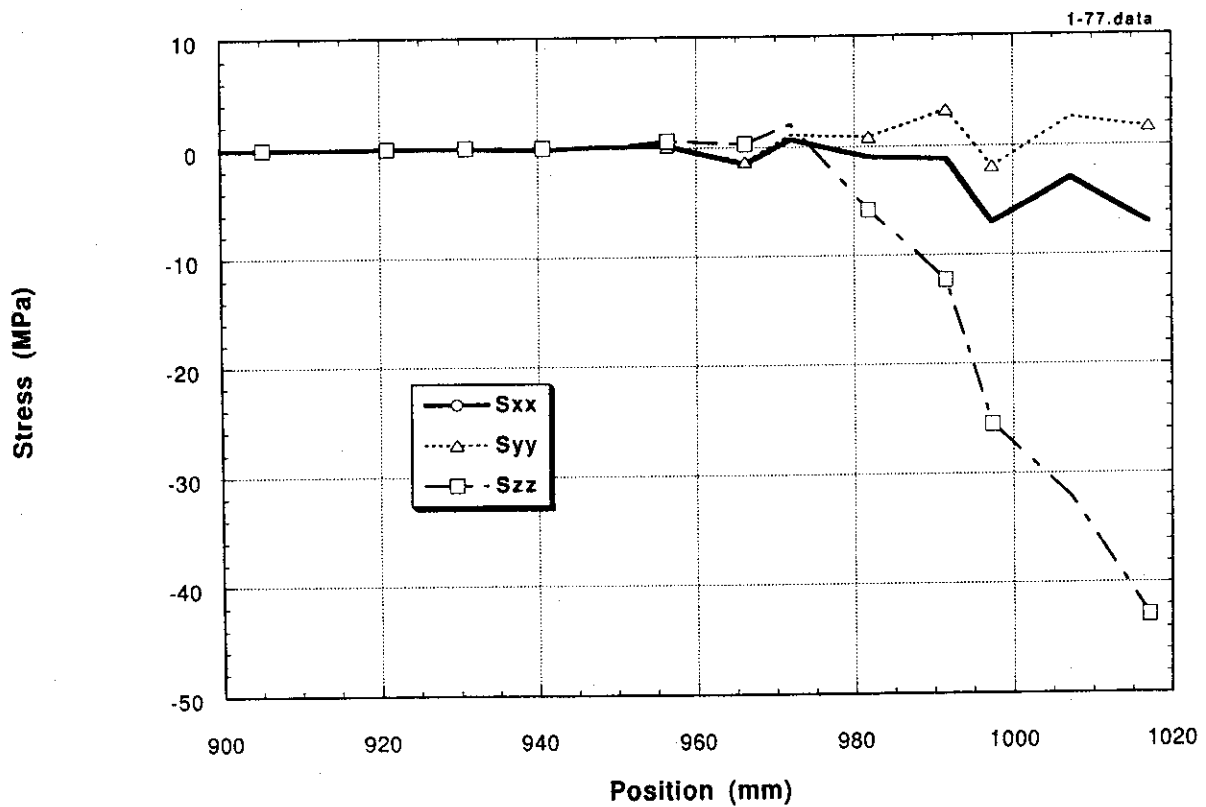
Fig. 48   Stress components at selected elements in CASE 1
(lower part of the cooling tube)
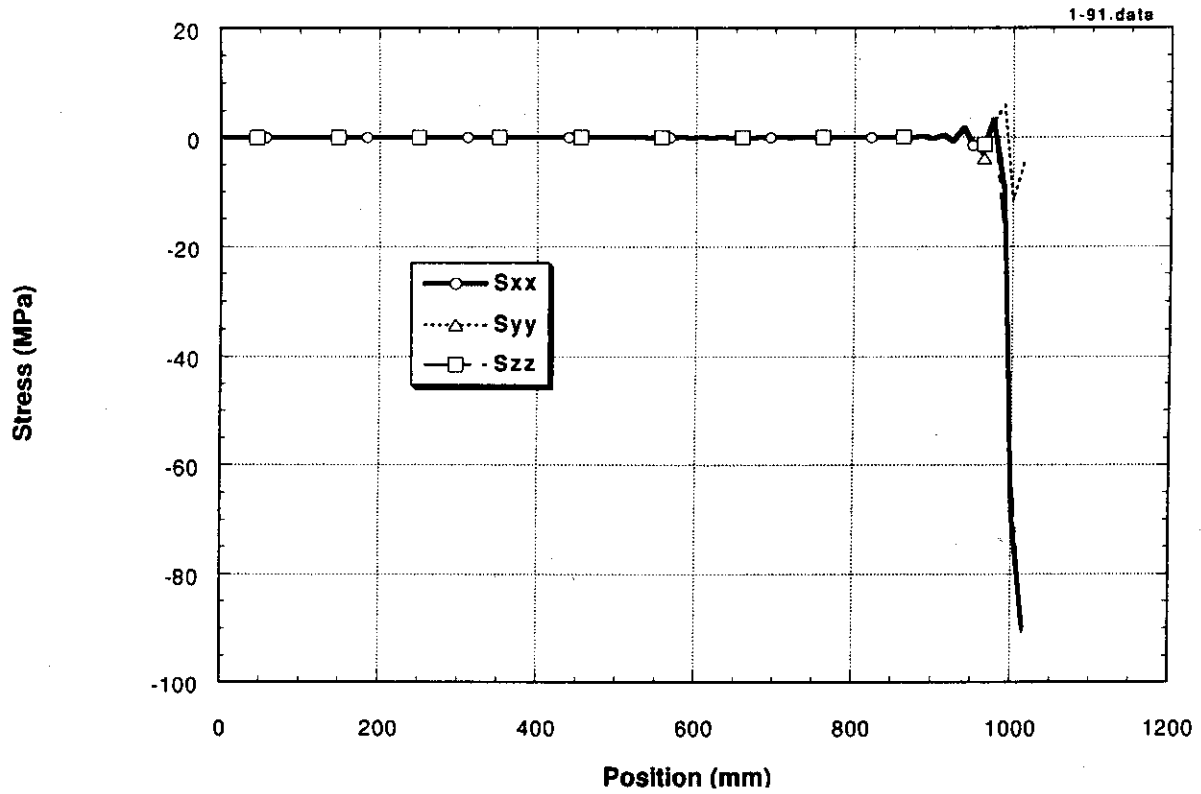
Fig. 49 Stress components obtained in CASE 2
(upper part of the cooling tube)
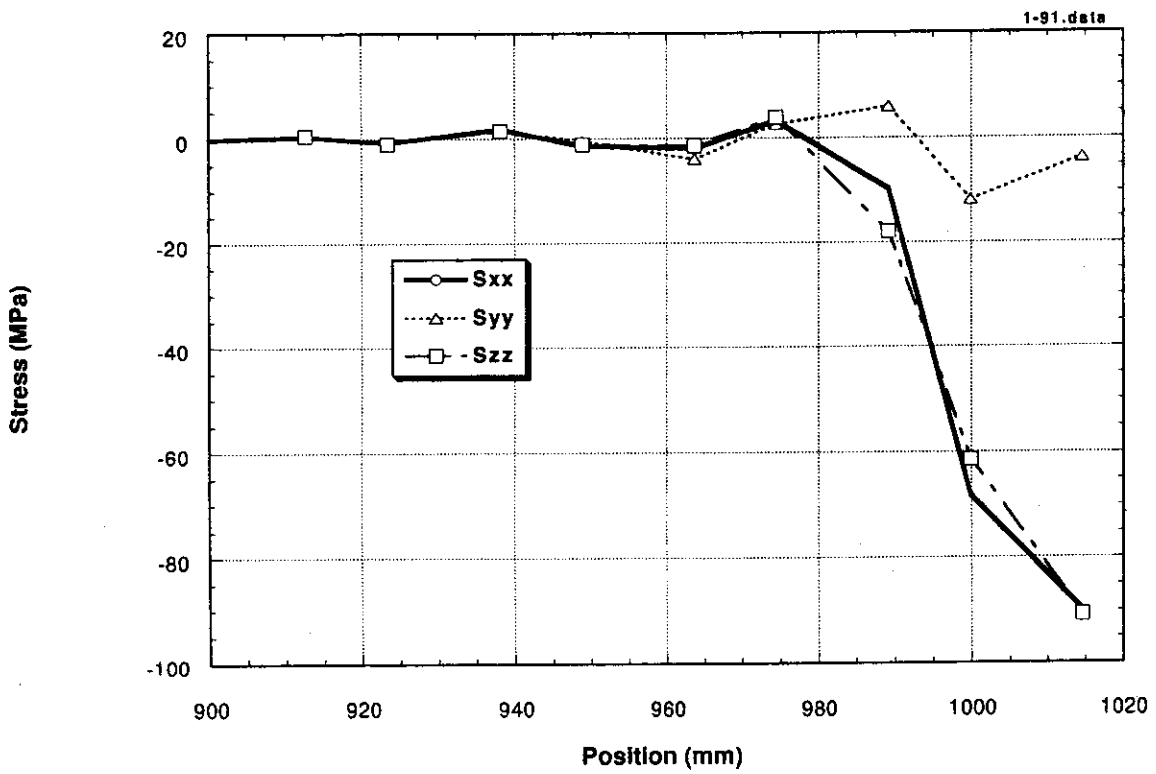
Fig. 50 Stress components at selected elements in CASE 2
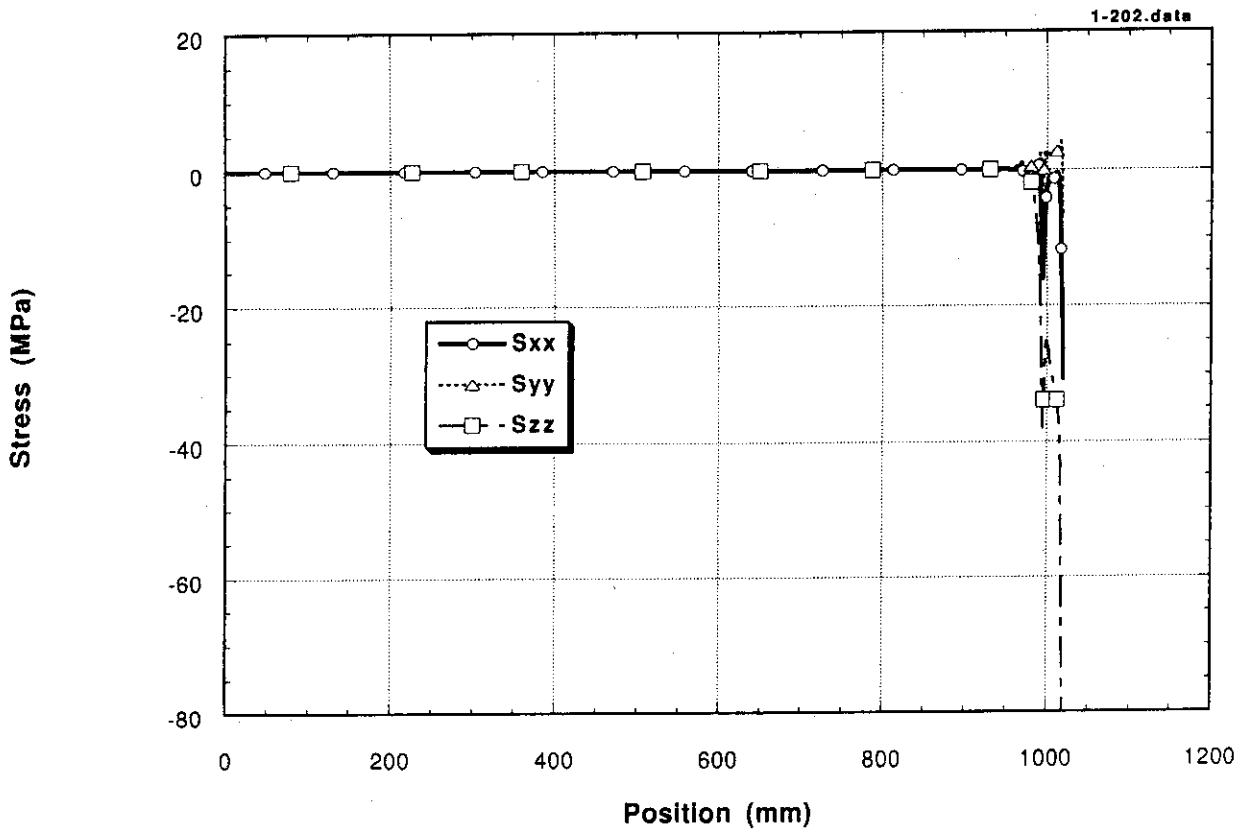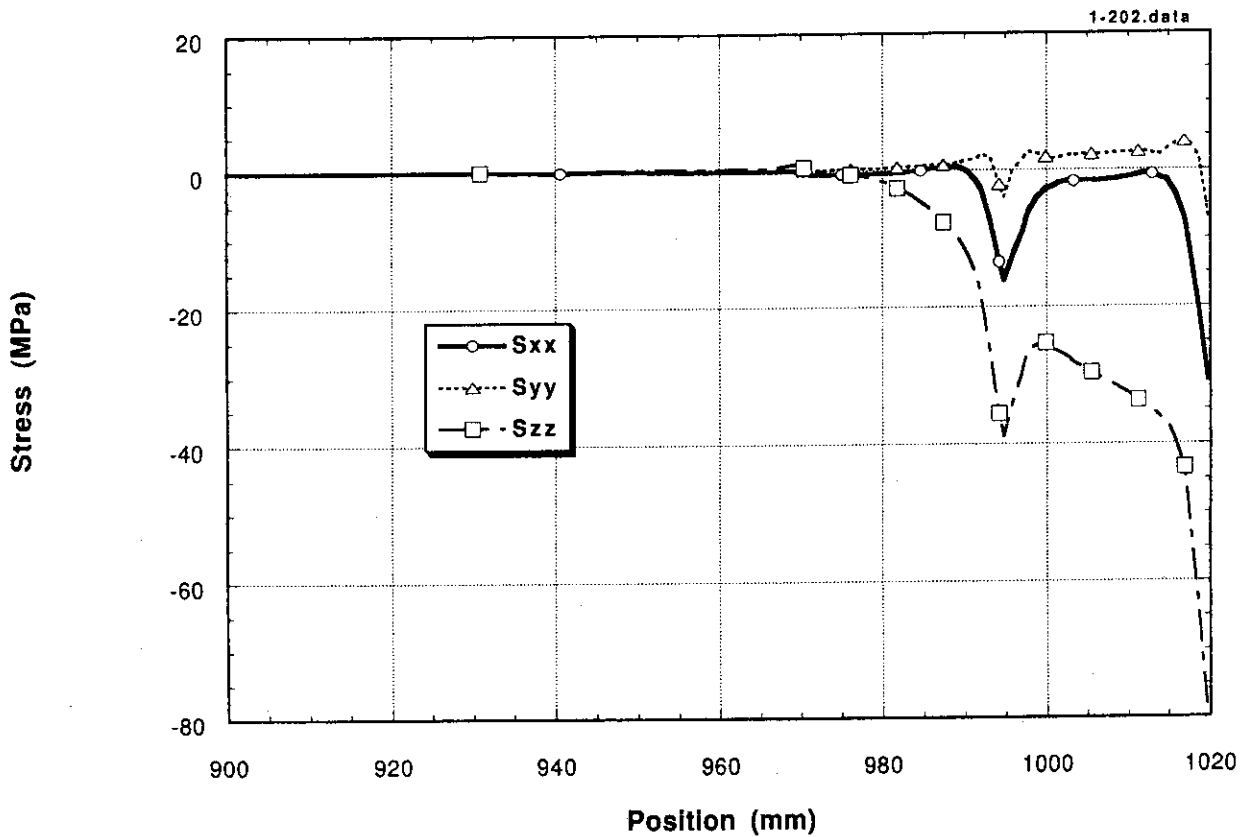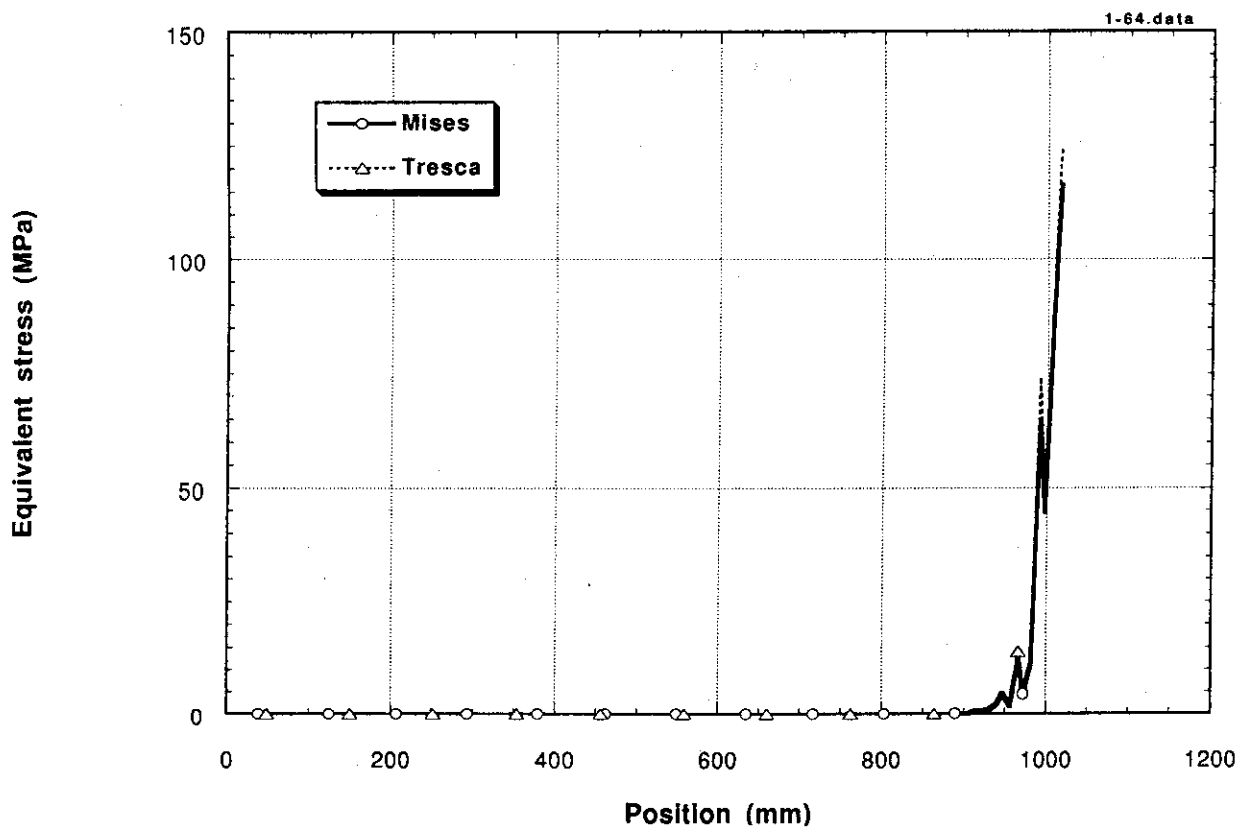(upper part of the cooling tube)

1-104.data

Fig. 51　Stress components obtained in CASE 2
(lower part of the cooling tube)

1-104.data
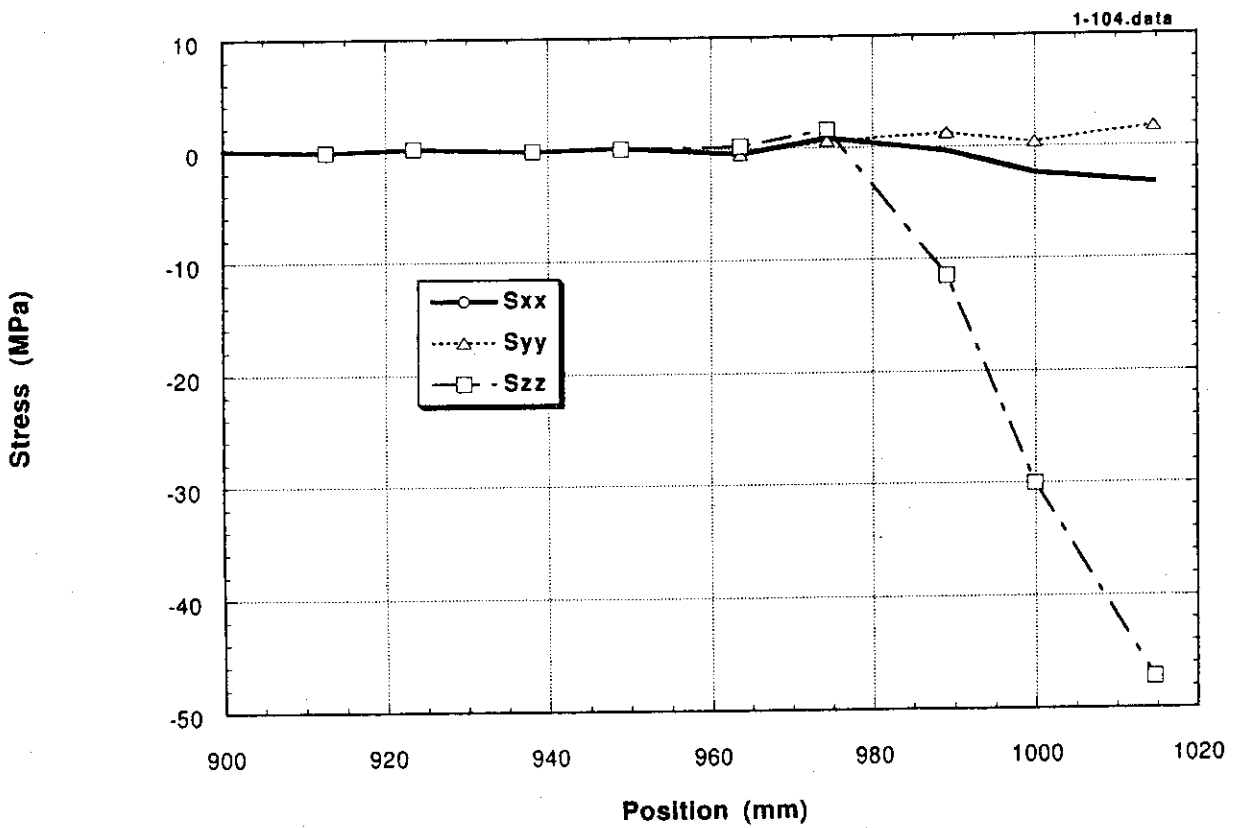
Fig. 52　Stress components at selected elements in CASE 2
(lower part of the cooling tube)
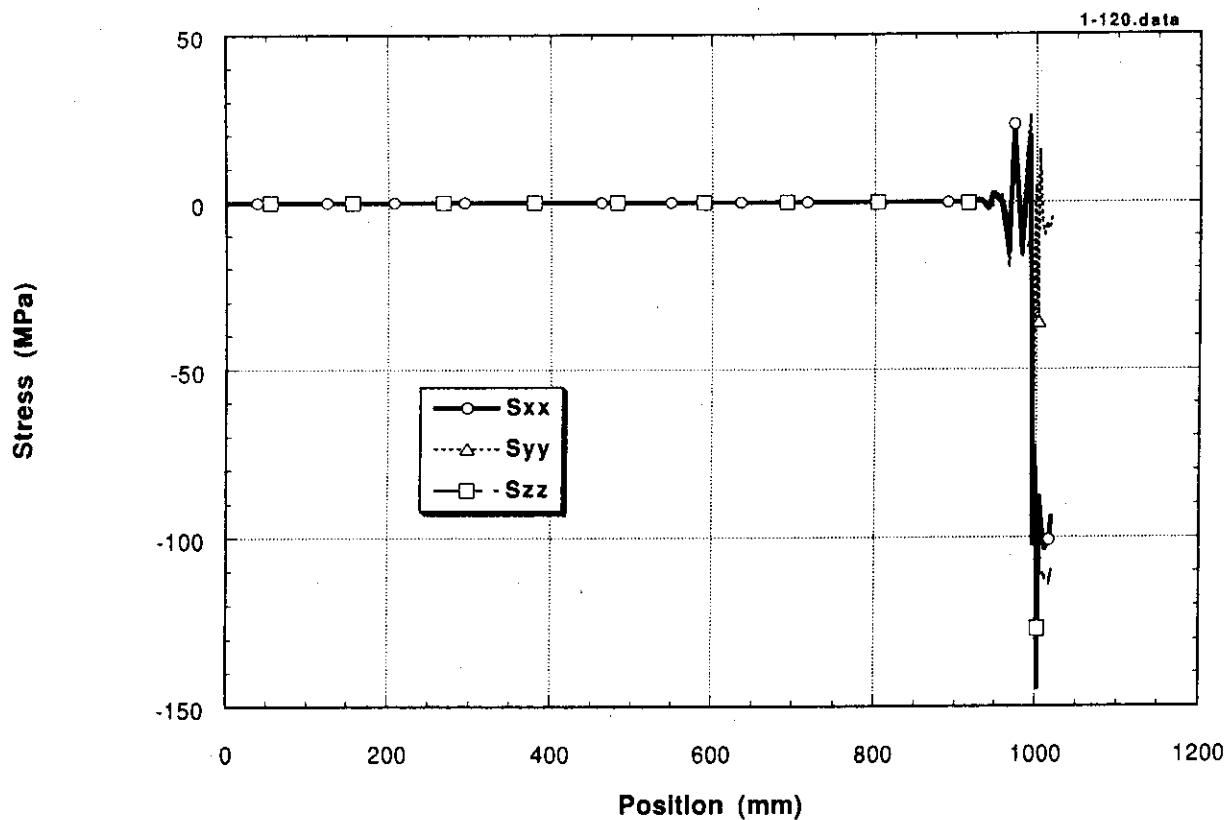
Fig. 53   Stress components obtained in CASE 3
(upper part of the cooling tube)
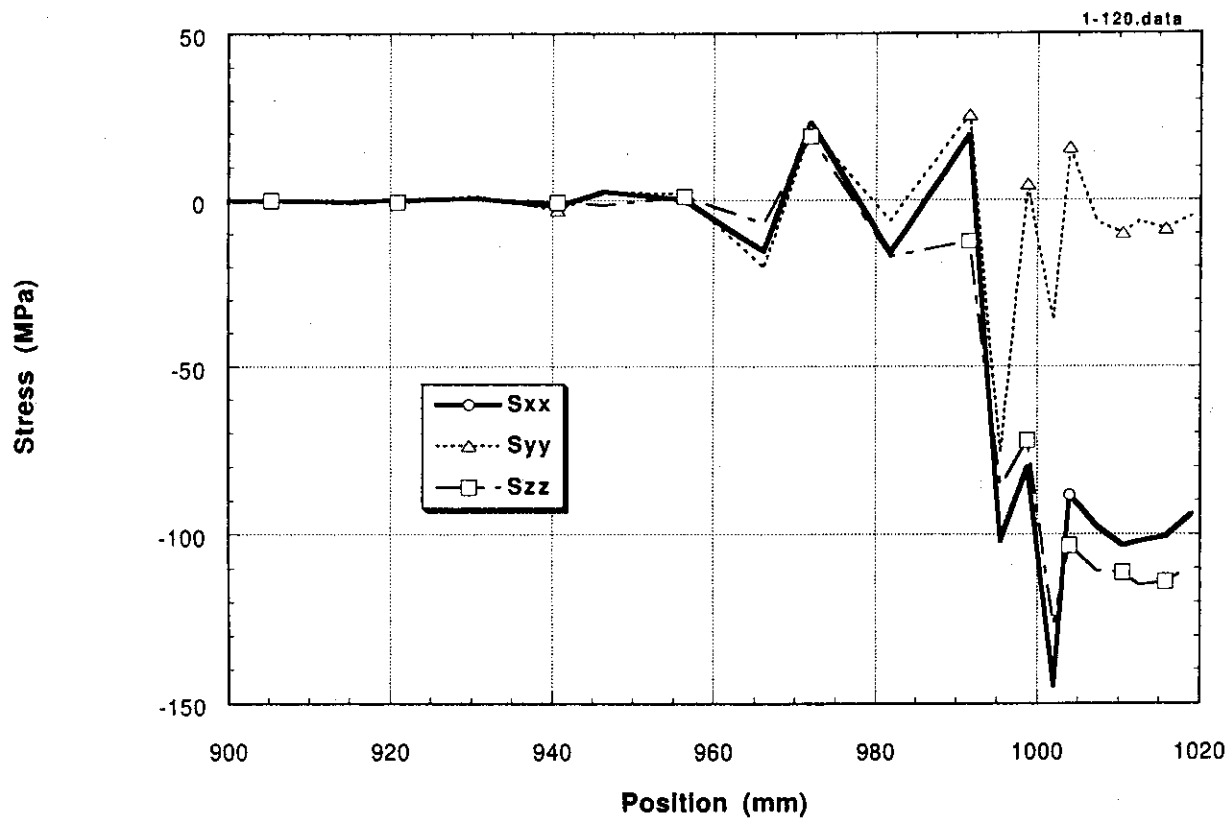
Fig. 54   Stress components at selected elements in CASE 3
(upper part of the cooling tube)

Fig. 55   Stress components obtained in CASE 3
(lower part of the cooling tube)
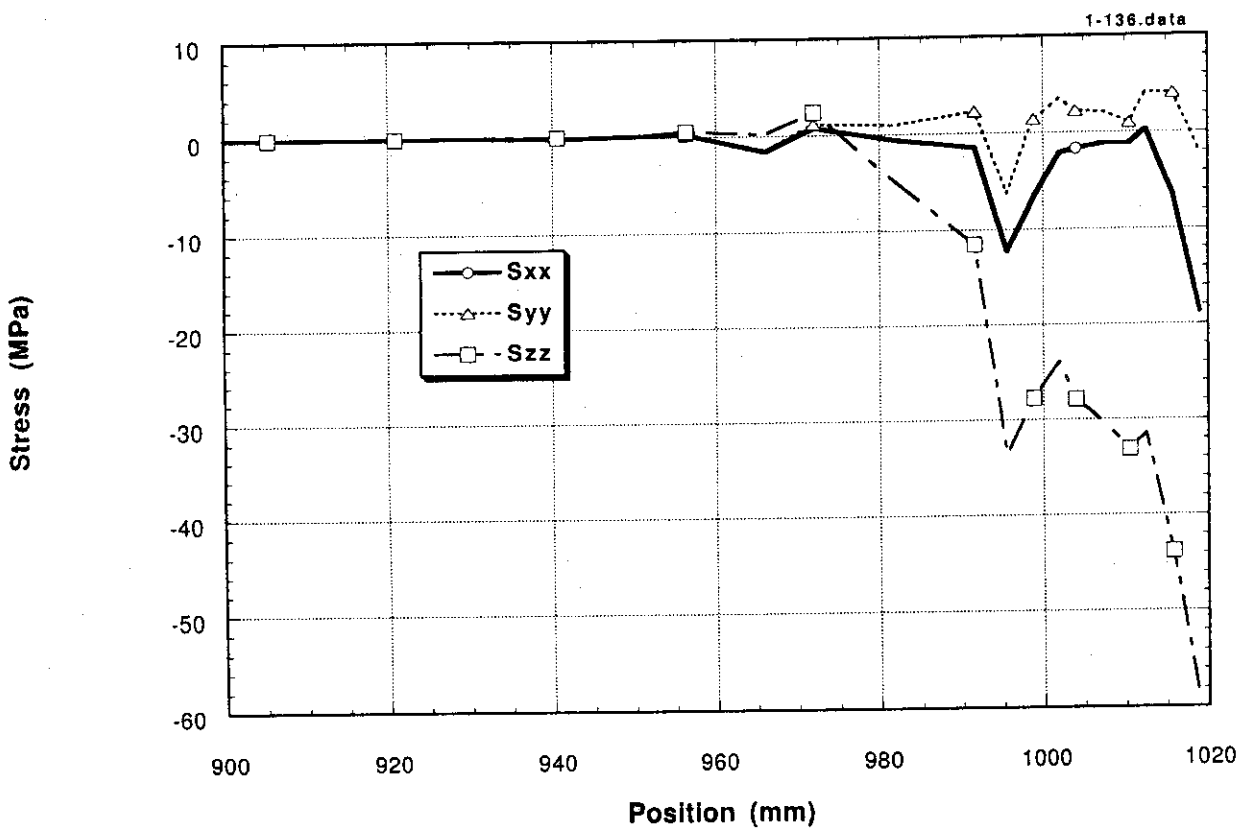
Fig. 56   Stress components at selected elements in CASE 3
(lower part of the cooling tube)

1-150.data

Stress (MPa)

Fig. 57 Stress components obtained in CASE 4
(upper part of the cooling tube)

1-150.data

Stress (MPa)

Position (mm)
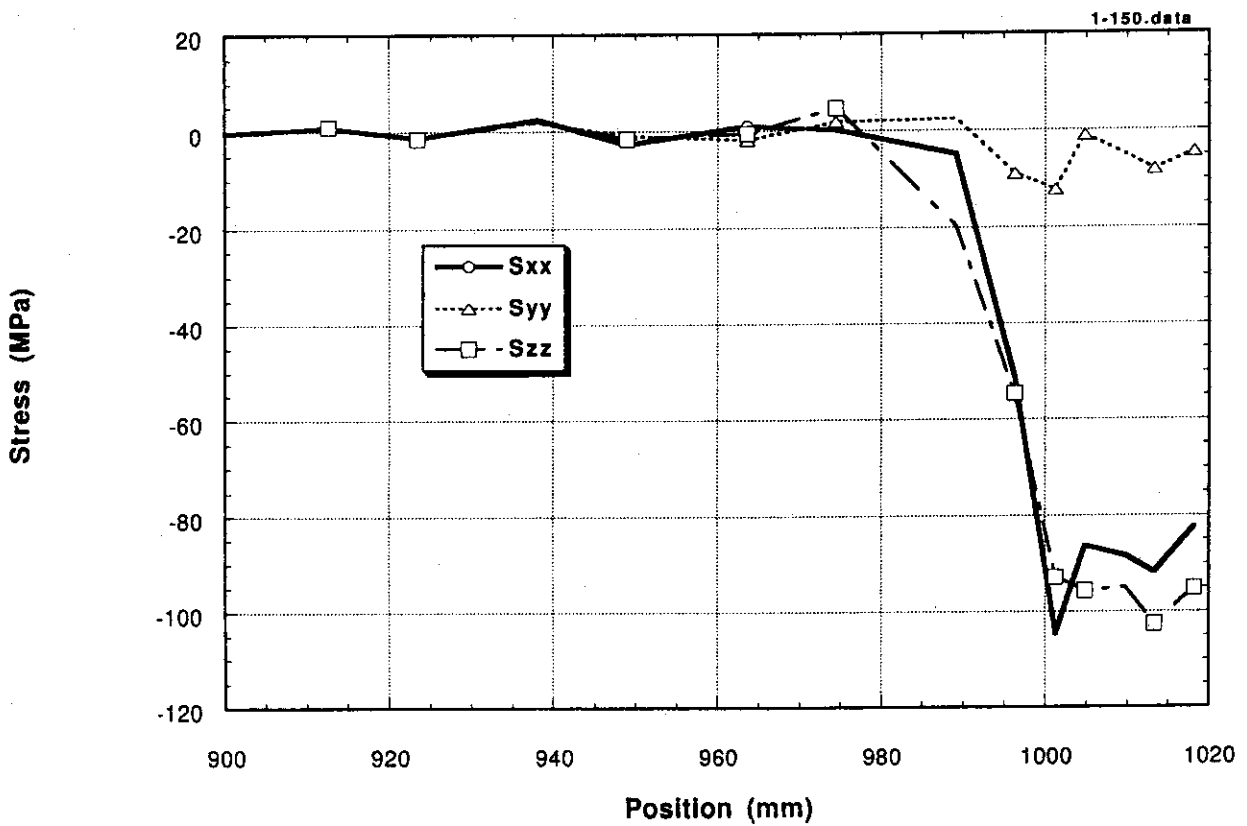
Fig. 58 Stress components at selected elements in CASE 4
(upper part of the cooling tube)

1-164.data

Fig. 59 Stress components obtained in CASE 4
(lower part of the cooling tube)

1-164.data
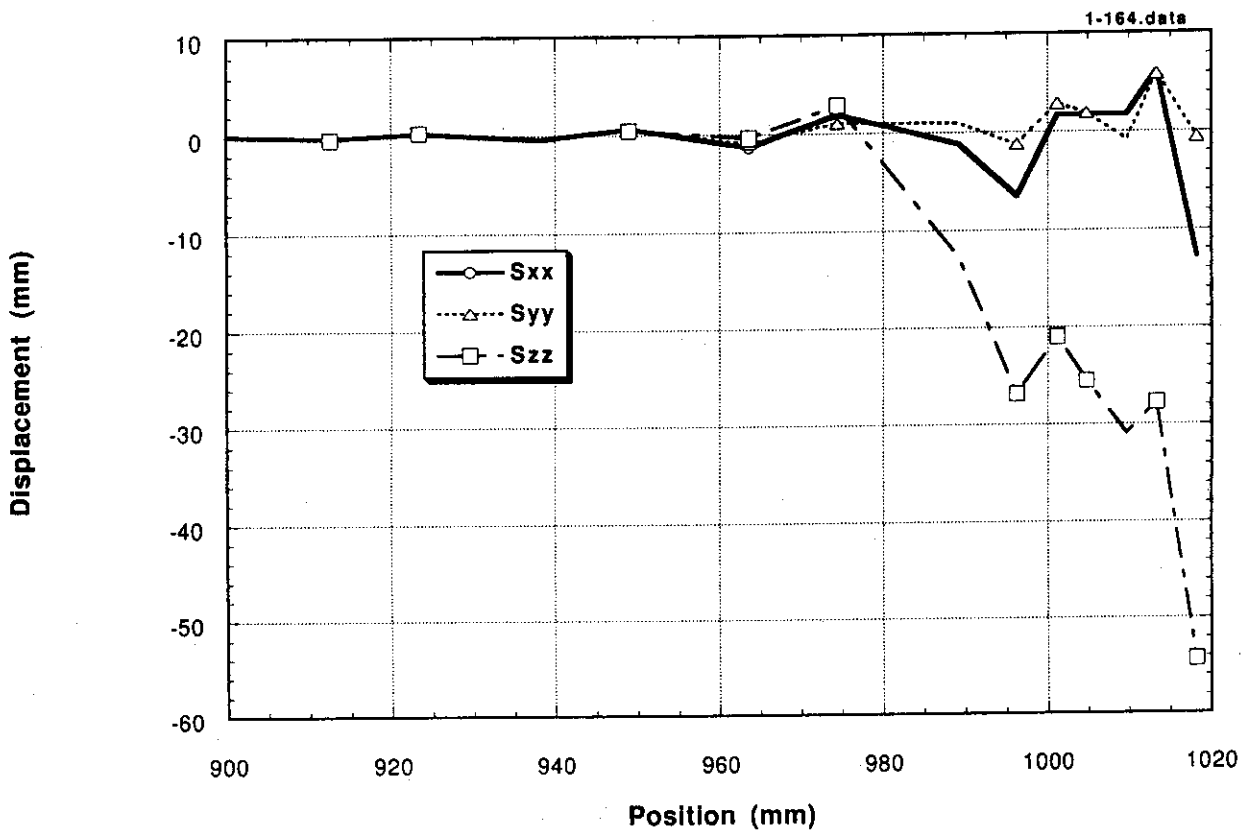
Fig. 60 Stress components at selected elements in CASE 4
(lower part of the cooling tube)

1-182.data

Fig. 61 Stress components obtained in CASE 5
(upper part of the cooling tube)

1-182.data

Fig. 62 Stress components at selected elements in CASE 5
(upper part of the cooling tube)

1-202.data

Fig. 63   Stress components obtained in CASE 5
(lower part of the cooling tube)

1-202.data

Fig. 64   Stress components at selected elements in CASE 5
(lower part of the cooling tube)

1-64.data

Fig. 65   Mises and Tresca equivalent stress distributions obtained in CASE 1
(upper part of the cooling tube)

1-64.data
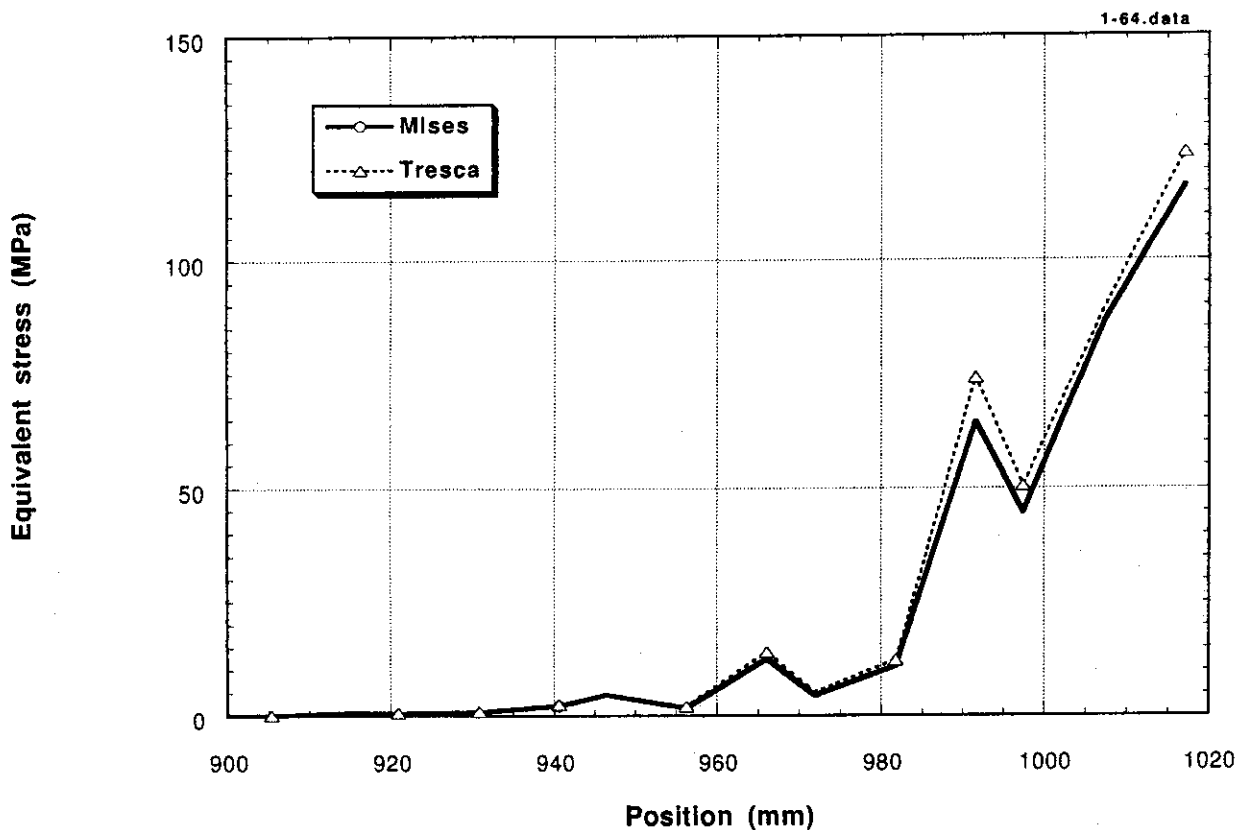
Fig. 66   Mises and Tresca equivalent stress distributions at selected elements in CASE 1
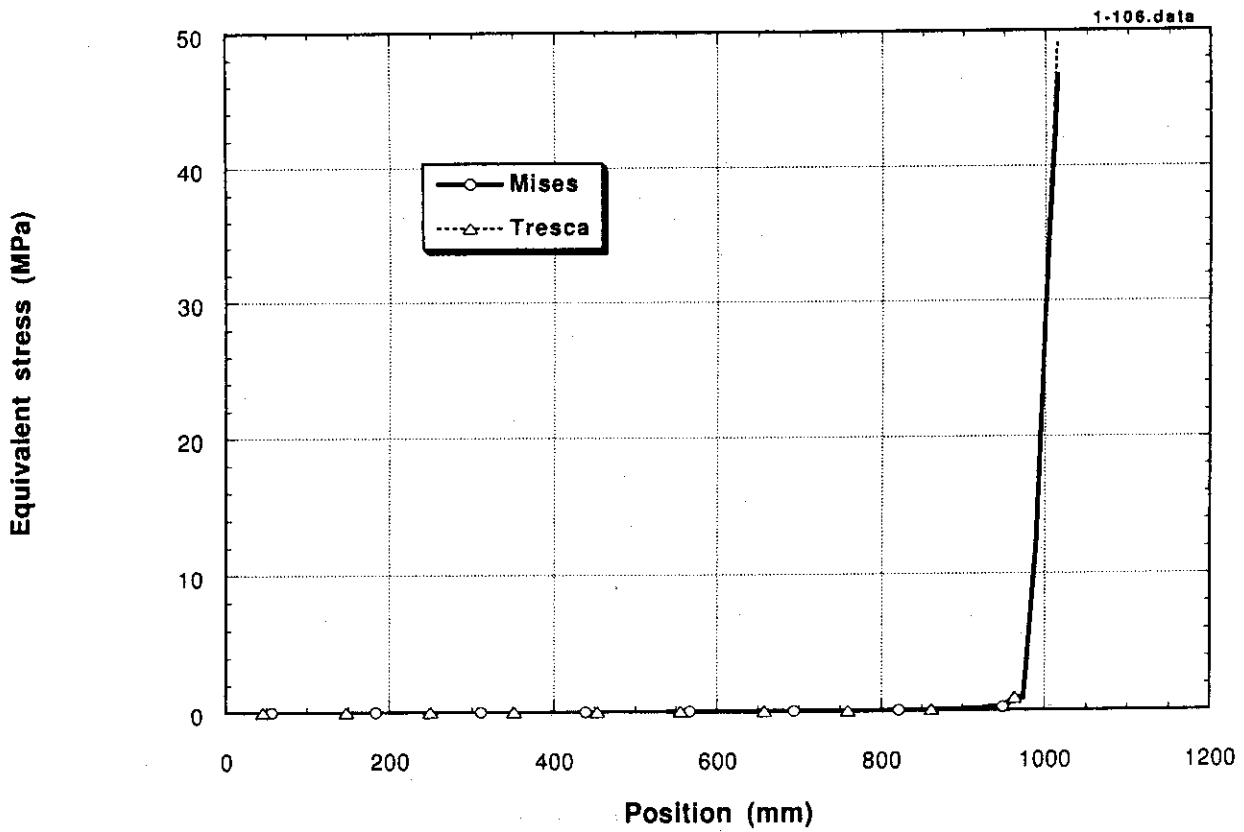(upper part of the cooling tube)
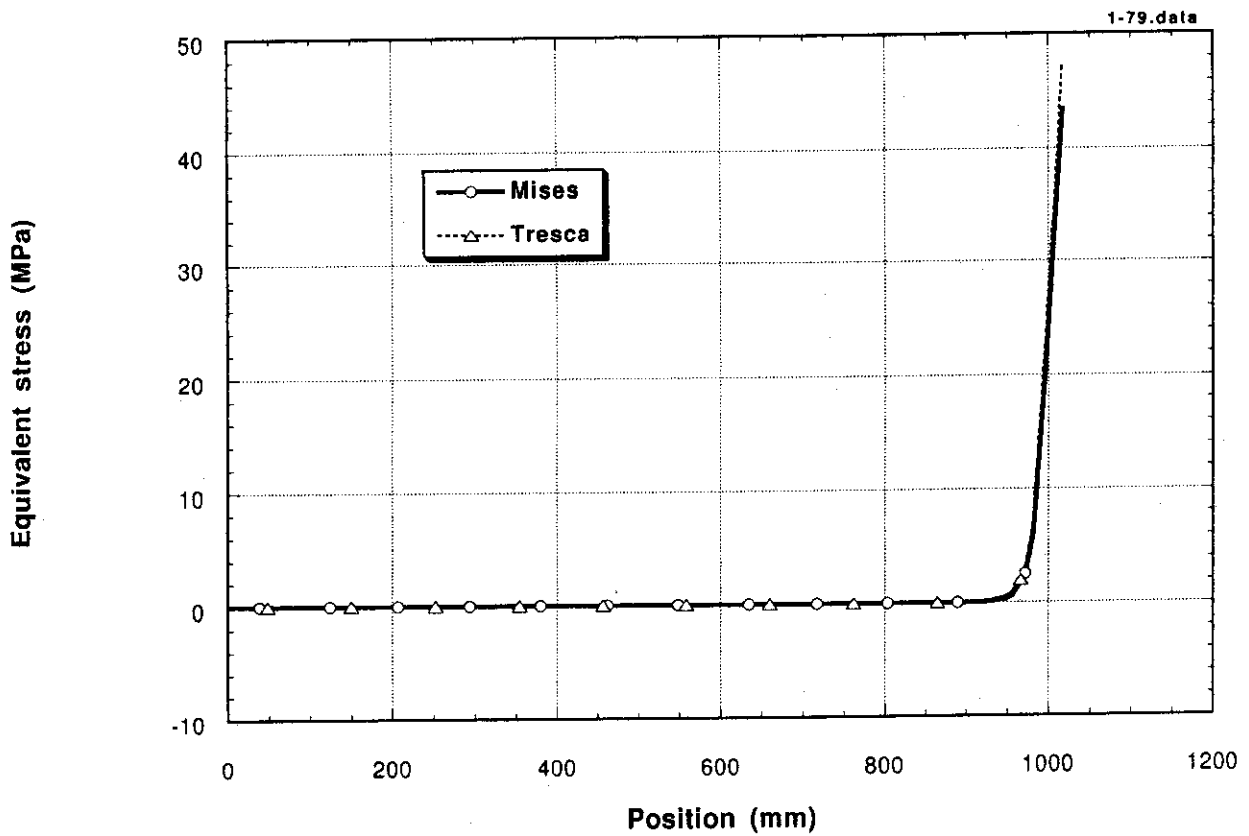
Fig. 67 Mises and Tresca equivalent stress distributions obtained in CASE 1
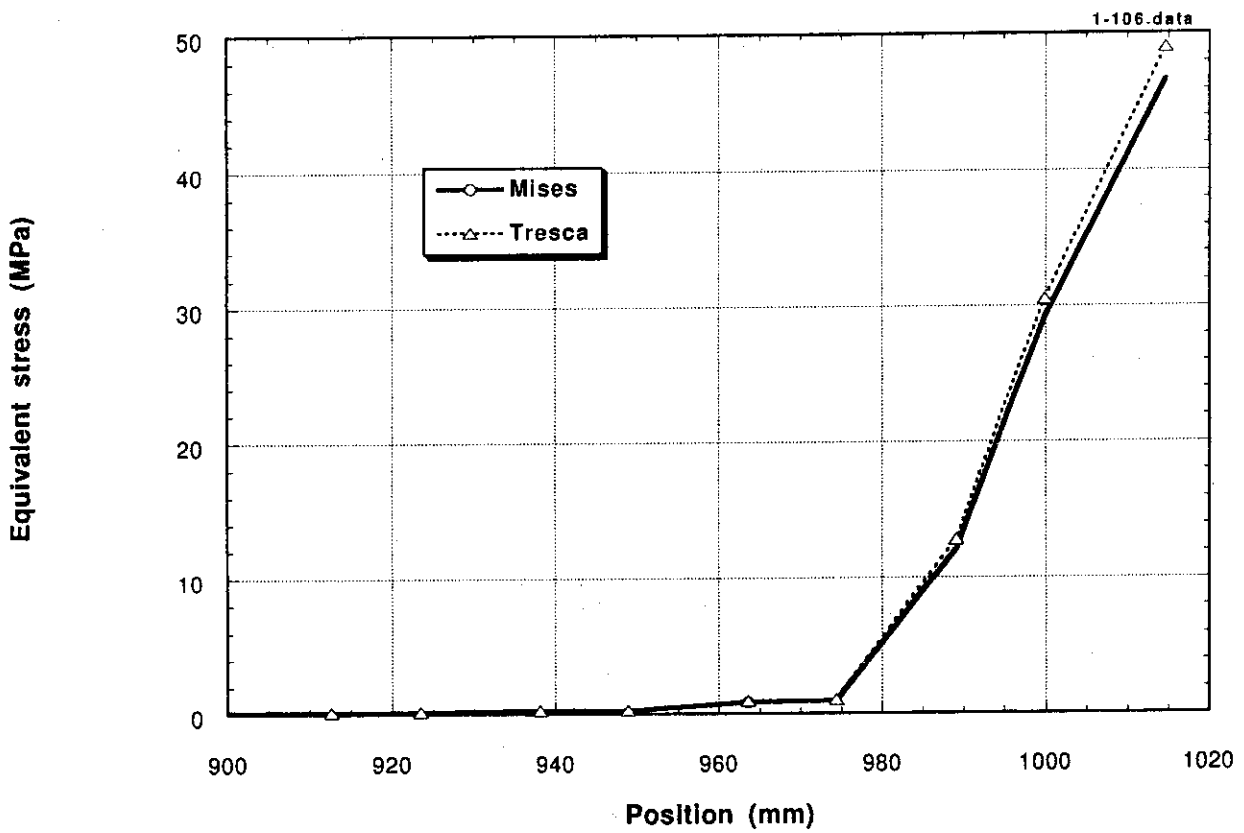(lower part of the cooling tube)
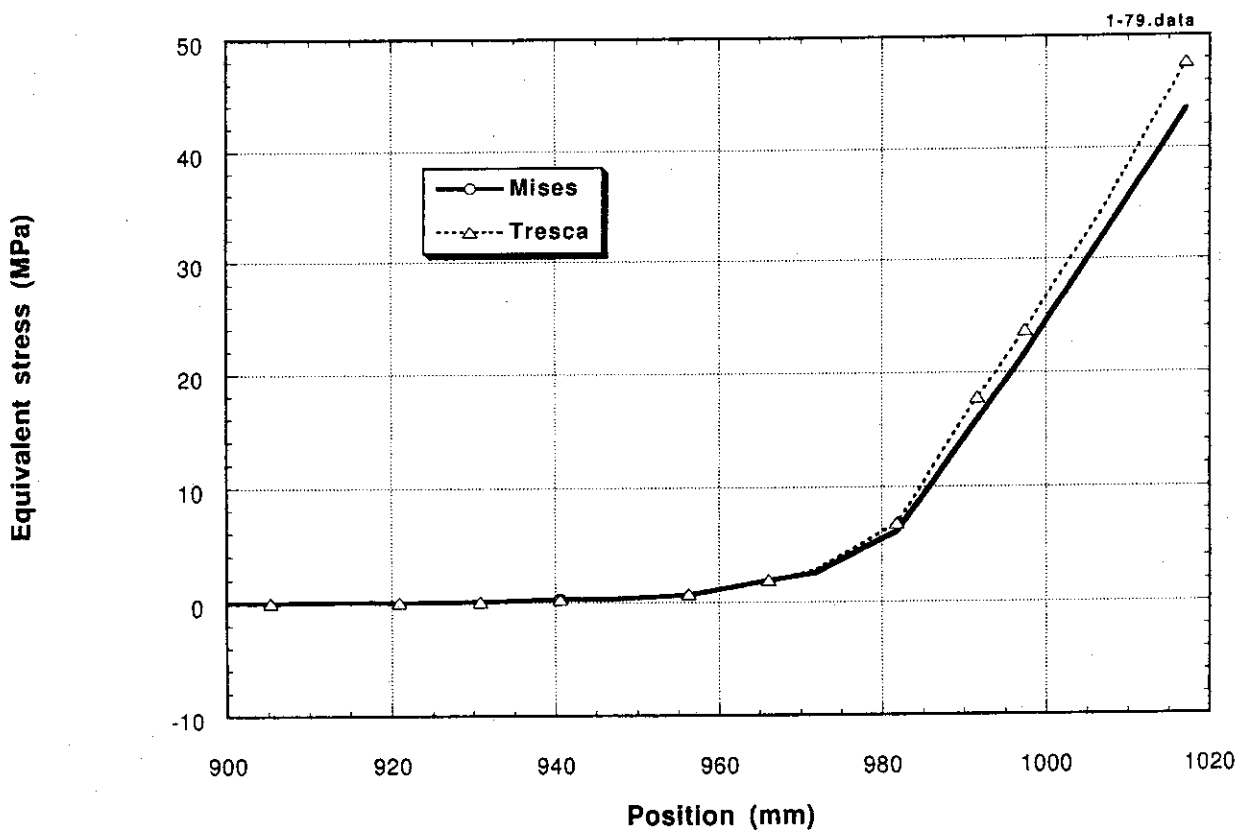
Fig. 68 Mises and Tresca equivalent stress distributions at selected elements in CASE 1
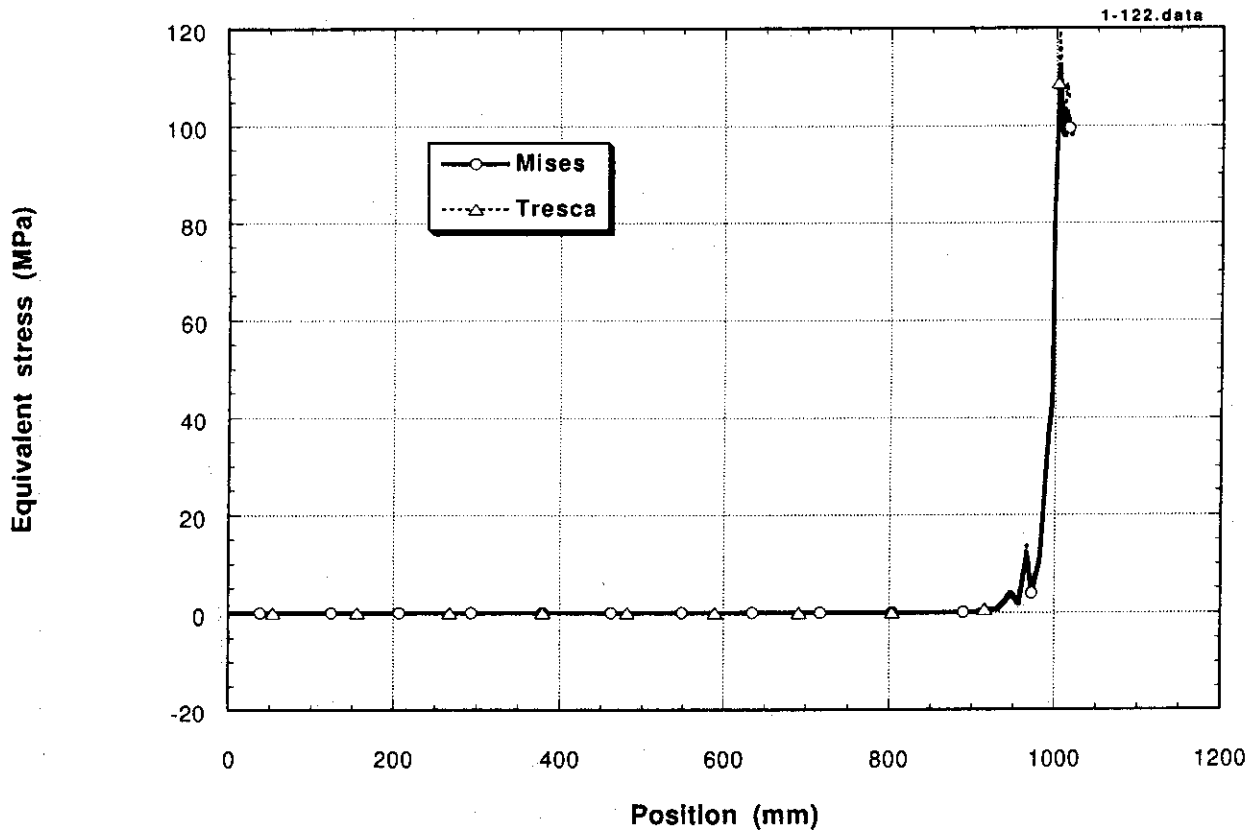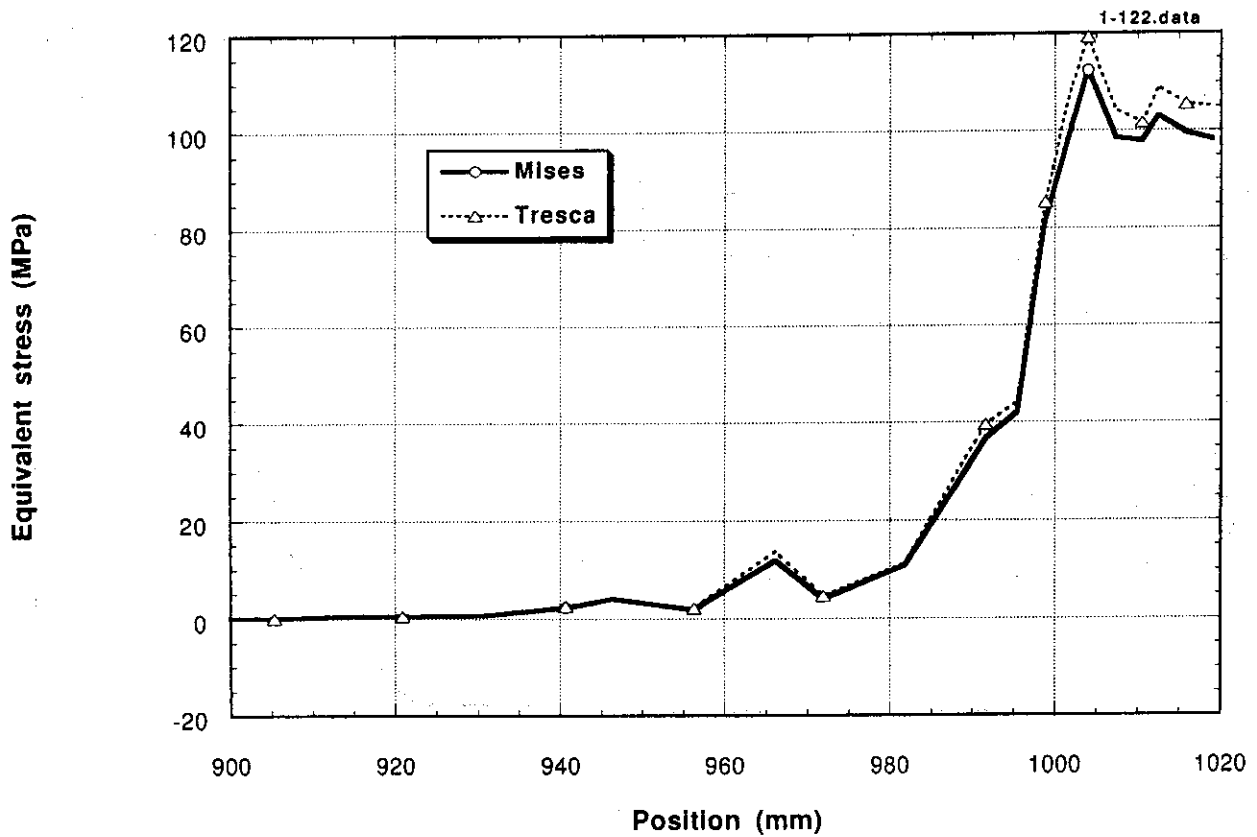(lower part of the cooling tube)
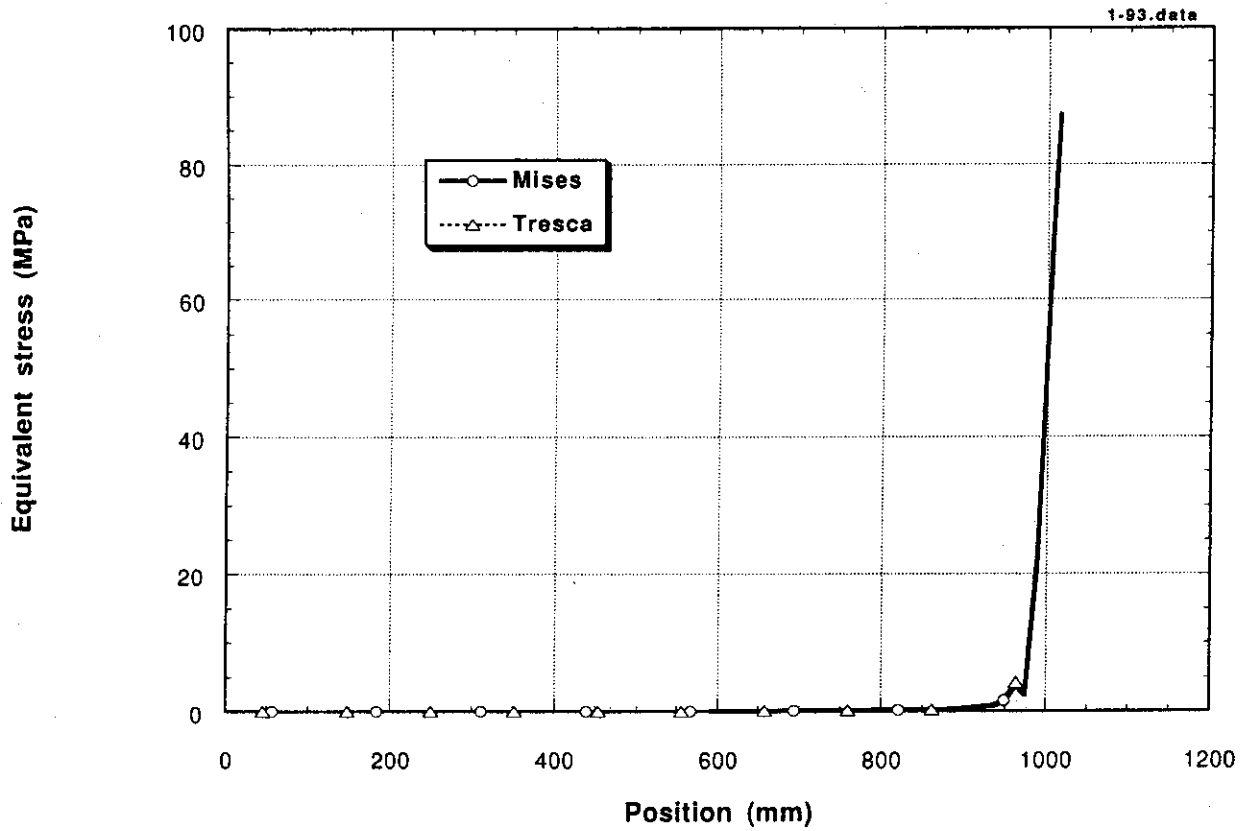
Fig. 69   Mises and Tresca equivalent stress distributions obtained in CASE 2
(upper part of the cooling tube)
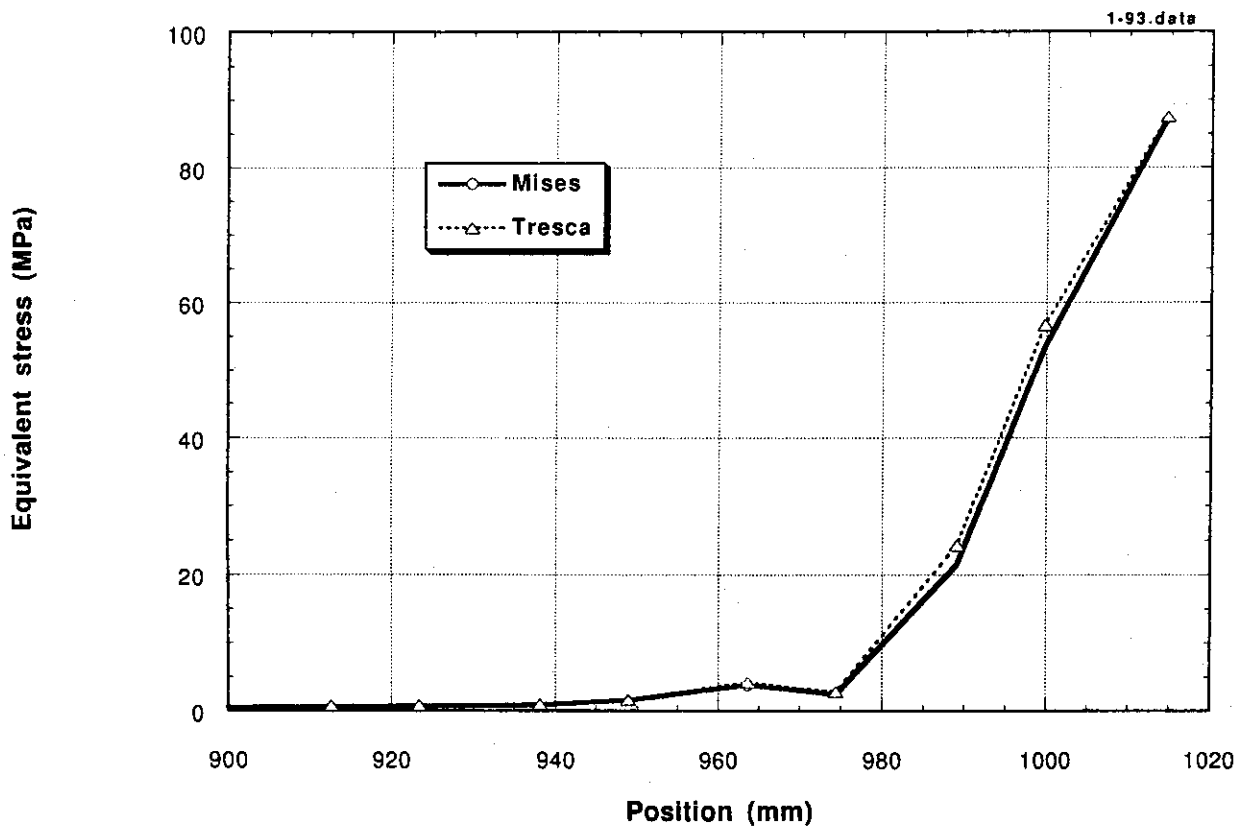
Fig. 70   Mises and Tresca equivalent stress distributions at selected elements in CASE 2
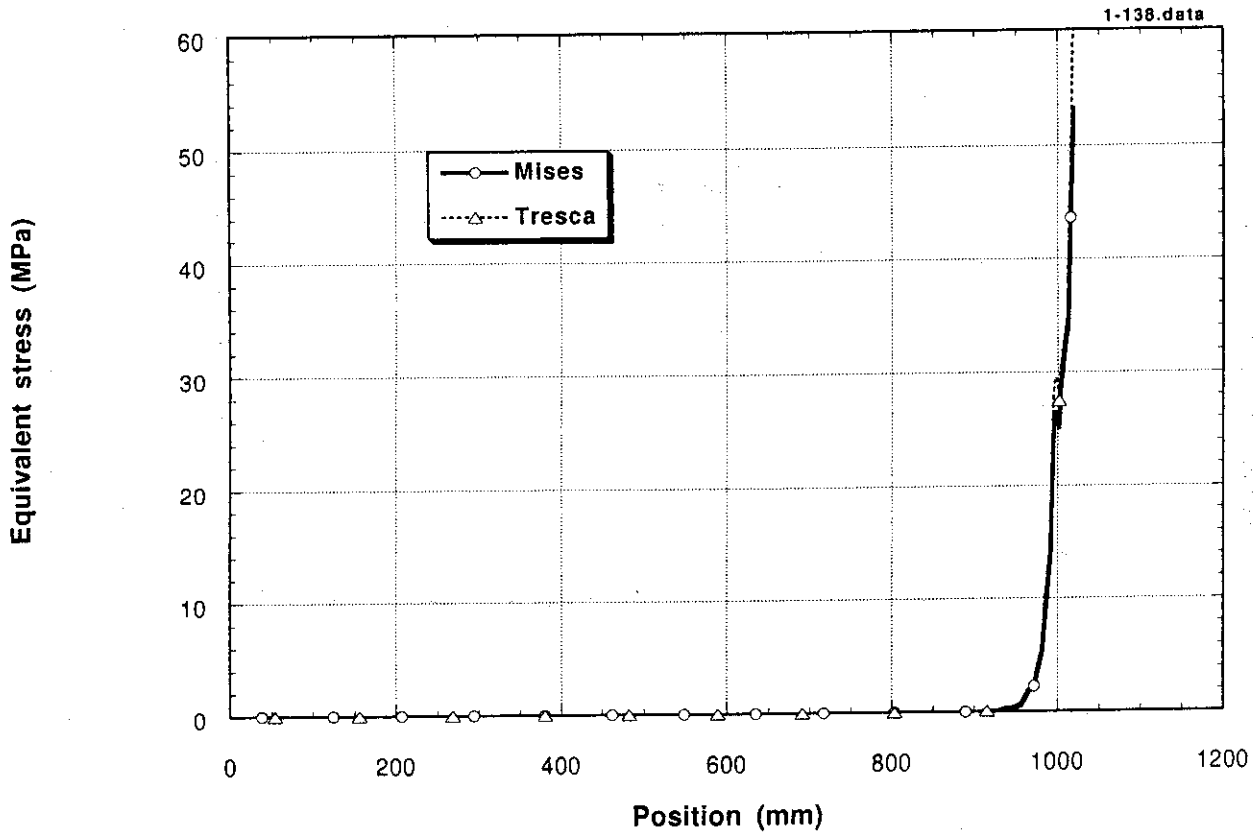(upper part of the cooling tube)

Fig. 71 Mises and Tresca equivalent stress distributions obtained in CASE 2
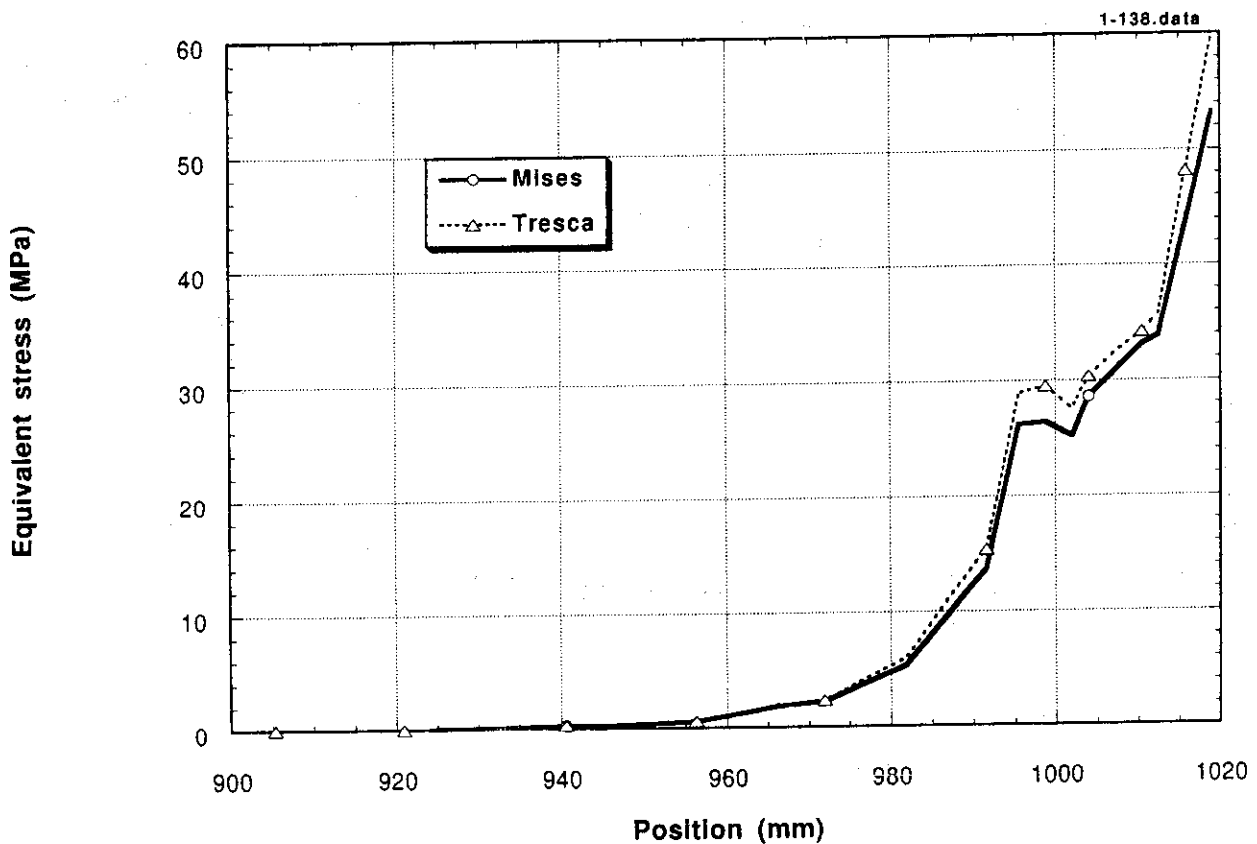(lower part of the cooling tube)

Fig. 72 Mises and Tresca equivalent stress distributions at selected elements in CASE 2
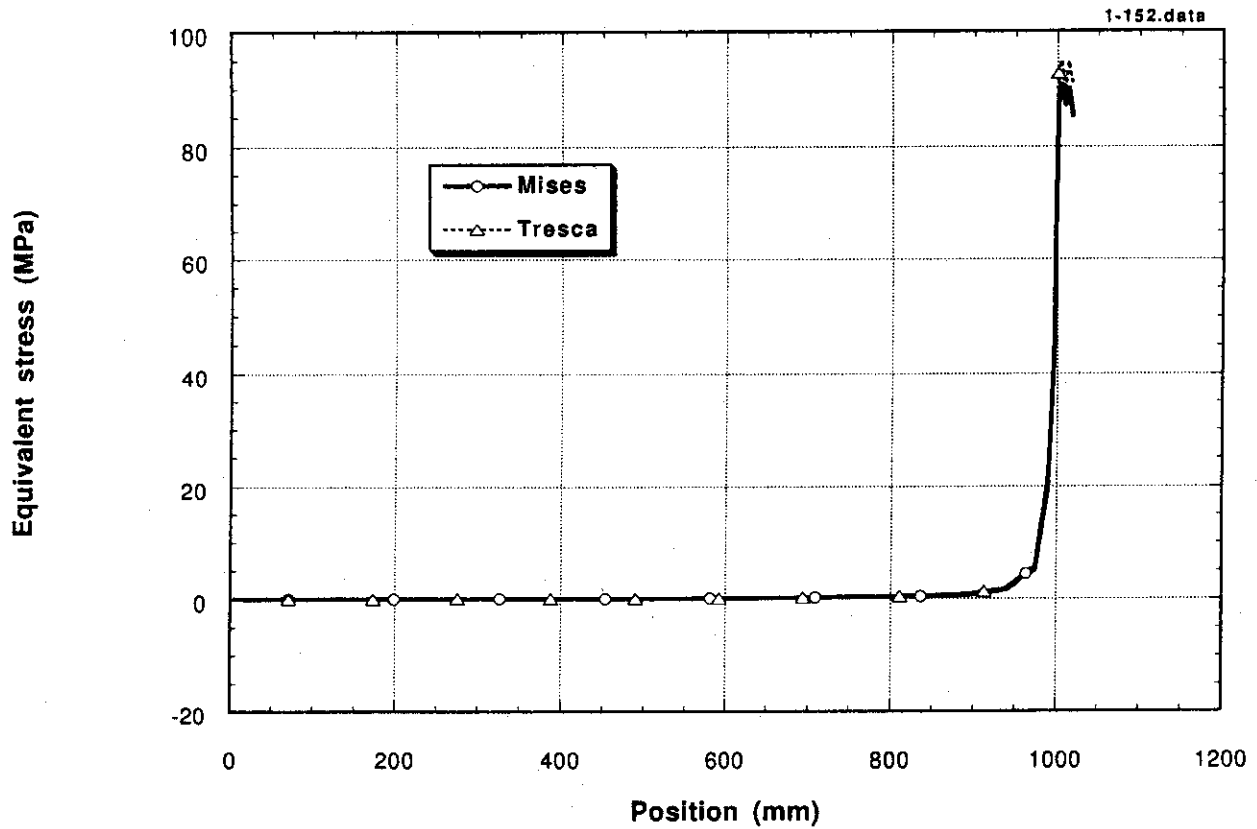(lower part of the cooling tube)

Fig. 73 Mises and Tresca equivalent stress distributions obtained in CASE 3
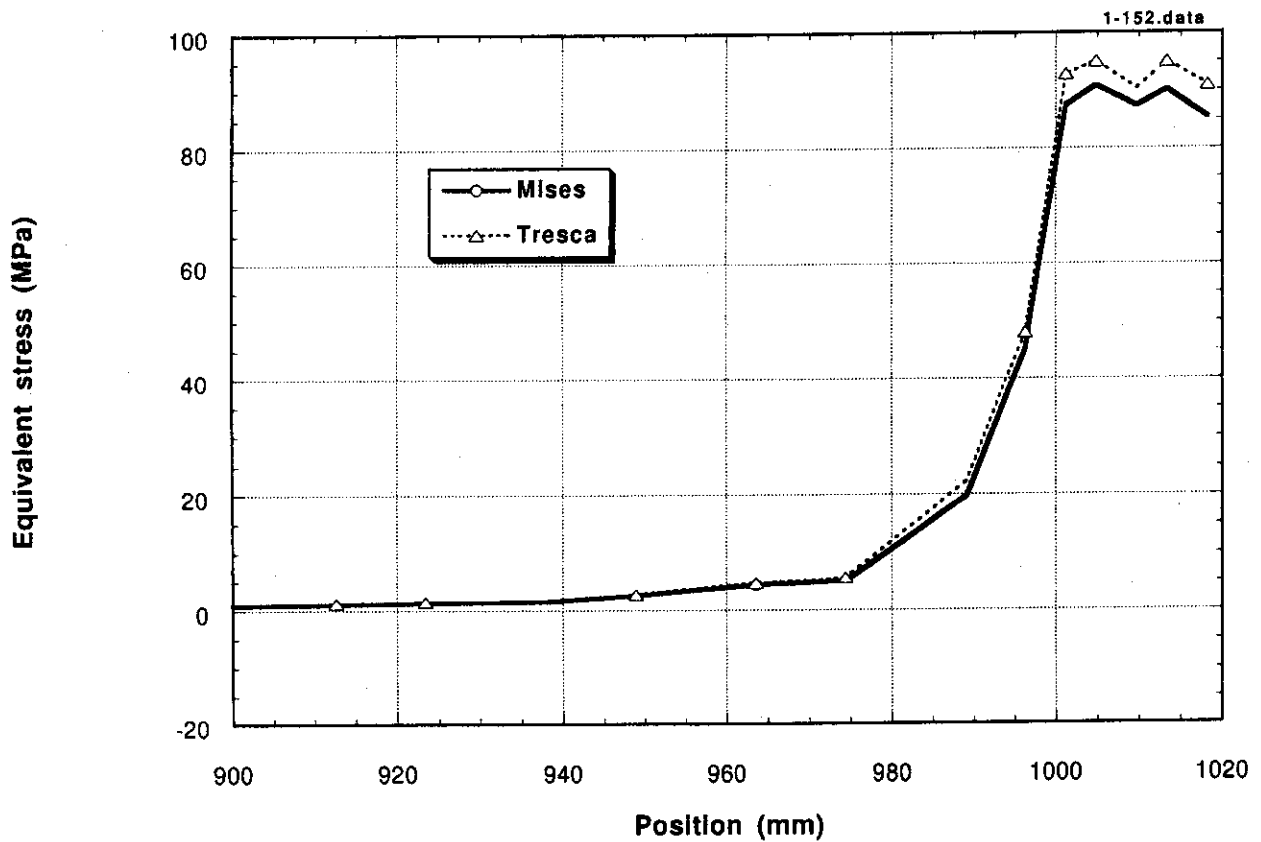(upper part of the cooling tube)

Fig. 74 Mises and Tresca equivalent stress distributions at selected elements in CASE 3
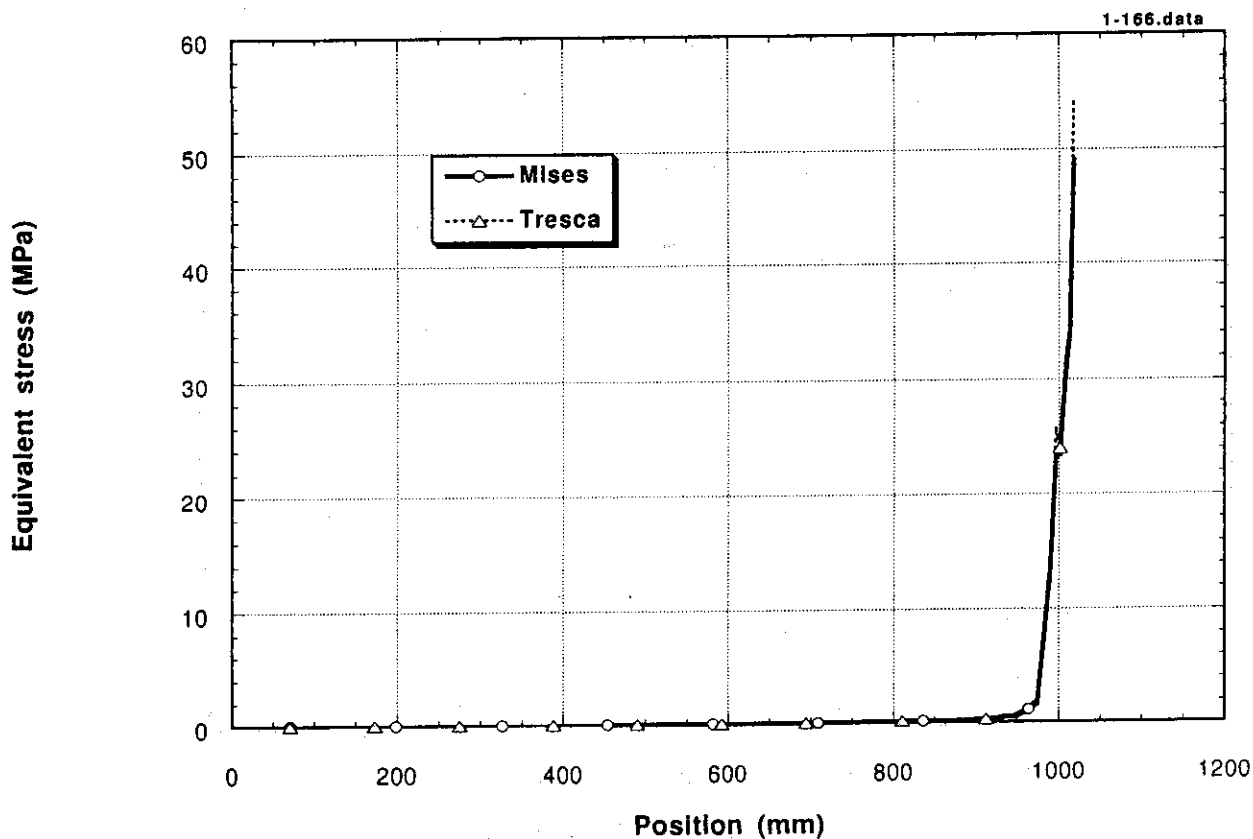(upper part of the cooling tube)

Fig. 75   Mises and Tresca equivalent stress distributions obtained in CASE 3
(lower part of the cooling tube)

Fig. 76   Mises and Tresca equivalent stress distributions at selected elements in CASE 3
(lower part of the cooling tube)

Fig. 77   Mises and Tresca equivalent stress distributions obtained in CASE 4
(upper part of the cooling tube)

Fig. 78   Mises and Tresca equivalent stress distributions at selected elements in CASE 4
(upper part of the cooling tube)

Fig. 79   Mises and Tresca equivalent stress distributions obtained in CASE 4
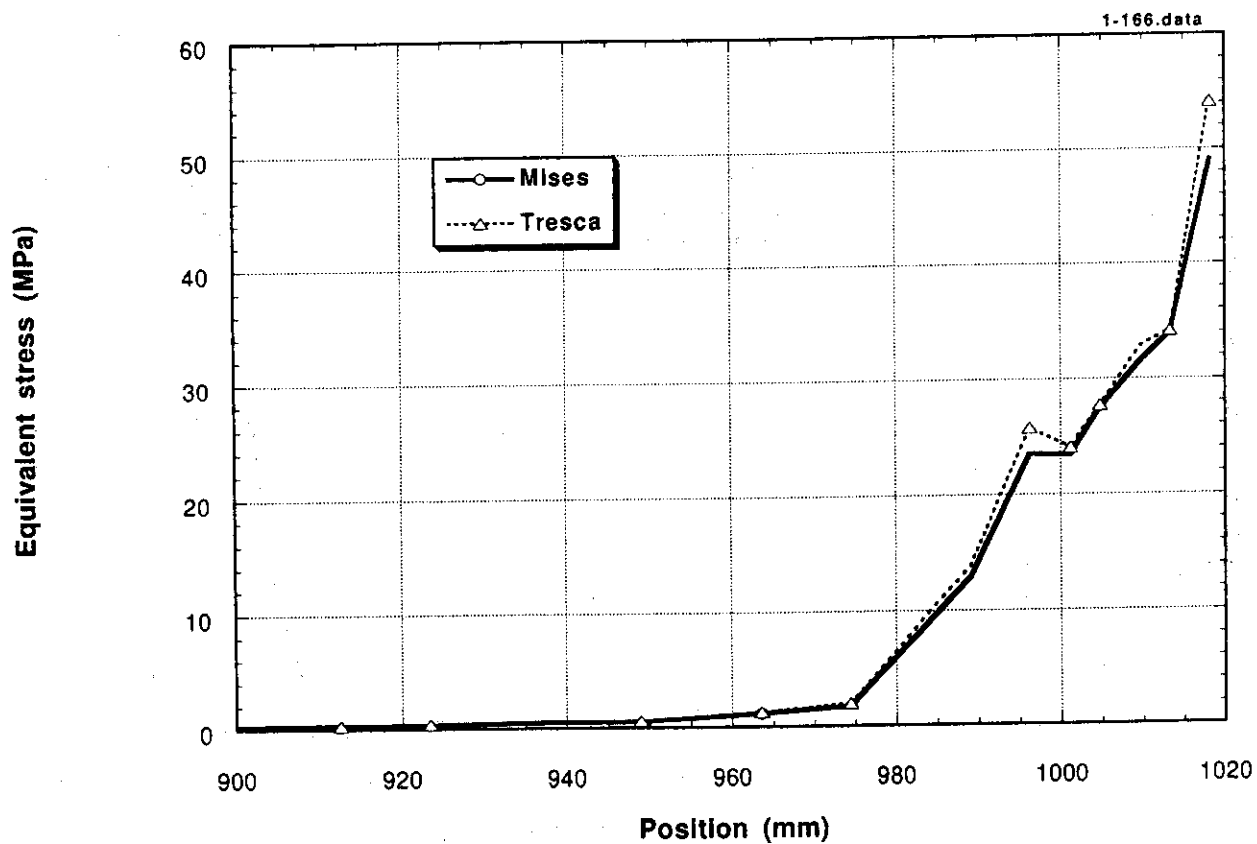(lower part of the cooling tube)

Fig. 80   Mises and Tresca equivalent stress distributions at selected elements in CASE 4
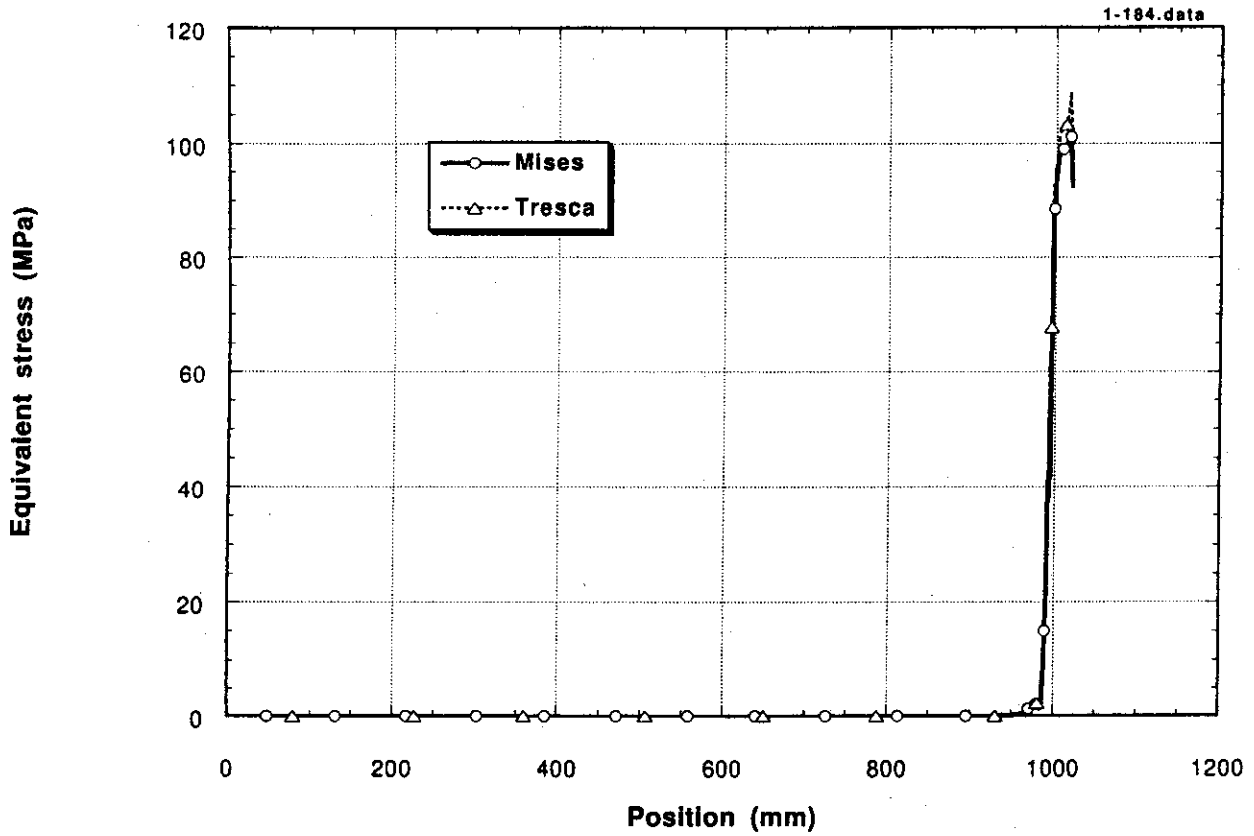(lower part of the cooling tube)

Fig. 81 Mises and Tresca equivalent stress distributions obtained in CASE 5
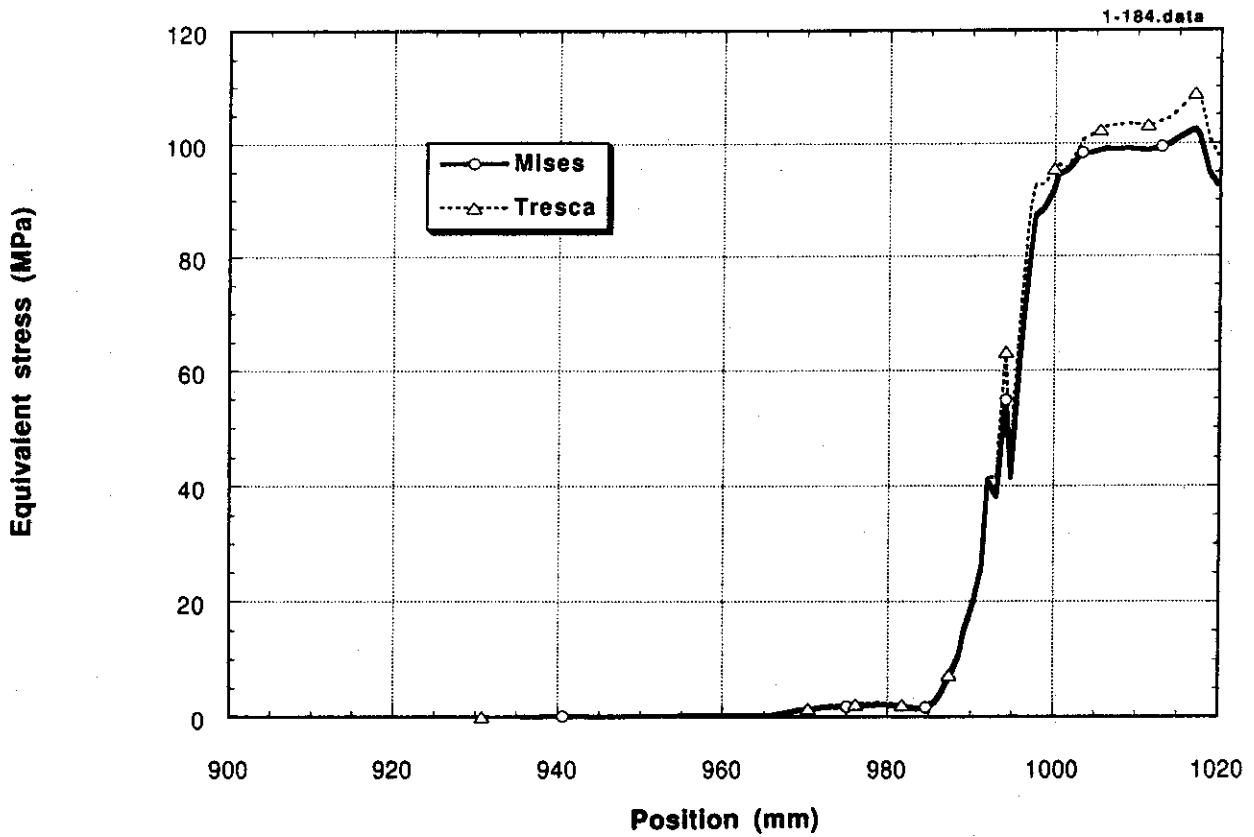(upper part of the cooling tube)

Fig. 82 Mises and Tresca equivalent stress distributions at selected elements in CASE 5
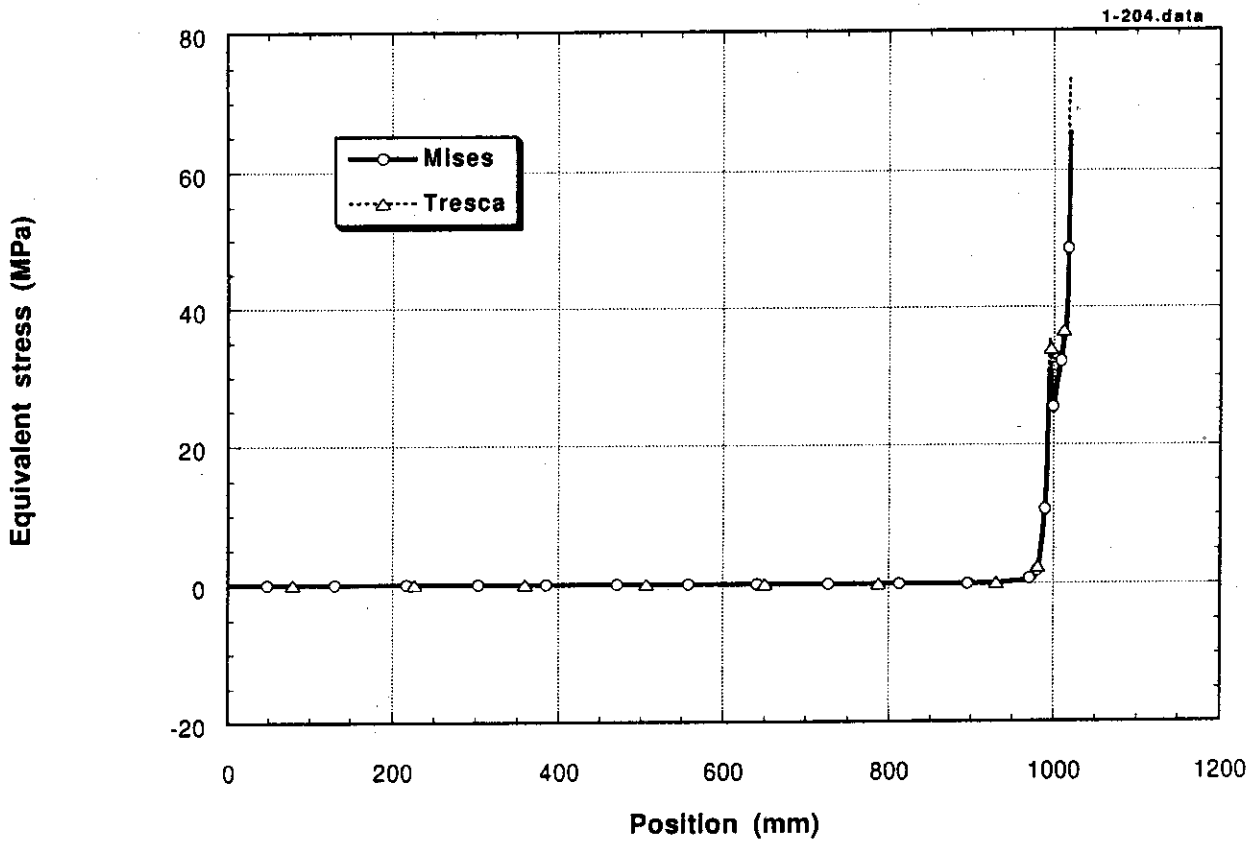(upper part of the cooling tube)

1-204.data

Fig. 83   Mises and Tresca equivalent stress distributions obtained in CASE 5
(lower part of the cooling tube)
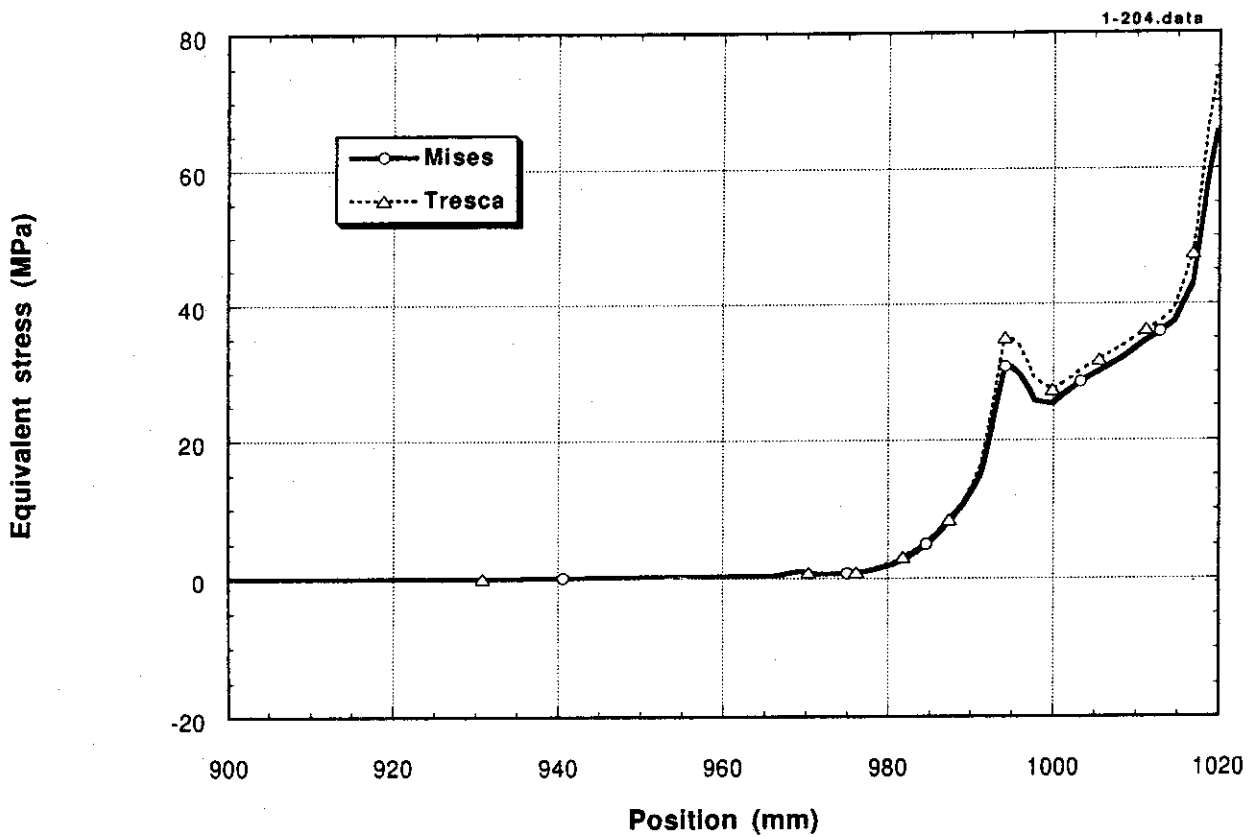
1-204.data

Fig. 84   Mises and Tresca equivalent stress distributions at selected elements in CASE 5
(lower part of the cooling tube)